UNIVERSITÀ DEGLI STUDI DI TRIESTE

XXXIV CICLO DEL DOTTORATO DI RICERCA IN
SCIENZE DELLA TERRA, FLUIDODINAMICA E MATEMATICA.
INTERAZIONI E METODICHE

NUMERICAL AND LABORATORY STUDY OF SEISMIC WAVES PROPAGATION, TEMPERATURE EFFECTS AND FLUID FLOWS IN MULTILAYERED MEDIA

Settore scientifico-disciplinare:
Geofisica Applicata-GEO/11

Dottorando:
Andrea Facca

Coordinatore:
Prof. Stefano Maset Stefano Maset

Supervisore di Tesi:
Prof. Michele Pipan Michele Pipan

ANNO ACCADEMICO 2020-2021

ABSTRACT

Steel production by continuous casting is nowadays the most efficient method and the one that yields the best quality semi-finished products. The types of steel that can be produced varies greatly depending on the composition of the mixtures, the casting powders used to prevent oxidation and reduce heat loss, the cooling rate, and many other factors. During continuous casting, heat from the molten steel must be removed in large quantities and quickly to allow the first layer of solid skin to be created, so the continuous casting moulds, *i.e.* large hollow tubes generally made of copper alloys, are immersed in a conveyor with a closed water circuit where water circulates at high speed and pressure. In addition to water, there are also other parameters that can be monitored to increase production quality, such as powder deposition on the casting bath and steel level control. It would be useful to have automatic systems capable of replacing manual human control, to avoid the hazardous situations obviously present in steel mills, but also to increase knowledge of the production process through the acquisition of reliable data. This research aims to experimentally explore the possibility of measuring the level of molten steel in the mould by making time-of-flight measurements in the wall of the ingot using ultrasonic transducers similar the ones used for non-destructive testing of materials. These time-of-flight measurements are then converted to temperature and determine a thermal profile along the mould wall, from which the steel level is derived using an ad-hoc constructed algorithm. The research activity was divided into the realization of a real-time hardware and software system that was eventually adopted in real production systems as well. To understand how to design an initial prototype and how to choose the key parameters of the measurement system, a numerical model was implemented to simulate Gaussian beams, which are used to approximate the propagation of ultrasonic beams in even heterogeneous media, as in this case. The results obtained, both from numerical simulations and laboratory tests, made it possible to implement a first sensor and to adopt a measurement technique already known in the literature but innovative in the sense of application to an industrial context such as continuous casting.

CONTENTS

LIST OF FIGURES

LIST OF TABLES

1 INTRODUCTION

1.1 THE CONTINUOUS CASTING OF STEEL

The continuous casting of steel is nowadays the most widespread and most efficient technique to produce semi-finished products, responsible of almost all the world's steel production: since the 1960s, the growth in the number of plants has resulted in more than 90% of the world's steel production being covered today. Several factors have contributed to the growth of these plants: research has produced different technologies that have increased the productivity of castings and also their quality. The increase of the casting speed has reduced costs per number of production lines and also has changed the roles for plant operators by orienting them toward less hazardous jobs and more productive activities. Continuous casting represents a milestone in the progress of steelmaking, even though the idea of this type of casting is quite dated. As early as 1857 Bessemer obtained a patent in England for the continuous casting of sheet metal directly from liquid steel, but it was not until the second half of the twentieth century that this process was introduced into industrial practice, when the difficult problems associated especially with steel's high melting temperature and its low thermal conductivity were solved. In 1960, there were just over 30 continuous casting plants installed in the world with a production capacity of about 1 million tons per year. In subsequent years and up to the present day, the number of continuous casting machines has increased rapidly and the production capacity has exceeded 1,000 million tons per year in 2010, according to data reported by [2]. Figure 1.1 shows production trends in millions of tons per year for the world's major countries. As can be seen, China has had the highest growth rate, rising from 95 million tons in 1999 to more than 800 million in 2017. Regarding the Western countries, they all had an increase in their production until 2007, starting to decrease since 2009, corresponding to the global financial crisis. After a quick recovery, production remained almost unchanged. Instead, most of the steel has become Chinese-made. For example in Italy, after a high of just over 30 million tons in 2007, the amount produced began to decline to 22.7 million in 2017. However, the relative share of steel produced by continuous casting has been gradually increased and, in 2017, about 96.2% of global steel is produced by this method. The increasing trend is observed in all countries, although for China it has been more abrupt, rising from 77% of total steel produced in 1999, to 98.7% in 2017. Figure 1.2 shows this global average trend over those years.

Figure 1.3 shows the relative comparison between countries in the 2 years 1999 and 2017. While in 1999 it was the Western countries that were the undisputed leaders in production, including Europe at first with large income from Italy and Germany, in the present days China produces the vast

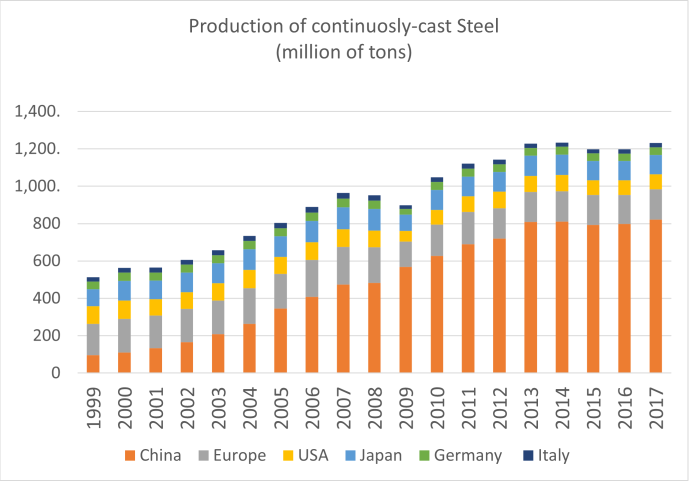

Figure 1.1: World continuous casting production capacity from 1999 to 2017.

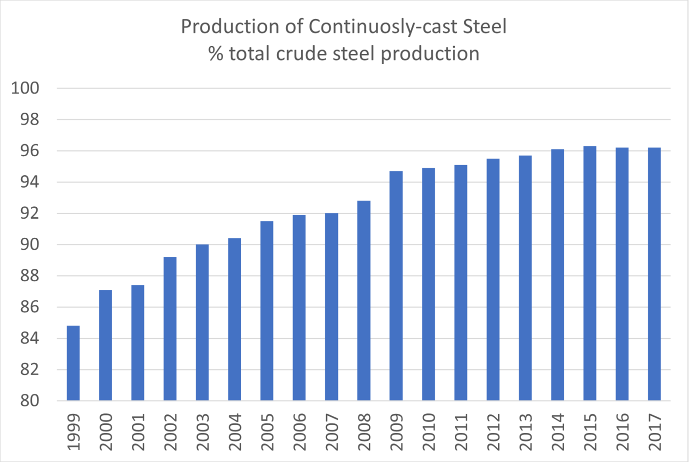

Figure 1.2: Percentage of steel produced by continuous casting.

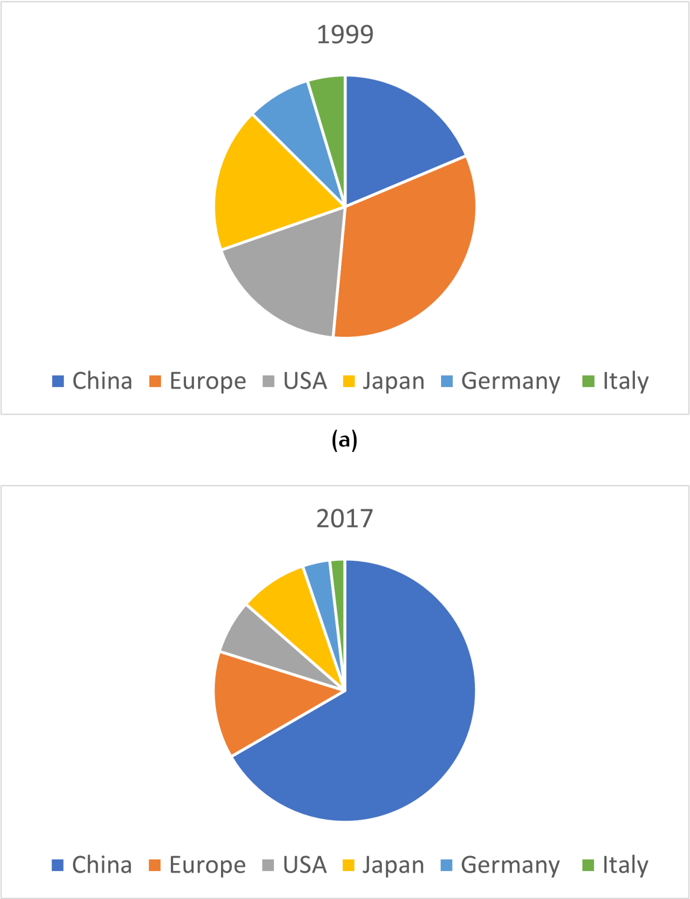

(a)

(b)

Figure 1.3: Relative distribution of steel production by continuous casting, across countries, in 1999 and 2017. Data obtained from WSA [2].

majority of steel, with Europe in second place, considering all 28 countries of the European Union.

The increase in production capacity, in addition to the increase in plants, has been also due to the size of the plants and the sections casted into them. Whereas in 1960 ladles had a maximum capacity of 100 tons and the sections were generally small (around $100\,\mathrm{cm}^2$) nowadays ladles can reach 400-ton and sections may exceed $6000\,\mathrm{cm}^2$.

1.1.1 Description of the process

In continuous casting, the liquid steel, placed in a container called a ladle, is decanted to the tundish, which acts as a lung and distributes it along the multiple casting lines, as shown in Figure 1.4 (a). In each casting line the steel enters the mould, a metal tube that can take on different geometric sections, where it begins the solidification phase and takes on the shape of the half-product. At the opposite end of the mould, where the steel exits, the outer wall of the semi-finished product is already in the solid phase, forming a first layer that maintains the shape of the semi-finished product, resisting to the ferrostatic pressure of the inner part that is not solidified yet. Before the casting start, a device called *false bar* or *false billet*, depending on the section being cast, is inserted at the bottom of the mould: the steel solidifies around it and the casting machine can start to extract the product. After a few moments, the extractor rollers begin to pull the *false bar* and with that, the semi-product moves inside the mould, beginning to solidify and shrink. The length of the mould is not random: if it were too short, the steel would not have enough time to form the first layer of solid skin to resist the ferrostatic pressure of the liquid phase, and it would break the semiproduct once it came out; if it were too long, the mould would not be able to exchange heat because the air gap due to the shrinkage of the section would interrupt the proper heat exchange. This is the reason why it is more efficient to spray with nozzles of steam on the semiproduct as it passes through the extractor rollers. The casting speed must be adjusted according to the amount of steel that falls from the distributor channel into the mould, so that the level of the steel meniscus in the mould remains constant. The principle of continuous casting is to produce no interruptions between castings, so the whole process takes place continuously, fed by sequences of ladles arriving from the melting furnace or refining stations. The continuous casting machine has undergone significant technological improvements, of which the most recent development is the curved machine (Figure 1.4 (b)) in which the mould can be straight or curved. The most common case is the latter, in which the bar is born curved and follows a path with a constant radius. In this way the height of the machine is considerably reduced and there is no limitation on the length of the bar that can be obtained. Compared with traditional pits casting, continuous casting offers very considerable advantages in terms of economics and often in terms of quality. Some of them are:

- Reduction in the number of stages and thus steel production time;
- Reduction in operating costs;
- Reduction in areas needed for plants;
- Reduction in investment capital;
- Reduction in labor costs;
- Possibility of automating and mechanizing part of operations;
- Quality improvements;

Regarding the last point, the quality of many continuously cast steels is now very high because they are preferred for the uniformity and consistency of their characteristics. One of the advantages of this type of casting is that it is possible to stir the liquid steel during casting through the use of electromagnetic stirrers, agitators that through the generation of intense magnetic fields stir the steel, preventing the formation of dendritic structures and reducing the number of defects. In addition to this, the use of lubricating oils and casting powders to reduce oxidation of surface steel are other tools that certainly realize an overall increase in product quality. The list of advantages of continuous casting could still be lengthened with other minor ones, but those already mentioned are sufficient to explain the success of this process.

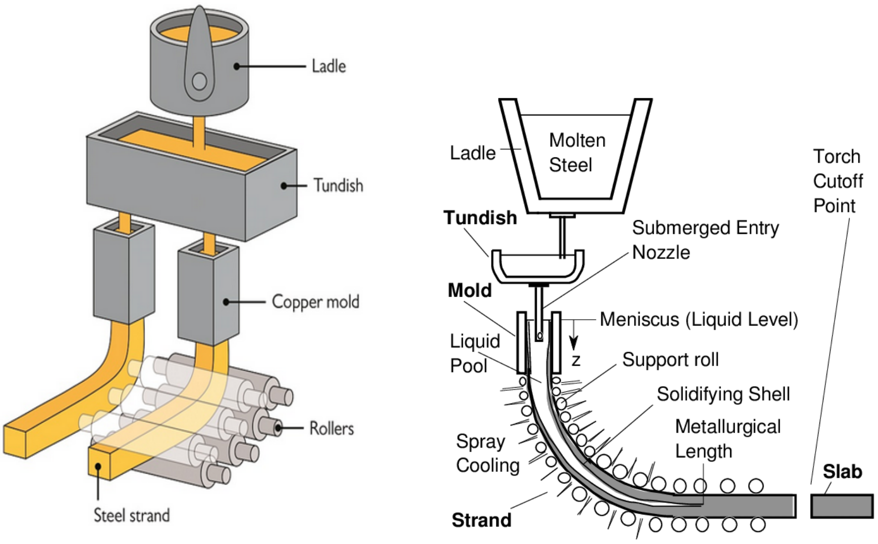

(a) (b)

Figure 1.4: Schematic diagram of the continuous casting.

1.2 MONITORING THE CONTINUOUS CASTING PROCESS

The study and control of what takes place during casting, and in particular during the solidification phase in the copper mould, makes it possible to greatly influence the final success of the product. Continuous casting has been studied for decades and efforts have been made to create devices whose goal is to monitor this delicate process. The approach to this kind of problem is to identify what are the basic parameters of the physical process and try to measure them correctly. This means that such devices are designed to operate in hostile environments, with widely varying conditions of temperature, humidity and also subjected to considerable wear and tear. These devices will be sensors that detect and measure chemical-physical quantities and produce an electrical output, i.e. they are transducers. An example is the ultrasonic transducer, a device that detects mechanical oscillations/vibrations in solid or liquid media and converts them into electrical signals that characterize them. Other examples are thermometers, barometers, or sensors used to detect concentrations of chemicals or pollutants in volumes of air. Since technological development has gradually accelerated over the years, technologies are now more affordable and sensors are increasingly integrated into the industrial world, enabling the development of more advanced automation and control techniques. In this context, a special area is reserved for sensors that monitor material processing and especially those that are applicable to continuous steel casting, which has been the main research topic of this paper. The idea to apply transducer to study and momitor the process of continuos casting is not so recent. As an example, in [26] there's the idea to apply ultrasonic transducer to monitor the processed materials, measuring their internal temperature to create a 2D map. In this way, with a process model to describe the physical evolution of the system and the measured variable the process variables can be adjusted, keeping them within certain limits. This is essentially the foundation of control pro-

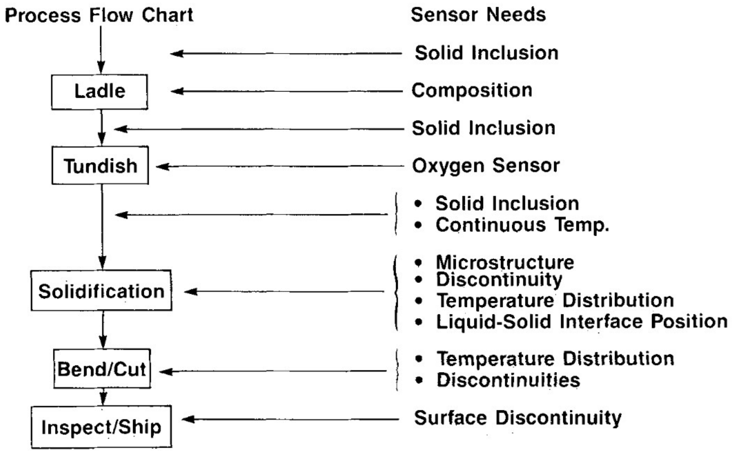

(a)

Figure 1.5: Process flow chart of continuous casting and possible physical and chemical property to measure. Image from [26].

cess theory. The temperature maps are realized with the measurements of the acoustic speed, knowing the physical relation between temperature and velocity. The latter is measured by measuring the delay between one echo and the next in the same path, using a single transducer operating as both transmitter and receiver (*pulse-echo* technique); or, by a pair of transducers. This delay is called time-of-flight (TOF) and allows, by knowing the distance traveled by the wave packet, the velocity to be derived. The types of transducers to accomplish this can be of different types, always with the aim of generating acoustic waves in conductive materials without contact, thanks to mechanical stresses produced by an electromagnetic effect, the so-called EMATs [30]. The revolutionary approoach is that it is not necessary to couple them with the surface of the investigated medium, so they are applicable in many contexts, even in harsh envinronment. Another type of transducers with different acoustic wave generation mechanism are the piezoelectric transducers: they are composed of thin membranes of ceramic material that deform under an electrical voltage. These mechanical vibrations are then transmitted to another medium by coupling the materials which compose the ultrasonic system. Within the entire continuous casting production process, various stages can be identified in order to act with some monitoring procedure. This makes it possible to act directly on quality control, and in order to do this the sensors have to manage the control cycle in real-time. The last action is therefore performed by a feedback mechanism on the casting machine, so that the adjusting parameters proccedure can be as precise and accurate as possible. As observed from Figure 1.5, the stages of steel transfer from the tundish to the ladle and the solidification are the most critical ones, where multiple events affect the quality of the final product. In the pouring of steel, for example, inclusions of slag, or of other substances, can coalesce; on the other hand, in the mould, if the steel is not stirred through the action of stirrers, it is more likely to form dendritic microstructures that make it inhomogeneous.

Regarding the aspect of the solidification, temperature distribution is definitely the most important aspect to know if good quality steel is to be obtained. Making a temperature distribution map, such as the one mentioned in the article using piezoelectric transducers with time-of-flight (TOF) measurements is a difficult because these would have to withstand contact with the surface of newly solidified steel for long time. Also in the case of measurements with EMATs it could be some problems. Since they operate in a non-contact configuration, but the distances can not be so wide, even a little surface defect might negative influence the produced wavelet. Then there is the unavoidable problem that the measurement, carried out at this stage, takes place anyway after the first layer of steel is just solidified, whereas it would be good to have information in the area corresponding to the liquid-solid steel interface, in contact with the surface of the bath inside the mould. Knowledge of the level of steel in the mould could therefore be very important, so much so that many companies have invested in making sensors for level control. In fact, over the years, a type of radioactive sensor, which is effective for monitoring level change by counts of photons emitted precisely from a bar of radioactive material placed in contact with the mould mold, has been very successful.

1.2.1 Numerical simulations

Another important aspect, which has become more and more crucial over the years and which parallels all the study for determining a measurement procedure during the process, concerns the development of numerical computer simulations. In the early 1970s, people began to think about how to model the phenomenon of steel solidification in the mould resolving the equations which describes the heat transfer phenomenom. In these cases, some authors started to investigate the behaviour of temperature and heat flux in the mould, rather than inside the semiproduct. In [22], analyses were carried out using a simplified physical model to derive which primary process properties may have the most influence on the temperature field distribution. It was found that the properties that significantly influence the absolute value of temperature and its profile along the lenght of the mould are relates to carbon content, lubrication and casting speed, while the thickness of the mould, the speed of the water, its inlet temperature and the conductivity of the copper affect it less. The study also emphasizes the different properties of mould alloys, not being composed of pure copper, but also containing traces of silver. In a more recent works,[5] and [6] discuss the effects of the parameters already mentioned in terms of heat transfer through the mould wall. The articles show different profiles obtained during casting using an mould mold lined with a network of thermocouples, held in stable contact with the mold, for all four faces. The conclusions evaluate how, thanks to this procedure and the use of modeling techniques and quality assessments on the material, it has been possible to perform an optimal design of the copper moulds. The big limitation of these studies, however, is that since they are focused on the study of the process, they are fine for characterizing the phenomenon, but not for producing a commercial sensor. Indeed, the investment needed for this such type of machining (the installation of a network of thermocouple) is quite considerable and it will not

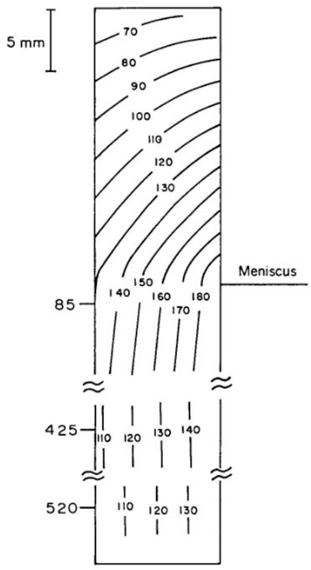

Figure 1.6: Predicted steady-state isotherms in the wall of a billet mould under standard conditions. On the right there's the liquid steel: from the bottom to the meniscus; On the left side there's the cooling water gap.Retrived from [22].

return. For most plants, the process informations remains inaccessible, so having instrumentation such as the one we described earlier would provide great benefits in terms of quality of productions. Figure 1.6 (a) shows a 2D map of the temperatures (isotherms) slenderness of the mould wall, while (b) shows a schematic of a section of the casting near the steel meniscus, where solidification begins.

1.3 ULTRASONIC TECHNOLOGY FOR PROCESS CONTROL

In the category of transducers, a very important type that finds very wide use in industrial but also biomedical fields is piezoelectric transducers, which are widely used in the field of materials processing because they are responsible for the class of devices used for nondestructive ultrasound exploration techniques [26], [24], [23]. The process of measuring by nondestructive techniques with ultrasound has a long history in industry, although the first to experiment is Floyd Firestone, of the University of Michigan, through his *reflectoscope*, the presence of inhomogeneities and defects in the material under inspection. The principle is very simple: acoustic waves are generated by inverse piezoelectric effect. By applying a potential difference at the ends of 2 metal plates separated by a piezoceramic material - a nonconductive piezoelectric ceramic or crystal material - deformation such as compression or expansion of the material is produced, which induces mechanical vibrations in a given range of frequencies, which can be determined according to the properties of the material and the size of the disk. The piezoelectric effect *directed*, is of course, the opposite: subjecting a portion of piezoceramic materail, sandwiched between 2 metal foils, to mechanical stress generates

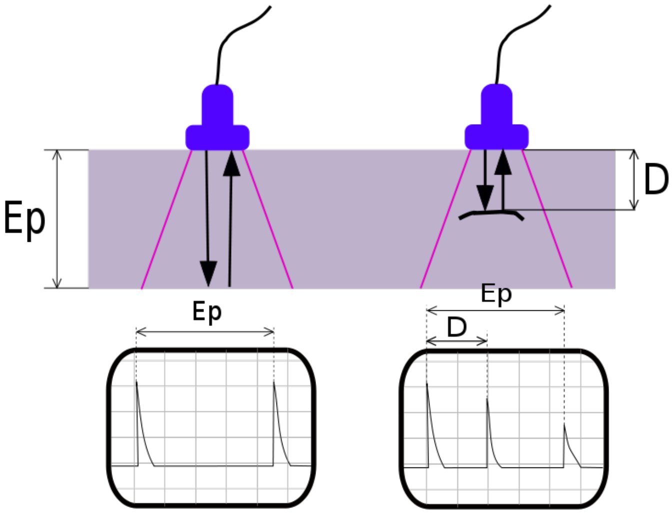

Figure 1.7: Schematic diagram of ultrasonic measurement of defect in material's interior. Image from [32].

electrical voltage and thus an electrical signal. Figure 1.7 schematically depicts the working principle of the ultrasonic inspection technique. The wave packet, in order to perform the round trip path in the portion of the material, it will takes an interval of time, defined as time of flight (TOFs). From the latter, knowing the properties of the material and from them the velocity, it is possible to derive the thickness of the medium to inspect. On the other side, the knowledge of the thickenss with the measured time of flight allow to retrieve the velocity.

1.4 ACTIVITIES OF THE RESEARCH

In such a complex process like the continuous casting, the intention of monitoring some key variables, including the temperature of the mould, is not so easy to achieve as it may seem, due to the particular operative environment. In particular, at the critical stage of the process,*i.e.* in the area where solidification of the steel inside the mould begins, it is difficult to access with instrumentation to take measurements because one is subjected to the constant exposure of extreme conditions due to the presence of glowing steel. Presented in this light, the activities to reach the goal of build the ultrasonic sensor can be decompose in three phases:

- Laboratory testing of experimental ultrasonic setups for time-of-flight measurement in an environment simulating the real continuous casting configuration;
- Analysis and development of signal analysis algorithms in a real time hardware and software system;
- Analysis and development of a procedure for calibrating temperatures measured indirectly from time-of-flight with the developed hardware instrumentation.

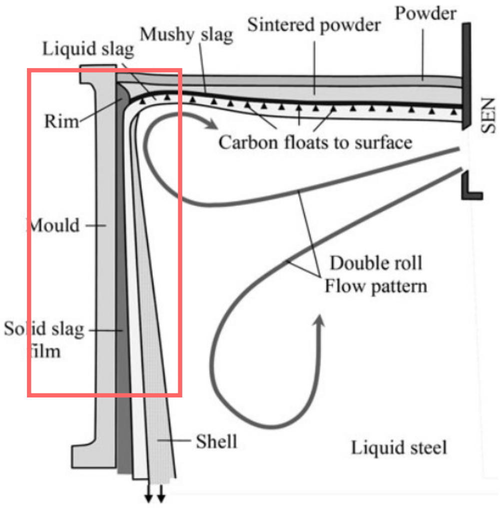

(a)

Figure 1.8: Schematic diagram showing various phases and their location in the mould: differen solid slag layers anche the convective motion of the liquid steel outgoing the Submerged Entry Noozle (SEN), from [20]. In the red recangle is highlighted the most relevant zone of the process.

The first activity is to test with ultrasonic transducers a measurement technique based on the time-of-flight of acoustic waves propagating in the mould wall. Figure 1.8 schematically shows a section of the continuous casting near the meniscus area of the steel. As imagined, in that region the temperature variations measured in the mould can be very large and variable within a few centimeters. It is precisely in this region that we would have the largest effects on the measured time-of-flight variation, and the area highlighted in red shows where the possible transducer might act. In this space, which is very small because it is at most 15 cm, the whole dynamics of the solidification process is concentrated. Unfortunately, the fact that the actual process takes place with liquid steel makes it virtually impossible to replicate the actual process in the laboratory. In addition, the fact that in-plant testing cannot be done easily and in a short period of time has also limited the ability to test proven configurations. With all of these constraints, it is evident how arduous it could be evaluate these considerations and experiments. Therefore, the objectives of this work focus on the common aspect of finding a viable approach that can then be employed in more focused and specific future analyses that will result in the construction of an initial prototype. While characterization studies of metals and metal alloys are present in the literature, applications in this context are virtually nonexistent.

The initial research activity focused mainly on the use of state-of-the-art instrumentation to build prototype transducers consisting of piezoelectric probes in both PZT and piezoceramic material. Tests were carried out in the laboratory in multiple configurations in order to choose which arrangement would be the most suitable, considering the restricted space of use that a hypothetical device should have in that context. In this first phase, the help of numerical simulations of the ultrasonic beam made it possible to study the shape and size of the transducers to be used for this application. With this tool, it was possible to estimate the maximum width of the beam inside the wall of the copper plate used as a prototype mould: in this way, we looked at the best configuration and the minimum distance at which to place two probes side by side, ensuring that there was no interference between the pulses of each individual probe. The second main activity, i.e. the development of signal analysis algorithms to be used in real time, was done on signals acquired in the laboratory in the above configurations. At the preliminary stage, several approaches were considered, including cross-correlation as a technique to correctly estimate the difference of times in the echoes of the measured signals; after which a technique based on interpolation and then signal reconstruction was developed. The last principal activity was achieved by using the information and background acquired during the first two parts of the work, obtaining acceptable results for the realization of a prototype instrument for temperature measurement.

This Thesis is therefore the presentation of the results obtained in the logical order they have been presented. In details, the in the following Chapter it will be show:

- Presentation of the fundamental aspects of acoustic and elastic wave propagation in solid media;
- Description of ultrasonic experimental setup and measurement method approach;
- Description of the tests carried out in the laboratory and the results of the application of the analysis algorithms;
- Conclusion and possible future developments.

2 ULTRASONIC SYSTEM DESIGN AND FIELD MODEL

This Chapter first introduces the ultrasonic system model formed by the superposition of layers of different materials, which was studied as a configuration of the sensor measurement setup. Mathematically, the acoustic wave beams generated by these transducers can be described with a multi-Gaussian beam model, and such a model was developed to be able to analyze the configurations. Finally, the theoretical guidelines provided by ASTM for a proper experimental approach to transducer measurements are listed, including the methodology for deriving velocity in both metal plates and wedge materials. More information and details can be found in [15] for the development of probe design guidelines in [3].

2.1 DESCRIPTION OF THE SYSTEM

An ultrasonic system consists not only of the transducer, defined according to the American Society for Testing and Materials (ASTM) *an electro acoustical device for converting electrical energy into acoustical energy and vice versa*, but also of other components: the wedge material, the lens system to refocus the beam and redirect it according to specific requirements, the coaxial cables, and the entire electronics drive system. The transducer plus the mounting socket, which also has the function of a delay and support line, is called in literature *search unit* or, more simply, *probe*. A typical angled commercial probe is shown in Figure 2.1, where the transducer is glued to the wedge and the overall composition acts as a delay line.

In addition to this, the ultrasound system also consists of the electronic part, such as cables, pulsator and oscilloscope, and receiver. The design procedure of this type must therefore take into account the inspection method,

Figure 2.1: Typical commercial angle beam probe: a transducer atteached on a wedge. Retrieved from [3].

the available technology to the specific application, and the proper assembly of the electro-mechanical and electronic components. Design methods and systems have evolved over time: in the beginning, it was only possible to connect a probe to one channel, and performing multiple inspection procedures required multiple scans, changing the probe support each time on demand; nowadays there are commercial instrumentations with electronics capable of handling multiple channels, with considerably more transducers. Transducer manufacturing has now reached high standards in terms of quality, so companies that provide services or products for nondestructive testing no longer build them, but the design part of the system must be customized as needed, so this is an integral part of the design work. In particular, the basic parameters regarding the geometric quantities of the transducer and the dimensions of the objects to be inspected must be determined. In this context, the objective of this Chapter is positioned: Model the physical measurement system in the most common configuration found in the continuous casting process situation. The physical elements that constitute the consinuous casting environments are:

- Molten steel inside the copper mould;
- Solid-liquid interface (solid shell);
- Copper mould;
- Cooling water gap;

The simplest model then involves the transducer being immersed in the cooling water gap, aligned with the mould wall so that the generated beams propagate through the water layer and impact the outer wall. The transducer should be equipped with a wedge so as to direct the beam along the direction normal to the surface. The main objective of the wedge is to transmit ultrasonic energy from the transducer through the interface with a test object to create in it an acoustic field suitable for a given inspection application. The system to be modeled stops up to the ingot: the interesting activity is the possibility of measuring the time-of-flight of the echo inside the wall, so measuring the first two echoes back from the inner wall. As depicted in Figure 2.2 (a) it will consist of:

- PZT Search Unit device or other piezo-ceramic material;
- Wedge material for support and delay line;
- Water Gap;
- Planar slab of copper;

Considering that the direction of propagation is normal to the surface, the vertical heterogeneity due to coupling of different materials has to be considered, while in the horizontal direction it is correct and simple to assume that the medium is infinite, so that the problem of reflections at the domain boundary does not arise. In fact, this condition is irrelevant to the problem, because even from a practical point of view the elements can be considered homogeneous and isotropic plane layers, and the probes are located far away the border of the copper mould. Indeed, the region near the meniscus of the molten steel is about 20 cm below the top of the mould. Figure 2.2 (b) depicts the model to simulate: at the interfaces of different materials, it is necessary to take into account through the transmission and reflection coefficients the contributions in energy passing from one layer to another, due to impedance differences.

2.2 GAUSSIAN BEAMS IN FLUIDS AND THE PARAXIAL APPROXIMATION

The purpose of an acoustic field calculation is to determine its parameters at every point of the field, specifically the sound pressure and the direction of particle motion which defines the mode. The basic parameters of the directional characteristics are the central ray refracted angle and the shape of the main lobe. If the problem regard the straight beam propagation, there are no refracted angle since the propagation can be assumed as straight and normal to the surfaces, so the only thing to investigate is the width and shape of the main lobe.

Many physical processes regarding wave propagations are well described by the formalism of plane and spherical waves. For example, these types of waves are used in acoustics, optics, geophysics and also represent building blocks for quantum mechanical systems. In such a systems, where the radiation's wavelenght is comparable with the dimension of the sample to be investigated, the use of spherical and plane waves could retrieve high inefficient computations. In the case of ultrasonic Non-Destructive Evaluation, sound beams are made of high frequency components: a method which implements superposition of plane or spherical waves could be quite inefficient for a correct description of the transducer's field. On the other hand, Gaussian beams can be used as particular solutions for these problems, providing a powerful numerical model working in a variety of geometrical shapes and materials.

Consider the case of wave propagation in a fluid. It can be represented with a plane wave of pressure p, which satisfies the wave equation. Assume the wave is propagating primarily along a fixed direction, say x_3. The time dependency $e^{-i\omega t}$ con be neglected and an harmonic wave solution can be placed into the wave equation in a form of quasi-plane wave

$$p = P(x_1, x_2, x_3)e^{ik_p x_3}. \tag{2.1}$$

Then P satisfies the following equation:

$$\frac{\partial^2 P}{\partial x_1^2} + \frac{\partial^2 P}{\partial x_2^2} + \frac{\partial^2 P}{\partial x_3^2} + 2ik_p \frac{\partial P}{\partial x_3} = 0 \tag{2.2}$$

It is expected that at high frequencies the complex exponential term will capture the most relevant variation in the x_3 direction. The wave diffraction effects associated with the $\frac{\partial^2 P}{\partial x_3^2}$ term is small in comparison with the other

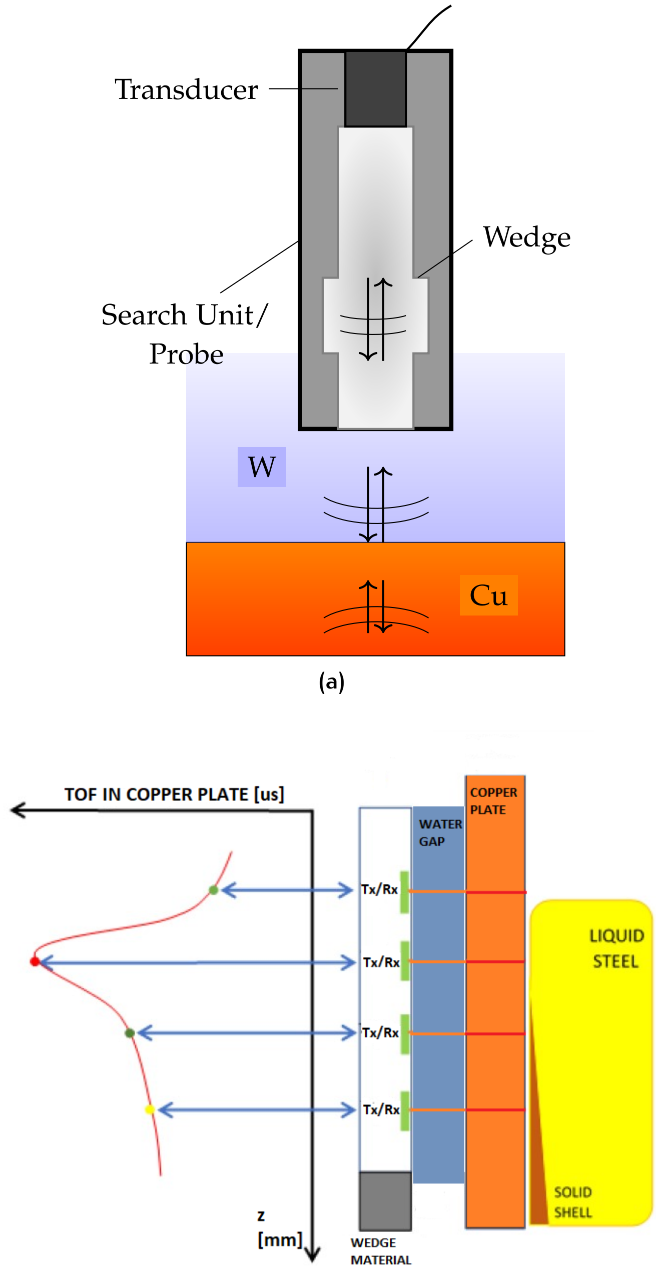

(a)

(b)

Figure 2.2: (a)Schematic representation of search unit configuration tested in laboratory measurements. The transducer is coupled with the wedge material (Rexolite) and the ultrasonic waves are transmitted from the wedge to the water (W) layer. Eventually the beams propagates back and forth in the copper (Cu) layer. (b) Schematic representation of the installation on the side of the copper mould for concrete application of multiplte ultrasonic search units. Each points in the vertical *z* axis represent a search unit position. The concrete installation in the production plant is obviously rotated by 90° since the casting is done in vertical direction.

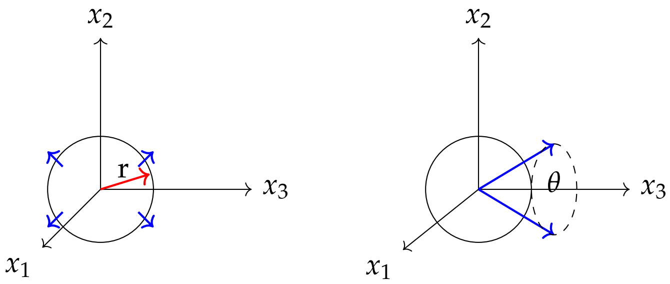

Figure 2.3: *Left*: spatial dispersion of spherical wave. *Right*: region wher the paraxial approx. is valid.

$$\frac{\partial^2 P}{\partial x_3^2} \ll \frac{\partial^2 P}{\partial x_1^2}, \frac{\partial^2 P}{\partial x_2^2}, 2ik_p \frac{\partial P}{\partial x_3}, \tag{2.3}$$

which leads to the *paraxial wave equation* for P:

$$\frac{\partial^2 P}{\partial x_1^2} + \frac{\partial^2 P}{\partial x_2^2} + 2ik_p \frac{\partial P}{\partial x_3} = 0 \tag{2.4}$$

Paraxial equation places some physical limits on the properties of Gaussian beams, for detailed information refers to [23]. The pressure in the fluid for a spherical wave propagating from a point source is described as

$$p = A\frac{e^{ik_p r}}{r} \tag{2.5}$$

where $k_p = \omega/c_p$ is the wave number of the pressure wave, with ω representing the angular frequency and c_p the wave speed of the fluid. $r = \sqrt{x_1^2 + x_2^2 + x_3^2}$ is the distance from the source point. Considering only a small angular region in the neighbours of the main direction of propagation x_3 (say $x_2/x_3 \ll 1$ and $x_1/x_3 \ll 1$) the spherical wave can be approximated viewing that

$$\begin{aligned} r = \sqrt{x_1^2 + x_2^2 + x_3^2} &= x_3\sqrt{1 + \frac{x_2^2 + x_3^2}{x_3^2}} \\ &\simeq x_3\left(1 + \frac{x_1^2 + x_2^2}{2x_3^2}\right) \\ &\simeq x_3 + \frac{x_1^2 + x_2^2}{2x_3} \\ &= x_3 + \frac{\rho_0^2}{2x_3} \end{aligned} \tag{2.6}$$

with $\rho_0 = \sqrt{x_1^2 + x_2^2}$. The final expression becomes

$$p \simeq A\frac{e^{ik_p(x_3 + \frac{\rho_0^2}{2x_3})}}{x_3} \tag{2.7}$$

To estimate the goodness fo the approximation the ratio $k_p r/k_p x_3$ is computed, knowing that ρ_0/x_3 represent the tangent of the angle θ between the

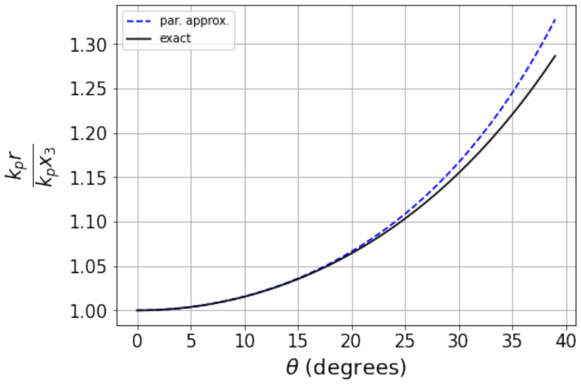

(a)

Figure 2.4: Normalized phase terms comparison. Solid line: exact normalization term. Dashed line: paraxial approximation term.

x_3 axis and the orthogonal plane (x_1, x_2), namely $\tan\theta$ (see Fig.2.3). It could be found that

- For an exact spherical wave:

$$\frac{k_p\, r}{k_p\, x_3} = \sqrt{1+\tan^2\theta} \tag{2.8}$$

- for paraxial approximation:

$$\frac{k_p\, r}{k_p\, x_3} = 1 + \frac{\tan^2\theta}{2}. \tag{2.9}$$

Fig. 2.4 shows the comparison between the two normalize phase terms versus the angle θ. The paraxial approximation begins to lose accuracy at an angle of 30 degrees from x_3 axis.

Comparison with other example cases are possible,*i.e.* using a Rayleight-Sommerfeld integral model to represent the transducer radiation in a fluid. Is is found that for both the on-axis pressure and for the angular spectrum inside a certain range the paraxial approximation is quite good. For details, see [24].

2.2.1 General form of a Gaussian beam

Gaussian beams are beams whose amplitude envelope in the transverse plane is given by a Gaussian function [31]. The general form which will be use in the subsequent is:

$$p = P(x_3)e^{i\frac{\omega}{2}\mathbf{X}^T\mathbf{M}_P(x_3)\mathbf{X}} \tag{2.10}$$

with $\mathbf{X} = [x_1, x_2]^T$, and $\mathbf{M}_p$ is a 2x2 complex-valued symmetric matrix. This matrix defines the properties for the propagating beam, like the beam width and the radius of curvature.

Substituting 2.10 in the general *paraxial wave equation* 2.4:

$$\frac{2}{c_p}\frac{\mathrm{d}P}{\mathrm{d}x_3} + P\,\mathrm{tr}(\mathbf{M}_p) + iP\mathbf{X}^T\left(\frac{1}{c_p}\frac{\mathrm{d}\mathbf{M}_p}{\mathrm{d}x_3} + \mathbf{M}_p^2\right)\mathbf{X} = 0 \tag{2.11}$$

To satisfy this one for all $\mathbf{X}$ the system of these two equations is obtained:

$$\frac{2}{c_p}\frac{\mathrm{d}P}{\mathrm{d}x_3} + P\,\mathrm{tr}(\mathbf{M}_p) = 0 \tag{2.12a}$$

$$\frac{1}{c_p}\frac{\mathrm{d}\mathbf{M}_p}{\mathrm{d}x_3} + \mathbf{M}_p^2 = 0 \tag{2.12b}$$

The first is called *transport equation*, as in the framework of the ray theory; while the second one is a particular type of the non-linear *Riccati equation* in matrix form[1].

Manipulation of both of these equations lead to the solution for $\mathbf{M_p}(x_3)$. Leaving aside the mathematical details, the solution of 2.12 is obtained by direct integration, which correspond to the *propagation law*

$$\begin{aligned}\mathbf{M}_p^{-1}(x_3) &= c_p x_3\mathbf{I} + \mathbf{M}_p^{-1}(0)\\ &= \left[c_p x_3\mathbf{M}_p(0) + \mathbf{I}\right]\mathbf{M}_p^{-1}(0).\end{aligned} \tag{2.13}$$

Taking the inverse, it's found in the end:

$$\mathbf{M}_p(x_3) = \mathbf{M}_p(0)\left[\mathbf{I} + c_p x_3\mathbf{M}_p(0)\right]^{-1} \tag{2.14}$$

In addition, the $P(x_3)$ and $P(0)$ terms can be obtained by integration of a manipulated term of 2.12b

$$\frac{\mathrm{d}}{\mathrm{d}x_3}\log\left[\frac{P(x_3)}{P(0)}\right] = \frac{\mathrm{d}}{\mathrm{d}x_3}\log\left[\det\left(\frac{\mathbf{M}_p^{-1}(x_3)}{\mathbf{M}_p^{-1}(0)}\right)^{1/2}\right] \tag{2.15}$$

with $P(0) = P(x_3)|_{x_3=0}$. The integration leads to

$$\frac{P(x_3)}{P(0)} = \sqrt{\frac{\det\left[\mathbf{M}_p^{-1}(0)\right]}{\det\left[\mathbf{M}_p^{-1}(x_3)\right]}} = \sqrt{\frac{\det\left[\mathbf{M}_p(x_3)\right]}{\det\left[\mathbf{M}_p(0)\right]}}. \tag{2.16}$$

These formulas can be used to modify the general form of a Gaussian beam:

$$p(\mathbf{x},\omega) = P(0)e^{ik_p x_3}\sqrt{\frac{\det\left[\mathbf{M}_p(x_3)\right]}{\det\left[\mathbf{M}_p(0)\right]}}\,e^{i\frac{\omega}{2}\mathbf{X}^T\mathbf{M}_p(x_3)\mathbf{X}} \tag{2.17}$$

The velocity can also be obtained by differentiating this pressure; however, in the paraxial approximation the dominant term in such an operation comes from the $e^{ik_p x_3}$ term, so the velocity is given by [2]

$$\mathbf{v}^p(\mathbf{x},\omega) = V^p(0)\mathbf{d}^p e^{ik_p x_3}\sqrt{\frac{\det\left[\mathbf{M}_p(x_3)\right]}{\det\left[\mathbf{M}_p(0)\right]}}\,e^{i\frac{\omega}{2}\mathbf{X}^T\mathbf{M}_p(x_3)\mathbf{X}} \tag{2.18}$$

---

[1] *Riccati equation*: $y'(x) = q_0(x) + q_1(x)y(x) + q_2(x)y^2(x)$, with $q_0(x) \neq 0$ and $q_2(x) \neq 0$

[2] For the demonstration that the other terms coming from differentiation are indeed negligible.

where $V^p(0) = P(0)/\rho c_p$, ρ is the density of the fluid and $\mathbf{d}^p$ is the unit vector in the x_3 direction of propagation. This form is the most common one to be used in the Gaussian beam formalism for the ultrasonic field computation.

2.2.2 The $\mathbf{M}_p$ matrix

Gaussian beams could be found in a variety of field of applications. First of all, they are used in optics to represent light beams in lasers. Optics representation of Gaussian beams is almost identical to that of fluids, since to describe the behaviour it's need only a scalar field. The term which describes the shape of the generated Gaussian beams are embedded in the $\mathbf{M}_p$ matrix term. In the laser literature, the matrix $\mathbf{M}_p$ is usually represented in a diagonal matrix of the form

$$\mathbf{M}_p(x_3) = \begin{bmatrix} \frac{1}{c_p q(x_3)} & 0 \\ 0 & \frac{1}{c_p q(x_3)} \end{bmatrix},$$

where $q(x_3)$ represents a complex scalar. In 2.17, this representation becomes

$$p(\mathbf{x}, \omega) = P(0) e^{ik_p x_3} \frac{q(0)}{q(x_3)} e^{\frac{ik(x_1^2 + x_2^2)}{2q(x_3)}} \tag{2.19}$$

and the propagation law 2.14 for $\mathbf{M}_p$ is

$$q(x_3) = q(0) + x_3. \tag{2.20}$$

Eq. 2.19 represents a Gaussian beam of circular cross section. As long as $q(0)$ has a negative imaginary part, the propagation law shows that $q(x_3)$ maintain a negative imaginary part so that equation will describe a beam always localized near the axis of propagation. $q(0)$ is a complex constant which depends on frequency ω, and has a important physical meaning: it can be expressed as

$$q(0) = -\left(x_{03} + \frac{i\pi w_0^2}{\lambda_p} \right) \tag{2.21}$$

with (x_{03}, w_0) having the dimensions of a length and $\lambda_p = 2\pi/k_p$ is the wavelength. The term $x_{R3} = \pi w_0^2/\lambda_p$, which is a distance, is the *confocal distance* or *confocal parameter*. x_{03} is the location of the beam waist, *i.e.* the location where the beam width $w(x_3)$ is smallest. In this way, the parameter $q(x_3)$ can be written in another form

$$\frac{1}{q(x_3)} = \frac{1}{R(x_3)} + i\frac{\lambda}{\pi w^2(x_3)} \tag{2.22}$$

with the introduction of two parameters: $R(x_3)$ represents a wave front radius of curvature which varies as the Gaussian beam propagates, while $w(x_3)$ represents the already mentioned beam width parameter that defines the radial distance to which the beam amplitude drops by a factor e^{-1} from its on-axis value. Eq 2.19 becomes

$$p(\mathbf{x},\omega) = P(0)e^{ik_p x_3}\frac{q(0)}{q(x_3)}e^{\frac{ik(x_1^2+x_2^2)}{2R(x_3)}}e^{-\frac{(x_1^2+x_2^2)}{w^2(x_3)}} \tag{2.23}$$

The parameters $R(x_3)$ and $w^2(x_3)$. Here are simply reported:

$$R(x_3) = (x_3 - x_{03}) + \frac{x_{R3}^2}{(x_3 - x_{03})} \tag{2.24}$$

$$w(x_3) = w_0\sqrt{1 + \frac{(x_3 - x_{03})^2}{x_{R3}^2}} \tag{2.25}$$

In laser field, most of the discussion about Gaussian beams is for circular cross-section beams, since the most common interactions with mirrors, lenses and other optical components maintain the original circular cross-section.

In ultrasonic, this is not always true. Even though a beam starts with a circular cross-section, after transmission and reflection from interfaces, the expression for $\mathbf{M}_p(x_3)$ has to be treated in a more general form, a complex 2x2 symmetric matrix. Like the previous case, as long as the two eigenvalues of $M_m^I(x_3) \equiv \mathrm{Im}\left[\mathbf{M}_p(x_3)\right]$ with $m = (1,2)$ satisfy $M_m^I(x_3) > 0$, the general solution 2.10 represents a wave with an elliptical Gaussian profile which decays from the x_3 axis. If the Gaussian beam starts at $x_3 = x_{03} = 0$ with eigenvalues of $M_m^I(0) > 0$, then during propagation the eigenvalues of the propagated matrix $M_m^I(x_3)$ will also satisfy the same inequality, since the *propagation law* Eq. 2.13 shows that only the real parts of the eigenvalues of $\mathbf{M}_p^{-1}$ are affected during propagation. Thus a localized Gaussian at $x_3 = 0$ always generates a localized propagating Gaussian beam, just as in the circular cross-section case. Like for the definition 2.22, the eigenvalues of real parts $M_m^R(x_3) \equiv \mathrm{Re}\left[\mathbf{M}_p(x_3)\right]$ are related to the principal wave front curvature. However, the directions of these principal curvature are different from the directions associated with the eigenvalues of $M_m^I(x_3)$, which are related to the principal beam widths for a Gaussian beam of elliptical cross section. It can be defined

$$M_m^I(x_3) = \frac{\lambda}{\pi c_p w_m^2(x_3)} \tag{2.26}$$

$$M_m^R(x_3) = \frac{1}{c_p R_m(x_3)} \tag{2.27}$$

with $m = 1,2$, R_m and w_m principal radii of curvature and beam widths. The expression Eq.2.17 can be written as

$$p(\mathbf{x},\omega) = P(0)e^{ik_p x_3}\sqrt{\frac{\det\left[\mathbf{M}_p(x_3)\right]}{\det\left[\mathbf{M}_p(0)\right]}}e^{\frac{ik_p}{2}\left(\frac{\eta_1^2}{R_1}+\frac{\eta_2^2}{R_2}\right)}e^{-\left(\frac{\xi_1^2}{w_1^2}+\frac{\xi_2^2}{w_2^2}\right)} \tag{2.28}$$

where (η_1,η_2) and (ξ_1,ξ_2) are the principal axes for the imaginary and real parts of the $\mathbf{M}_p$ matrix. The orientation of both these axes are function of x_3. Fig. 2.5 clarifies the situation.

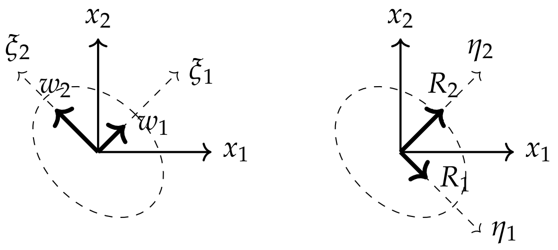

Figure 2.5: *Left*: the principal beam widths with their directions where the beam amplitude fell off to e^{-1} of its beam axis value. *Right*: the principal wave front radii of curvature, along with their directions.

An important difference between the two expression is that the scalar one and that in matrix form regards the square root terms appearing in the latter equation. Since the matrix $\mathbf{M}_p$ is complex and the principal curvature and beam width directions are not aligned in general, some attention must be taken in evaluating those square roots.

In many cases, Gaussian beams problems have the $\mathbf{M}_p$ matrix diagonal

$$\mathbf{M}_p(x_3) = \begin{bmatrix} M_1(x_3) & 0 \\ 0 & M_2(x_3) \end{bmatrix} \tag{2.29}$$

and the ratio in the Gaussian beam expression becomes

$$\frac{P(x_3)}{P(0)} = \frac{\sqrt{\det\left[\mathbf{M}_p(x_3)\right]}}{\sqrt{\det\left[\mathbf{M}_p(0)\right]}} = \frac{\sqrt{M_1(x_3)}\sqrt{M_2(x_3)}}{\sqrt{M_1(0)}\sqrt{M_2(0)}}. \tag{2.30}$$

Because the imaginary parts of $M_m(0)$ and $M_m(x_3)$ are always positive, the individual square roots in 2.30 must be taken to have positive imaginary parts. For the more general case where $\mathbf{M}_p$ is not diagonal, although the principal directions of the real and imaginary parts of $\mathbf{M}_p$ do not coincide, the real part of $\mathbf{M}_p$ is a real, symmetrical matrix and the imaginary part is a real, symmetrical and positive definite matrix (see [4] for details). Under these conditions, from linear algebra theory [9], it is always possible to define a generalized eigenvalue problem where a real 2x2 transformation matrix $\mathbf{T}$ *simultaneously* diagonalizes both the real and the imaginary parts of $\mathbf{M}_p$. Knowing this transformation matrix, the term can be rearranged to be

$$\frac{\sqrt{\det\left[\mathbf{T}^T(x_3)\mathbf{M}_p(x_3)\mathbf{T}(x_3)\right]}}{\sqrt{\det\left[\mathbf{T}^T(0)\mathbf{M}_p(0)\mathbf{T}(0)\right]}} = \frac{\sqrt{\tilde{M}_1(x_3)}\sqrt{\tilde{M}_2(x_3)}}{\sqrt{\tilde{M}_1(0)}\sqrt{\tilde{M}_2(0)}}. \tag{2.31}$$

The complex $\tilde{M}_m(0)$, $\tilde{M}_m(x_3)$ terms are the diagonal matrix terms obtained after applying the transformation matrices to $\mathbf{M}_p$. The tilde over these quantities shows that these complex quantities are not the same as the complex values given in 2.30; however, the square roots on the right sides of 2.31 can be found in the same fashion of the remaining real determinant

$$
\begin{aligned}
\frac{P(x_3)}{P(0)} &= \frac{\sqrt{\det\left[\mathbf{M}_p(x_3)\right]}}{\sqrt{\det\left[\mathbf{M}_p(0)\right]}} \\
&= \frac{\sqrt{\det^2\left[\mathbf{T}(0)\right]}}{\sqrt{\det^2\left[\mathbf{T}(x_3)\right]}} \frac{\sqrt{\tilde{M}_1(x_3)}\sqrt{\tilde{M}_2(x_3)}}{\sqrt{\tilde{M}_1(0)}\sqrt{\tilde{M}_2(0)}}
\end{aligned}
\tag{2.32}
$$

2.3 GAUSSIAN BEAMS IN SOLIDS

When dealing with solid materials, elastic waves can be describes in terms of elastic potentials [1], [23], [24]. Unlike the governing equations for a fluid, Navier equations are not in general wave equations for the displacement or velocity fiels. Their form is in fact:

$$\rho \frac{\partial^2 \mathbf{u}}{\partial t^2} = \mathbf{f} + \mu \nabla^2 \mathbf{u} + (\lambda + \mu) \boldsymbol{\nabla}(\boldsymbol{\nabla} \cdot \mathbf{u}) \tag{2.33}$$

with ρ density of the material, λ and μ Lamé parameters. However, Navier equations could be decompose to describe two distinct wavefields. The displacement vector (written as usually $\mathbf{u}$) can be decomposed into a *scalar* potential ϕ and a *vector* potential $\boldsymbol{\Psi}$, in this form

$$\mathbf{u} = \boldsymbol{\nabla}\phi + \boldsymbol{\nabla} \times \boldsymbol{\Psi} \tag{2.34}$$

Placing this decomposition into the Navier equation, setting the body force $\mathbf{f} = 0$ and using the fact that the divergence of the curl is zero, it's found the two wave equations

$$\nabla^2 \phi - \frac{1}{c_p} \frac{\partial^2 \phi}{\partial t^2} = 0 \tag{2.35}$$

$$\nabla^2 \boldsymbol{\Psi} - \frac{1}{c_s} \frac{\partial^2 \boldsymbol{\Psi}}{\partial t^2} = 0. \tag{2.36}$$

The displacement potentials satisfy the wave equations, so they also can have paraxial Gaussian beam solutions

$$\phi = \Phi(x_3) e^{i k_p x_3} e^{i \frac{\omega}{2} \mathbf{X}^T \mathbf{M}_p(x_3) \mathbf{X}} \tag{2.37}$$

$$\psi = \Psi(x_3) e^{i k_s x_3} e^{i \frac{\omega}{2} \mathbf{X}^T \mathbf{M}_s(x_3) \mathbf{X}} \tag{2.38}$$

At high frequencies the velocity $\mathbf{v}^\alpha (\alpha = p, s)$ for a P-wave or S-wave is obtained by differentiating the $e^{i k_\alpha x_3}$ terms in these equation

$$\mathbf{v}^\alpha = V^\alpha(x_3) \mathbf{d}^\alpha e^{i k_\alpha x_3} e^{i \frac{\omega}{2} \mathbf{X}^T \mathbf{M}_\alpha(x_3) \mathbf{X}} \qquad (\alpha = p, s) \tag{2.39}$$

with $V^p = \omega^2 \Phi / c_p$, $V^s = \omega^2 \Psi / c_s$ and $\mathbf{d}^p = \mathbf{e}_3$, $\mathbf{d}^s = \mathbf{e}_3 \times \mathbf{t}$, where $\mathbf{e}_3$ is a unit vector in the x_3 direction. Note that these relations are identical in form to those for a plane wave since in a plane wave $e^{ik_\alpha x_3}$ is the only spatially varying term present.

Another approach uses an high frequency approximation of Navier equations for the displacements in the quasi-plane wave form [4]

$$u_i = \tilde{U}_i(x_1, x_2, x_3)e^{ik_s x_3} \tag{2.40}$$

which leads to the paraxial wave equation

$$\frac{\partial^2 \tilde{U}_3}{\partial x_1^2} + \frac{\partial^2 \tilde{U}_3}{\partial x_2^2} + 2ik_p \frac{\partial \tilde{U}_3}{\partial x_3} = 0 \qquad \text{with } \tilde{U}_1 = \tilde{U}_2 = 0 \text{ for P-waves} \tag{2.41}$$

$$\frac{\partial^2 \tilde{U}_I}{\partial x_1^2} + \frac{\partial^2 \tilde{U}_I}{\partial x_2^2} + 2ik_s \frac{\partial \tilde{U}_I}{\partial x_3} = 0 \quad \text{with } (I = 1, 2) \text{ for S-waves and } \tilde{U}_3 = 0. \tag{2.42}$$

The vector form is therefore

$$\mathbf{u}^\alpha = U^\alpha(x_3)\mathbf{d}^\alpha e^{ik_\alpha x_3} e^{\frac{i\omega}{2}\mathbf{X}^T\mathbf{M}_\alpha(x_3)\mathbf{X}} \qquad (\alpha = p, s), \tag{2.43}$$

by taking a derivative $\mathbf{v}^\alpha = -i\omega\mathbf{u}^\alpha$, $V^\alpha(x_3) = -i\omega U^\alpha(x_3)$. Now, like the steps outlined for the fluid case, these Gaussian beam solutions must satisfy the *transport* and *Riccati* equation already seen 2.12, but in terms of V^α:

$$\frac{2}{c_\alpha}\frac{\mathrm{d}V^\alpha}{\mathrm{d}x_3} + V^\alpha \operatorname{tr}(\mathbf{M}_\alpha) = 0 \tag{2.44}$$

$$\frac{1}{c_\alpha}\frac{\mathrm{d}\mathbf{M}_\alpha}{\mathrm{d}x_3} + \mathbf{M}_\alpha^2 = 0. \tag{2.45}$$

Again, the solutions are

$$\mathbf{M}_\alpha(x_3) = \mathbf{M}_\alpha(0)\left[\mathbf{I} + c_\alpha x_3 \mathbf{M}_\alpha(0)\right]^{-1} \tag{2.46}$$

and

$$\begin{aligned}\frac{V^\alpha(x_3)}{V^\alpha(0)} &= \sqrt{\frac{\det\left[\mathbf{M}_\alpha^{-1}(0)\right]}{\det\left[\mathbf{M}_\alpha^{-1}(x_3)\right]}} = \sqrt{\frac{\det\left[\mathbf{M}_\alpha(x_3)\right]}{\det\left[\mathbf{M}_\alpha(0)\right]}} \\ &= \frac{1}{\sqrt{\det\left[\mathbf{I} + c_\alpha x_3\mathbf{M}_\alpha(0)\right]}}\end{aligned} \tag{2.47}$$

so that the velocity in the solid for a Gaussian beam of type $\alpha = p, s$ is

$$\mathbf{v}^\alpha = V^\alpha(0)\mathbf{d}^\alpha \frac{\sqrt{\det\left[\mathbf{M}_\alpha(x_3)\right]}}{\sqrt{\det\left[\mathbf{M}_\alpha(0)\right]}} e^{ik_\alpha x_3} e^{\frac{i\omega}{2}\mathbf{X}^T\mathbf{M}_\alpha(x_3)\mathbf{X}} \tag{2.48}$$

is almost identical to the expression for fluid, except the polarization vector (Eq. 2.18)

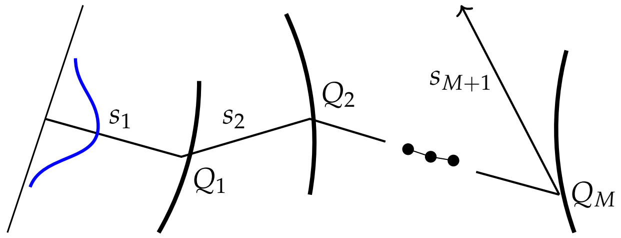

Figure 2.6: Gaussian beams: transmission and reflection across multiple media

2.4 THE ABCD MATRIX FORMALISM

For the mathematical properties of Gaussian beams, when an initial beam starts out localized it remains localized during propagation and after interaction with general curved surfaces. Furthermore, propagation and interface transformation laws can be combined to obtain the form of Gaussian beam after multiple interaction with these surfaces.

Consider the general case where a Gaussian beam travels through or is reflected from M interfaces. Applying propagation and transmission/reflection laws to each medium and interface, yield this expression for velocity of Gaussian beam of type α in medium $M+1$:

$$\begin{aligned}\mathbf{v}^{\alpha;y}_{M+1} = {} & \frac{\sqrt{\det\left[\mathbf{M}^{\alpha}_{M+1}(s_{M+1})\right]}}{\sqrt{\det\left[\mathbf{M}^{\alpha}_{M+1}(0)\right]}} \cdot \\ & \cdot \left[\prod_{m=M}^{1} \mathbf{T}^{\gamma_{m+1};\gamma_m}_{m} \frac{\sqrt{\det\left[\mathbf{M}^{\gamma_m}_{m}(s_m)\right]}}{\sqrt{\det\left[\mathbf{M}^{\gamma_m}_{m}(0)\right]}}\right] \cdot \\ & \cdot V^{\gamma_1}_1(0)\mathbf{d}^{\gamma_1}_1 \exp\left[i\omega \sum_{m=1}^{M+1} \frac{s_m}{c^{\gamma_m}_m} + i\frac{\omega}{2}\mathbf{y}^T\left[\hat{\mathbf{M}}^{\alpha}_{M+1}(s_{M+1})\right]\mathbf{y}\right]. \end{aligned} \tag{2.49}$$

where s_m is the distance the beam has travelled in medium m along its central axis and γ_m is the wave mode (γ_m = P, SV, SH). This situation is depicted in Fig. 2.6.

The matrix $\mathbf{T}^{\gamma_{m+1};\gamma_m}_m$ represents the transmission/reflection coefficient between the medium m and $m+1$. Since this is the general case of a beam which might have polarization vectors not on the POI. That requires coordinate transformation by the $\mathbf{G}$ matrices. In additions, the product has to be taken in reverse order:

$$\mathbf{T}^{\gamma_{M+1};\gamma_M}_M \mathbf{T}^{\gamma_M;\gamma_{M-1}}_{M-1} \dots \mathbf{T}^{\gamma_2;\gamma_1}_1. \tag{2.50}$$

However, in the following it will be used the matrix form of the transmission/reflection coefficients, even though the scalar form it will be sufficient in the analysed cases. At the m-th interface is valid the relation $\mathbf{M}^{\gamma_m}_m(s_m) = \mathbf{M}^{\gamma_m}_m(Q_m)$, if s_m represents the distance travelled by the beam until it reaches the point Q_m. This point will be the starting point for the medium $m+1$, so $\mathbf{M}^{\gamma_{m+1}}_{m+1}(0) = \mathbf{M}^{\gamma_{m+1}}_{m+1}(Q_m)$. This situation is depicted in Fig. 2.7. The Gaussian beam experiences two different phases: propagation,

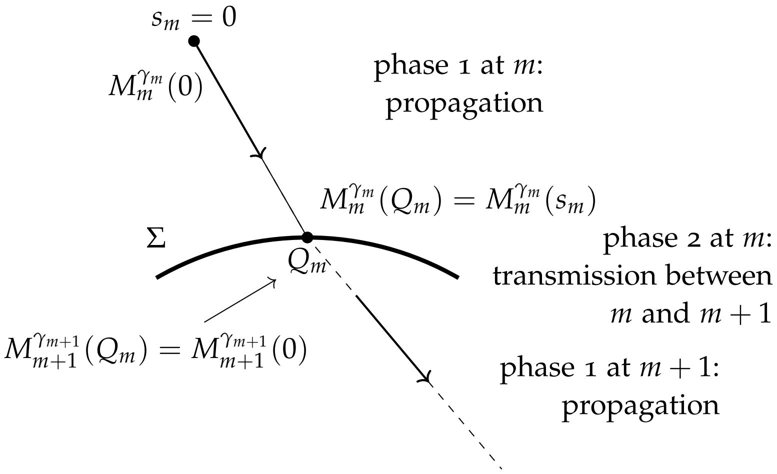

Figure 2.7: The notations used in the m-th interface.

along the direction of the central beam axis, and transmission/reflection at the next interface.

From the expression of Gaussian beams (2.49), the computation of each term can be simplified in a modular way using the **A**, **B**, **C**, **D** formulation, analogous to those used in optics (scalar formulation). Indeed , both propagation and transmission laws for $\mathbf{M}_m^{\gamma_m}$ can be written in a common form. Let's consider the propagation law first 2.14 for the fluid case

$$\mathbf{M}_p(x_3) = \mathbf{M}_p(0)\left[\mathbf{I} + c_p x_3 \mathbf{M}_p(0)\right]^{-1},$$

in a more general way it can be written as

$$\mathbf{M}_m^{\gamma_m}(s_m) = \left[\mathbf{D}_m^d \mathbf{M}_m^{\gamma_m}(0) + \mathbf{C}_m^d\right]\left[\mathbf{A}_m^d + \mathbf{B}_m^d \mathbf{M}_m^{\gamma_m}(0)\right]^{-1} \tag{2.51}$$

with the following choice made for the matrices structure:

$$\mathbf{A}_m^d = \mathbf{D}_m^d = \mathbf{I}, \qquad \mathbf{B}_m^d = c_m^{\gamma_m} s_m \mathbf{I}, \qquad \mathbf{C}_m^d = \mathbf{0}. \tag{2.52}$$

I and **0** are the identity and zero matrices, where s_m represents the beam central distance instead of x_3 and the superscript d stays for *displacement*.

Let's consider now the transmission law for the **M** matrix, Eq. (**??**)), rewritten as

$$\mathbf{M}_{m+1}^{\gamma_{m+1}}(Q_m) = \left[\left[\tilde{\mathbf{G}}^C\right]^{-1}\mathbf{G}\mathbf{M}_m^{\gamma_m}(Q_m) + \left[\tilde{\mathbf{G}}^C\right]^{-1}\mathbf{h}(Q_m)\left(\frac{\cos\theta_m^{\gamma_m}}{c_m^{\gamma_m}} - \frac{\cos\theta_{m+1}^{\gamma_{m+1}}}{c_{m+1}^{\gamma_{m+1}}}\right)\left[\left[\mathbf{G}^C\right]^T\right]^{-1}\right]\left[\left[\tilde{\mathbf{G}}^C\right]^{-1}\mathbf{G}^C\right]^T. \tag{2.53}$$

which could be mutated in

$$\mathbf{M}_{m+1}^{\gamma_{m+1}}(Q_m) = \left[\mathbf{D}_m^t \mathbf{M}_m^{\gamma_m}(Q_m) + \mathbf{C}_m^t\right]\left[\mathbf{A}_m^t + \mathbf{B}_m^t \mathbf{M}_m^{\gamma_m}(Q_m)\right]^{-1}. \tag{2.54}$$

The choice for the matrices are:

$$\begin{aligned}\mathbf{A}_m^t &= \left[\tilde{\mathbf{G}}^C\right]^T \left[\left[\mathbf{G}^C\right]^T\right]^{-1} \\ &= \begin{bmatrix}\cos\lambda & -\sin\lambda \\ \sin\lambda & \cos\lambda\end{bmatrix} \begin{bmatrix}\frac{\cos\theta_{m+1}^{\gamma_{m+1}}}{\cos\theta_m^{\gamma_m}} & 0 \\ 0 & 1\end{bmatrix} \begin{bmatrix}\cos\lambda & \sin\lambda \\ -\sin\lambda & \cos\lambda\end{bmatrix}\end{aligned} \tag{2.55}$$

$$\mathbf{B}_m^t = \mathbf{0} \tag{2.56}$$

$$\begin{aligned}\mathbf{C}_m^t &= \left(\frac{\cos\theta_m^{\gamma_m}}{c_m^{\gamma_m}} - \frac{\cos\theta_m^{\gamma_{m+1}}}{c_{m+1}^{\gamma_{m+1}}}\right) \left[\tilde{\mathbf{G}}^C\right]^{-1} \mathbf{h}(Q_m) \left[\left[\mathbf{G}^C\right]^T\right]^{-1} \\ &= \left(\frac{\cos\theta_m^{\gamma_m}}{c_m^{\gamma_m}} - \frac{\cos\theta_m^{\gamma_{m+1}}}{c_{m+1}^{\gamma_{m+1}}}\right) \begin{bmatrix}\cos\lambda & -\sin\lambda \\ \sin\lambda & \cos\lambda\end{bmatrix} \cdot \\ &\begin{bmatrix}\frac{h_{11}}{\cos\theta_m^{\gamma_m}\ \cos\theta_{m+1}^{\gamma_{m+1}}} & \frac{h_{12}}{\cos\theta_{m+1}^{\gamma_{m+1}}} \\ \frac{h_{21}}{\cos\theta_m^{\gamma_m}} & h_{22}\end{bmatrix} \begin{bmatrix}\cos\lambda & \sin\lambda \\ -\sin\lambda & \cos\lambda\end{bmatrix}\end{aligned} \tag{2.57}$$

$$\begin{aligned}\mathbf{D}_m^t &= \left[\tilde{\mathbf{G}}^C\right]^{-1} \mathbf{G}^C \\ &= \begin{bmatrix}\cos\lambda & -\sin\lambda \\ \sin\lambda & \cos\lambda\end{bmatrix} \begin{bmatrix}\frac{\cos\theta_m^{\gamma_m}}{\cos\theta_{m+1}^{\gamma_{m+1}}} & 0 \\ 0 & 1\end{bmatrix} \begin{bmatrix}\cos\lambda & \sin\lambda \\ -\sin\lambda & \cos\lambda\end{bmatrix}.\end{aligned} \tag{2.58}$$

where t stays for "transmission". With this representation, the two phases (displacement + transmission) can be represented in an uniform way. For example, consider a Gaussian beam in medium m starting from $s_m = 0$ (with $\mathbf{M}_m^{\gamma_m}(0)$), travelling a distance s_m to interface m (with $\mathbf{M}_m^{\gamma_m}(Q_m)$) and then transmitting across that interface to obtain $\mathbf{M}_{m+1}^{\gamma_{m+1}}(Q_m)$, the overall relationship can be written as

$$\mathbf{M}_{m+1}^{\gamma_{m+1}}(Q_m) = \left[\mathbf{D}\mathbf{M}_m^{\gamma_m}(0) + \mathbf{C}\right] \left[\mathbf{A} + \mathbf{B}\mathbf{M}_m^{\gamma_m}(0)\right]^{-1} \tag{2.59}$$

where the $\mathbf{A}$, $\mathbf{B}$, $\mathbf{C}$ and $\mathbf{D}$ matrices are given by the matrix product of the propagation and the transmission matrices in the 4x4 form:

$$\begin{bmatrix}\mathbf{A} & \mathbf{B} \\ \mathbf{C} & \mathbf{D}\end{bmatrix} = \begin{bmatrix}\mathbf{A}_m^t & \mathbf{B}_m^t \\ \mathbf{C}_m^t & \mathbf{D}_m^t\end{bmatrix} \cdot \begin{bmatrix}\mathbf{A}_m^d & \mathbf{B}_m^d \\ \mathbf{C}_m^d & \mathbf{D}_m^d\end{bmatrix} \tag{2.60}$$

To obtain this, simply substitute in the transmission law (2.54) the expression for $\mathbf{M}$ of the propagation law (2.51), and then rearrange to obtain the result in form of 2.60.

The interesting property is that this process of combination can continue for any additional number of material and interfaces. The extension, from medium 1 to $M+1$ is straightforward: the final $\mathbf{M}$ matrix in the last material at distance s_{M+1} from the M-th interface is directly related to the first $\mathbf{M}$ matrix in medium 1, in terms of the *global* matrices $\mathbf{A}^G$, $\mathbf{B}^G$, $\mathbf{C}^G$, $\mathbf{D}^G$ as

$$\mathbf{M}_{M+1}^{\gamma_{M+1}}(s_{M+1}) = \left[\mathbf{D}^G\mathbf{M}_1^{\gamma_1}(0) + \mathbf{C}^G\right] \left[\mathbf{A}^G + \mathbf{B}^G\mathbf{M}_1^{\gamma_1}(0)\right]^{-1} \tag{2.61}$$

with the matrices given by the product of *all* the contributing propagation and transmission matrices

$$\begin{aligned}\begin{bmatrix}\mathbf{A}^G & \mathbf{B}^G\\ \mathbf{C}^G & \mathbf{D}^G\end{bmatrix} = & \begin{bmatrix}\mathbf{A}^d_{M+1} & \mathbf{B}^d_{M+1}\\ \mathbf{C}^d_{M+1} & \mathbf{D}^d_{M+1}\end{bmatrix} \cdot \begin{bmatrix}\mathbf{A}^t_{M} & \mathbf{B}^t_{M}\\ \mathbf{C}^t_{M} & \mathbf{D}^t_{M}\end{bmatrix} \cdot \\ & \begin{bmatrix}\mathbf{A}^d_{M} & \mathbf{B}^d_{M}\\ \mathbf{C}^d_{M} & \mathbf{D}^d_{M}\end{bmatrix} \cdot \begin{bmatrix}\mathbf{A}^t_{M-1} & \mathbf{B}^t_{M-1}\\ \mathbf{C}^t_{M-1} & \mathbf{D}^t_{M-1}\end{bmatrix} \cdot \ldots \cdot \\ & \begin{bmatrix}\mathbf{A}^d_{1} & \mathbf{B}^d_{1}\\ \mathbf{C}^d_{1} & \mathbf{D}^d_{1}\end{bmatrix}\end{aligned} \qquad (2.62)$$

So, referring to the general formula 2.49, all the matrices appearing in that expression can be obtained via the matrix multiplication shown above. Moreover, to obtain the Gaussian beam expression for the final point, it will be need:

- Propagation/Transmission/Reflection matrices **A**, **B**, **C**, **D** at each stage for each specified set of wave type;
- plane wave Transmission/Reflection coefficients to compute the $\mathbf{T}_m^{\gamma_m;\gamma_{m+1}}$ matrix;
- the velocity $V_1^{\gamma_1}(0)\ \mathbf{d}_1^{\gamma_1}$;
- the phase matrix $\mathbf{M}_1^{\gamma_1}(0)$ at the starting point in the first medium.

2.5 MULTI-GAUSSIAN TRANSDUCER BEAM MODEL

The mathematical formalism seen so far now comes useful for the description and construction of the ultrasonic field transducer and build the solution for the specific study. The method is based on superposition of Gaussian beams, to represent a model of piston transducer and then analytically transmit or reflect those beams from interfaces. Furthermore, there's the advantage that the surface interface are planar or, at most, slightly curved (for example at the interface between Rexolite and water). The advantages of these *Multi-Gaussian Beam model* are

1. The superposition of a relatively few Gaussian beams can accurately predict the wave fields of either focused or un-focused circular transducers;
2. no numerical ray tracing is needed sinche all the Gaussian propagates along a fixed ray from the centre of the transducer, normal to its face;
3. no numerical integration is required for multi-gaussian beam models.[3]

Starting from these consideration, [27] demonstrated that a sound beam from a circular piston transducer radiating into water can be simulated using

---

[3] Here is not considered the integration to calculate the *elastic/acoustic transfer function* $t_A(\omega)$ which is a fundamental property to allow a complete description of an UMS.

the superposition of as few as ten or even fifteen Gaussian beams. These Gaussian beams are weighted by a set of complex-valued coefficient that have to be determined, through a minimization procedure expalined in [28]. The only condition to be met is $(ka)^2 \gg 1$, where k is the wavenumber and a the radius of the transducer. On the face or a transducer of radius a located on a plane at $x_3 = 0$, radiating into a region $x_3 > 0$, the authors had shown that the normalized velocity field can be written as

$$\frac{\mathbf{v}^p(x_1, x_2, 0; \omega)}{v_0(\omega)} = \sum_{i=1}^{15} A_r \mathbf{d}^p e^{-\frac{B_r \rho^2}{a^2}} \tag{2.63}$$

where $\rho^2 = x_1^2 + x_2^2$, $v_0(\omega)$ is the constant velocity on the transducer face and $\mathbf{d}^p = \mathbf{e}_3 = (0, 0, 1)$. The right hand side of the previous equation is nothing but the series of base functions (superposition) to reproduce the field solution, approximated with the $(ka)^2 \gg 1$, valid for this method.

For a circular *planar* piston transducer of radius a, the normalized velocity field in the x_3-direction, v_3/v_0 is given by the *circ function*, where

$$\frac{v_3(x_1, x_2, 0, \omega)}{v_0(\omega)} = \begin{cases} 1 & \rho^2/a^2 < 1 \\ 0 & \text{otherwise} \end{cases} \equiv \text{circ}\left(\rho^2/a^2\right). \tag{2.64}$$

So the base functions coefficients are obtained minimizing an objective function, given by

$$J(A_r, B_r) = \int_0^\infty \left[\text{circ}\left(\frac{\rho^2}{a^2}\right) - \sum_{i=1}^{15} A_r e^{-B_r \frac{\rho^2}{a^2}} \right]^2 d\rho. \tag{2.65}$$

Once the coefficient have been calculated, it's not necessary to re-compute each time their value, if the transducer of the problem remains the same, *i.e.* planar and circular. For each Gaussian beams there will be values of

$$\left[V_1^p(0)\right]_r = A_r v_0(\omega) \tag{2.66}$$

$$\left[\mathbf{M}_1^p(0)\right]_r = \begin{bmatrix} \frac{iB_r}{c_{p1} D_R} & 0 \\ 0 & \frac{iB_r}{c_{p1} D_R} \end{bmatrix} \tag{2.67}$$

Here $D_R = k_{p1} a^2/2$ is the *Rayleigh distance*, A_r and B_r are complex-valued expansion coefficients determined with the previous described procedure. The mode for the first $\mathbf{M}$ matrix is p which means P-wave, since for hypothesis the transducer is radiating in a fluid, it is the only possible mode. The wave field from a piston transducer, after multiple propagation and interface interactions, in form of a Multi-Gaussian beam model is therefore

$$\begin{aligned}\mathbf{v}_{M+1}^{\gamma_{M+1}}(\mathbf{y},\omega) = \sum_{r=1}^{15} & \frac{\sqrt{\det\left[\mathbf{M}_{M+1}^{\gamma_{M+1}}(s_{M+1})\right]_r}}{\sqrt{\det\left[\mathbf{M}_{M+1}^{\gamma_{M+1}}(0)\right]_r}} \cdot \\ & \cdot \left[\prod_{m=M}^{1} \mathbf{T}_m^{\gamma_{m+1};\gamma_m} \frac{\sqrt{\det\left[\mathbf{M}_m^{\gamma_m}(s_m)\right]_r}}{\sqrt{\det\left[\mathbf{M}_m^{\gamma_m}(0)\right]_r}}\right] \cdot \\ & \cdot \left[V_1^{\gamma_1}(0)\right]_r \mathbf{d}_1^{\gamma_1} \exp\left[i\omega \sum_{m=1}^{M+1} \frac{s_m}{c_m^{\gamma_m}} + i\frac{\omega}{2}\mathbf{y}^T \left[\hat{\mathbf{M}}_{M+1}^{\gamma_{M+1}}(s_{M+1})\right]\mathbf{y}\right]. \end{aligned} \tag{2.68}$$

The reliability of this approach is based on the effectiveness of reproducing the piston transducer wave field to within the limits of the paraxial approximation. These limits are accurate at distances of approximately one transducer diameter or greater from the transducer face.

Again from [28], it is reported a similar procedure to determine a set of 15 optimized coefficients. The authors use the normalized exact on-axis pressure calculated analytically from Rayleight-Sommerfeld integral, corresponding to

$$\tilde{p}_{exact}(x_3,\omega) = \frac{p(0,0,x_3,\omega)}{\rho_1 c_{p1} v_0} = e^{ik_{p1}x_3} - e^{ik_{p1}\sqrt{a^2+x_3^2}} \tag{2.69}$$

and a 15 term multi-Gaussian beam model for this same field:

$$\tilde{p}_{MG}(x_3,\omega) = \sum_{r=1}^{15} \frac{A_r}{1+iB_r x_3/D_R} e^{ik_{p1}x_3} \tag{2.70}$$

with the definition of a new objective function

$$\begin{aligned} J(A_r,B_r) = \int_0^\infty & \left[\operatorname{circ}\left(\frac{\rho^2}{a^2}\right) - \sum_{r=1}^{15} A_r e^{-B_r\frac{\rho^2}{a^2}}\right]^2 d\rho \\ & + \lambda_w \int_{z_1}^{z_2} \left[\left|\tilde{p}_{exact}(x_3,\omega)\right| - \left|\tilde{p}_{MG}(x_3,\omega)\right|\right]^2 dx_3 \end{aligned} \tag{2.71}$$

where λ_w is a constant to weight the on-axis matching conditions relative to the boundary matching conditions and z_1 and z_2 are near field limit values that define the range where matching to on-axis field take place. An easy verification for a simple configuration is the evaluation of the normalized on-axis pressure wave field obtained for a single medium, given by the multi-Gaussian beam model as

$$\frac{p(x_1,x_2,x_3,\omega)}{\rho_1 c_{p1} v_0(\omega)} = \sum_{r=1}^{15} \frac{A_r}{1+iB_r x_3/D_R} e^{ik_{p1}x_3} e^{i\omega\left(\frac{1}{2}\mathbf{x}^T\left[\hat{\mathbf{M}}_1^p(x_3)\right]_r\mathbf{x}\right)} \tag{2.72}$$

where

$$\left[\hat{\mathbf{M}}_1^p(x_3)\right]_r = \begin{bmatrix} \frac{\frac{iB_r}{c_{p1}D_R}}{1+\frac{iB_r x_3}{D_R}} & 0 & 0 \\ 0 & \frac{\frac{iB_r}{c_{p1}D_R}}{1+\frac{iB_r x_3}{D_R}} & 0 \\ 0 & 0 & 0 \end{bmatrix} \tag{2.73}$$

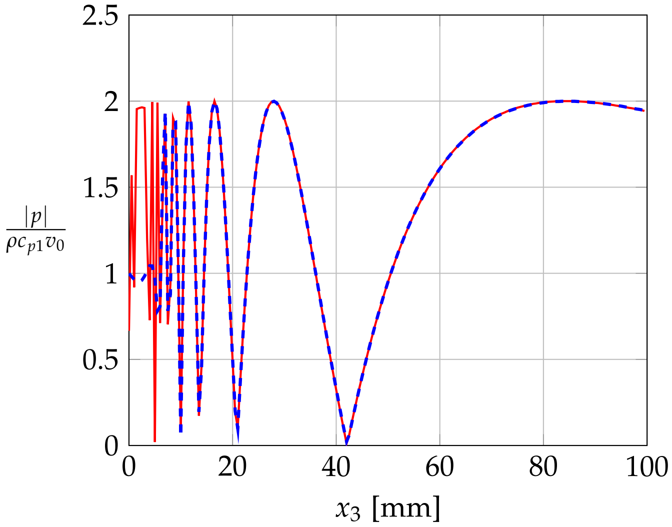

Figure 2.8: Plot comparison of on-axis pressure for a 5 mm radius piston transducer radiating into water at 5 MHz. Exact solution (red) by the Rayleigh-Sommerfeld integral and by a superposition of 15 Gaussian beams by optimized coefficients (blue dashed), computed with the implemented model.

Fig.2.8 shows the comparison of the exact result (Eq.2.69) and the approximated one, obtained with this model. Notice that, starting from about 10 mm from the transducer face located at $x_3 = 0$, the calculated field agrees perfectly with the analytical profile.

A nice property of this approach is that it's practical and easy to obtain models for focused transducer, simply by modification of the B_r coefficients. For a spherical focused transducer of radius a and geometrical focal length F this corresponds to specifying the velocity field at the transducer as

$$\frac{v_3(x_1, x_2, 0, \omega)}{v_0(\omega)} = \text{circ}\left(\frac{\rho^2}{a^2}\right) e^{-ik_{p1}\frac{\rho^2}{2F}}, \tag{2.74}$$

since the Multi-Gaussian beam model can be viewed as an approximation of the *circ* function in the form

$$\text{circ}\left(\frac{\rho^2}{a^2}\right) = \sum_{r=1}^{15} A_r e^{-B_r \frac{\rho^2}{a^2}}. \tag{2.75}$$

Eq. 2.74 includes the effects of spherical focusing so there's the need to modify the B_r coefficients for the circular planar transducer case by making

$$B'_r = B_r + \frac{ik_{p1}a^2}{2F}. \tag{2.76}$$

2.6 STANDARDS IN ULTRASONIC SYSTEM DESIGN

Even in the field of ultrasonic measurements there are reference guidelines that explain how to choose the basic parameters that characterize transducers. ASTM, the American Society for Testing and Materials, is the international body that sets these standards and periodically publishes these standards for a wide range of test materials and systems. These guidelines were helpful in choosing the key parameters to consider for the selection of ultrasonic transducers, and how to design the experimental tests. For example, tests measuring acoustic wave velocity at room temperature were done for the inspected materials, but these are not reported in this work because they are redundant. Moreover, such data are already found tabulated in the literature.

2.6.1 Velocity measurement in thick metal

The ASTM E 494 *Standard Practice for Measuring Ultrasonic Velocity* states the requirements to determine the inspected object properties such as velocity of the L-wave. The signal pattern should contain several back reflections that are clearly separated. It is recommended to set an inital signal amplitude to cleary measure more than a few replicates on the signal, highly above the noise level. The number of multiple reflections should be as many as possible. Then the system acquires the sampled signal and the distances in time -TOF- should be determined.

The other notation that will be used in the Chapter of the results for the acoustic velocity of longitudinal waves is simply v_p. So, To calculate ultrasonic velocity v_p, the cumulated distance should be divided by the measured TOF:

$$v_p = \frac{(n-1) \times 2L}{\sum \Delta t} \tag{2.77}$$

where L is the thickness of the sample, n the number of back reflections, $\sum \Delta t$ the total measured TOF.

THe ASTM E 494 requires some specification on the interval of used frequencies, and sample sizes.

2.6.2 Velocity measurement in wedge materials

The same method used for the metals recommended by the ASTM E 494 Standard is not suitable for velocity measurements in wedge materials [3]. There are two other methods for achieving this scope: contact method and immersion method. The first method uses a single straigh beam transducer coupled with a matching layer that actually increases the thickness of the sample. The second method provide a more accurate measurement but requires special fixturing, such as a small immersion tank with two transducers, transmitter T and receiver R, mounted in line on two opposite sides of the tank. To measure the velocity, the sample is placed in the tank, approximatively in the middle of the two transducers. The measurements were performed with the first method since the simplicity of the task. Regarding this one, if the material of the matching layer has approximately the same velocity as the wedge material itself, but with a different thickness, depending on the transducer frequency, the measured velocity in the wedge material will apparently vary with the transducer frequency. This trend is

Transducer frequency [MHz]	Velocity value [mm/µs]			
	min	max	average	diff max - min %
1.0	2.52	2.72	2.65	7.35
2.25	2.60	2.745	2.715	6.46
5.0	2.705	2.746	2.732	1.49

Table 2.1: Influence of matching layer thickness on velocity measurements as a function of frequency. retrieved from [3].

observed for Plexiglas where results are reported in Tab.2.1: notice that the higher the transducer frequency used, the smaller the final velocity change. This could be a more reason for use a medium frequency range transducer ($2\,\mathrm{MHz} \leq f \leq 5\,\mathrm{MHz}$).

To eliminate the influence of the matching layer, the measurements should be performed on the two samples of the same material, but with different thickness L_1, L_2. The relative TOF for the two samples are τ_1 and τ_2. The difference in thickness $\Delta L = L_2 - L_1$ has to be divided by the difference in transit time $\Delta\tau = \tau_2 - \tau_1$ to obtain velocity in the wedge material:

$$v_p = \frac{2\,\Delta L}{\Delta\tau} \tag{2.78}$$

Again, the measurements should be made with the highest possible probe frequency to reduce the differences in the data.

2.6.3 Crystal Size Selection

The crystal size and materials are some key parameters for the overall procedure of selection of a ultrasonic transducer. Conventional sharp typically used are: round, square and rectangular. The beam shape, angular aperture and resonant frequency are parameters that depend on the crystal shape and material. For a circular or square disk the difference in beam divergence is negligible; in the case of rectangular crystals this difference is greater. There are equations that are simplifications of more complex models for determining, for example, the transition point from near to far field, thus the position of the maxima and minima, or to determine the angular aperture: in each case it is necessary to determine experimentally what the optimal condition is depending on the application. Again, the ASTM standards are very useful, in particular:

- ASTM E 114-10 Standard Practice states that *typical search unit sizes usually range from 1/8 inches (*3.2 mm*) in diameter to 1 1/8 (*28.6 mm*) in diameter.*

- ASTM E 164 recommend: *Transducer sisze recommended for weld examination range from a minimum of 1/4 inches (*6.4 mm*) diameter or 1/4 in square to 1 inches (*25.4 mm*) square or 1.1/8 inches (*28.6 mm*) diameter.*

To connect the crystal size with the frequency of oscillation , can be used another parameter, *i.e.* the product of the two factors $d \times f$. In literature it is recommended that the crystal size is selected to be in the range of $d \times f \simeq 12.5 - 125\,\mathrm{mm} \cdot \mathrm{MHz}$. The reasons behind this recommendation are mainly two. First, it's not practical to make a transducer with 6.35 mm diameter and 1 MHz of nominal frequency, due to the radial vibration mode increase with the crystal thickness and energy losses of the thickness mode. Second, the making of a transducer with 25.4 mm diameter and 10 MHz of nominal frequency, because of brittleness due to the relatively thin crystal.

2.7 CONSIDERATION ON REAL-TIME ULTRASONIC THERMOMETRY

Since the goal is to make a device for real-time temperature measurement in the harsh environment of continuous casting, the need to making modifications and customization of the instrumentation may be unavoidable. In operative scenarios such as industry process control, the ultrasonic methods allow to overcomes some limitations imposed by the environment where these control activities have to be performed. Industrial processes which are controlled by customized sensors, usually requires invasive adaptations and feasibility studies in order to install the sensors and recover useful information for the processes analysis. Another important aspect is that usually in these contexts automated sensors have to work with the minor hardware costs and less computational resources. Indeed, tasks for processes control are usually performed at low sampling rate (10 Hz), in accordance with the available hardware and resources. Generally, custom embedded electronics have to be develop in order to satisfy space, performance and resources requirements. Since in the market there aren't commerical product which satisfy all the required needs, usually, the processing of signal acquisition has to be done by an embedded device. The real-time requirement is the most demanding task for this application: The need to manage process variables as quickly as possible and have the process controller response instantaneously after the change in parameters, for example a sudden change in the level of steel in the mould, implies that the generation, acquisition and processing of the ultrasonic signal takes place in the shortest possible period and that the communication of the calculated/estimated process variables is realized via PLC. Thus, to be able to carry out the mathematical processing operations in the shortest time, the architecture for real-time involves microcontroller units which are perfectly suited to handle the generation and acquisition of ultrasonic signals.

2.7.1 Physical relation of ultrasonic speed with temperature

The relationship between ultrasonic velocity and temperature is a special property for each type of material. The law of propagation of elastic waves in a homogeneous and isotropic medium is given by Navier's equation

$$(\lambda + 2\mu)\, \boldsymbol{\nabla} \left(\boldsymbol{\nabla} \cdot \mathbf{u}\right) - \mu \left(\boldsymbol{\nabla} \times \boldsymbol{\nabla} \times \mathbf{u}\right) = \rho \frac{\partial^2 \mathbf{u}}{\partial t^2} \tag{2.79}$$

where λ and μ are the Lamé constants - μ is also called *shear modulus*-, ρ is the material density, $\mathbf{u}$ is the displacement vector. The relationship between ultrasonic speed and elastic modulus in ultrasonic wave can be given by

$$v_p = \sqrt{\frac{\lambda + 2\mu}{\rho}} = \sqrt{\frac{E(1-\sigma)}{\rho(1+\sigma)(1-2\sigma)}}, \tag{2.80}$$

$$v_s = \sqrt{\frac{\mu}{\rho}} = \sqrt{\frac{E}{2\rho(1+\sigma)}}. \tag{2.81}$$

where E is the Young modulus and σ is the Poisson ratio. As report by temperature is below the 300 °C the velocity of the copper will decrease as temperature is raising. The Young modulus of the material and the shear modulus decrease by about 40% and 36% respectevely [8]. Furthermore, as temperature rises, the Poisson ration increases slightly as well. So for isotropic material the hypothesis that the effects of temperature on ultrasonic velocitymainly depends on Poisson ratio may be realistic. Therefore the elastic modulus of metals materials decreases as temperature rises, in an approximate linear relation

$$E = E_0\,(1 - \eta T) \tag{2.82}$$

where E_0 is the Young modulus under the 0 °C, η the temperature coefficient of E and T the internal temperature, assumed to be uniform. For most metals and alloy, experimental parameters $\alpha/\eta \times 10^3 \simeq 40$, so the previous equation can be rewritten in

$$E = E_0\,(1 - 25\,\alpha T)\,. \tag{2.83}$$

Since the expression for velocities c_p and c_s have the square root, the binomial approximation is valid [4] and, since the Poisson ratio can be also assumed constant with temperature, the relationship between temperature and velocity is linear as well. This approximation is valid at least for temperature lower than 500 °C. So the final expression for the velocity may be

$$v_p = V_0\,(1 - 12.5\,\alpha T) \tag{2.84}$$

with V_0 a constant which encloses all the remaining terms which do not vary or at least have negligible temperature dependency: both the density ρ and the Poisson ratio σ influence is relative small.

2.8 CONCLUSIONS

In this Chapter, the Multi-Gaussian Beam model has been used to describe a simplified version of a reliable sensor configuration in the steel plant. This model provides a powerful tool with effective simplification in the equation to describe the behaviour of the ultrasonic fields. Furthermore, the standard directives used for implementing ultrasonic non-destructive tests and

---

[4] In the binomial approximation $(1+x)^\beta = (1+\beta x)$ for $x \ll 1$. In this case, the linear expansion coefficient for copper $\alpha \simeq 1.67 \times 10^{-5}\,°\mathrm{C}^{-1}$.

measurements have been presented, to derive right criteria for choosing the experimental components. Eventually, the physical relation describing the acoustic waves have been explored, and it has been shown how the variations of the key parameters depend on temperature.

3 RESULTS OF NUMERICAL SIMULATION

3.1 MULTI-LAYER PLANAR MATERIAL CASE

The Multi-Gaussian Beam model is usually used to describe angle-beam configurations, where the ultrasound beam path propagates through different media and across interfaces, starting from a transmitting transducer, coming to another one called receiver. A particular configuration, where the starting and arriving points coincides is the *pulse-echo* mode. The model of this physical situation is depicted in Fig.3.1. Before presenting the Multi-Gaussian Beam model for this test case, we have to do some assumptions:

- The multilayered system is made of three different materials: Rexolite, Water and copper;
- The principal axes of the beams for different media are always *orthogonal* to the surfaces because all the interfaces are planar and parallel;
- The transmission and reflection (T/R) coefficients are computed considering PP wave mode conversion;
- The model assumes infinte extension in the orthogonal direction to the parallel interfaces, so there are no rigid boundary conditions causing spourious reflection. This is due to the fact that in the real case problem the copper mould has larger extension in longitudinal axis (Chapter 2, Section 2.1);

In such a configuration, where the transducer beam can be transmitted or reflected multiple times, the use of the **A**,**B**,**C**,**D** matrices is ideal. Furthermore, a Gaussian beam that is initially described by a diagonal **M** matrix on the face of the transducer will remain a diagonal matrix after propagation and transmission/reflection.

The model (Eq. 2.68) reduce to this form

$$\begin{aligned}\mathbf{v}_{M+1}^{\gamma_{M+1}}(\mathbf{y},\omega) = \sum_{r=1}^{15} \frac{\sqrt{\det\left[\mathbf{M}_{M+1}^{\gamma_{M+1}}(s_{M+1})\right]_r}}{\sqrt{\det\left[\mathbf{M}_{M+1}^{\gamma_{M+1}}(0)\right]_r}} \cdot \\ \cdot \left[\prod_{m=M}^{1} T_m^{\gamma_{m+1};\gamma_m} \frac{\sqrt{\det\left[\mathbf{M}_m^{\gamma_m}(s_m)\right]_r}}{\sqrt{\det\left[\mathbf{M}_m^{\gamma_m}(0)\right]_r}}\right] \cdot \\ \cdot \left[V_1^p(0)\right]_r \mathbf{d}_1^p \exp\left[i\omega \sum_{m=1}^{M+1} \frac{s_m}{c_m^{\gamma_m}} + i\frac{\omega}{2}\mathbf{y}^T \left[\hat{\mathbf{M}}_{M+1}^{\gamma_{M+1}}(s_{M+1})\right]\mathbf{y}\right] \end{aligned} \quad (3.1)$$

where $T_m^{\gamma_{m+1};\gamma_m}$ is a scalar and $\gamma_m = p$ for all the layers. $[V_1^p(0)]_r$ and $[\mathbf{M}_1^p(0)]_r$ are defined in terms of the A_r, B_r coefficients. All the square root

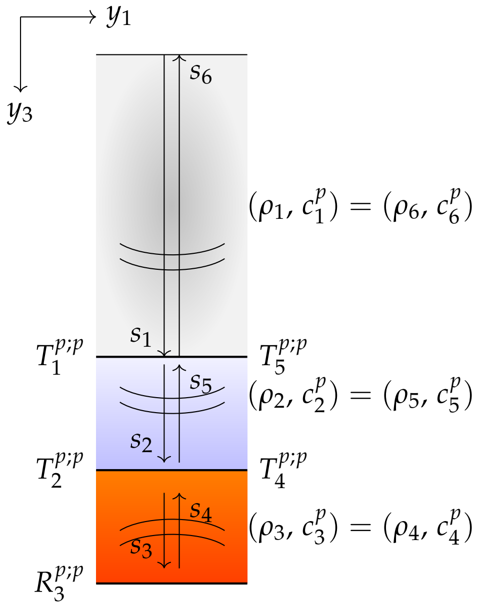

Figure 3.1: Schematic three-layer configuration used to simulate the sensor installation in the workplant. $T_n^{p;p}$ represents the *transmission coefficient* at the n-th interface; $\left(\rho_n, c_1^p\right)$ are the density and longitudinal velocity in the n-th medium, while s_n is the travel distance by the beam.

terms in Eq. 3.1 are diagonal and can be obtained directly without any transformation. At the interface between the probe and the Rexolite there is a thin layer of a couplig material, like an epoxy resin; however, the thickness of the layer does not require a model and the interface is assumed as two solid in smooth contact.

The above expression for the MGBm can be written explicitly as

$$\frac{v_n(\mathbf{y}_s,\omega)}{v_0(\omega)} = \sum_{r=1}^{15} \frac{\sqrt{[\mathbf{M}_6^p(s_6)]_r}}{\sqrt{[\mathbf{M}_6^p(0)]_r}}$$

$$T_5^{p;p}T_4^{p;p}R_3^{p;p}T_2^{p;p}T_1^{p;p}\frac{\sqrt{[\mathbf{M}_5^p(s_5)]_r}}{\sqrt{[\mathbf{M}_5^p(0)]_r}}\,\frac{\sqrt{[\mathbf{M}_4^p(s_4)]_r}}{\sqrt{[\mathbf{M}_4^p(0)]_r}}\,\frac{\sqrt{[\mathbf{M}_3^p(s_3)]_r}}{\sqrt{[\mathbf{M}_3^p(0)]_r}}\,\frac{\sqrt{[\mathbf{M}_2^p(s_2)]_r}}{\sqrt{[\mathbf{M}_2^p(0)]_r}}\,\frac{\sqrt{[\mathbf{M}_1^p(s_1)]_r}}{\sqrt{[\mathbf{M}_1^p(0)]_r}}$$

$$\frac{[V_1^p(0)]_r}{v_0}\exp\left[i\omega\left(\frac{s_1}{c_1^p}+\frac{s_2}{c_2^p}+\frac{s_3}{c_3^p}+\frac{s_4}{c_4^p}+\frac{s_5}{c_5^p}+\frac{s_6}{c_6^p}\right)+i\frac{\omega}{2}\mathbf{y}^T\left[\hat{\mathbf{M}}_6^p(s_6)\right]\mathbf{y}\right] \tag{3.2}$$

where

- $[V_1^p(0)]_r = A_r v_0(\omega)$: value of the trasnducer face velocity;
- $T_1^{p;p}$: transmission coefficient for Rexolite/water interface;
- $T_2^{p;p}$: transmission coefficient for water/copper interface;
- $R_3^{p;p}$: transmission coefficient for copper, it is assumed a solid-vacuum (no stress condition) interface;

- $T_4^{p;p}$: transmission coefficient for copper/water interface;
- $T_5^{p;p}$: transmission coefficient for Rexolite/water;
- The summation term m over the internal interfaces (from the mth to the 1st) is expanded in the second row;
- The phase term containing the path terms and the second-order term $\mathbf{y}^T\hat{\mathbf{M}}\mathbf{y}$ are in the third row. Notice that $s_1 = s_6$, $s_2 = s_5$, $s_3 = s_4$ and $c_1 = c_6$, $c_2 = c_5$ and $c_3 = c_4$;

The expressions for the matrices $\mathbf{M}_m^{\gamma_m}$ are obtained starting from the first $\mathbf{M}_1^p(0)$, in agreement with Eq.2.66:

$$\mathbf{M}_1^p(0) = \begin{bmatrix} \frac{iB_r}{c_1^p D_R} & 0 \\ 0 & \frac{iB_r}{c_1^p D_R} \end{bmatrix}. \tag{3.3}$$

The intermediate matrices are therefore derived from the ABCD matrices for propagation and transmissions. We present the formulas for the first two steps (propagation + transmission):

- $$\mathbf{M}_1^p(s_1) = \frac{\mathbf{D}_1^d \mathbf{M}_1^p(0) + \mathbf{C}_1^d}{\mathbf{B}_1^d \mathbf{M}_1^p(0) + \mathbf{A}_1^d} \tag{3.4}$$

  with the following definitions, accordingly to Eq.2.51 for propagation terms

  $$\mathbf{A}_1^d = \mathbf{D}_1^d = \begin{bmatrix} 1 & 0 \\ 0 & 1 \end{bmatrix}, \qquad \mathbf{B}_1^d = \begin{bmatrix} c_1^p s_1 & 0 \\ 0 & c_1^p s_1 \end{bmatrix}, \qquad \mathbf{C}_1^d = \mathbf{0}; \tag{3.5}$$

- $$\mathbf{M}_2^p(0) = \frac{\mathbf{D}_1^t \mathbf{M}_1^p(s_1) + \mathbf{C}_1^t}{\mathbf{B}_1^t \mathbf{M}_1^p(s_1) + \mathbf{A}_1^t} \tag{3.6}$$

  with the following definitions, accordingly to Eq.2.54

  $$\mathbf{A}_1^t = \begin{bmatrix} \frac{\cos\theta_2^p}{\cos\theta_1^p} & 0 \\ 0 & 1 \end{bmatrix}, \quad \mathbf{B}_1^t = \mathbf{0}, \quad \mathbf{C}_1^t = \mathbf{0}, \quad \mathbf{D}_1^t = \begin{bmatrix} \frac{\cos\theta_1^p}{\cos\theta_2^p} & 0 \\ 0 & 1 \end{bmatrix} \tag{3.7}$$

  The $\mathbf{C}_1^t$ matrix, along with the other $\mathbf{C}_m^t$ matrices is always null because the curvature terms h_{ij} are null, since the interfaces are all planar in the POI. This reduces a lot the complexity of the problem; moreover, there are not the terms related to the rotation about the x_3 axis, *i.e.* the λ matrices. Moreover, the angles θ appearing in all these expressions are 0 since the angle of incidence is always 0, *i.e.* the ray path is normal to the surface.

The other terms are substantially the same of these two just illustrated, with the obvious substitution of the velocity terms c_m^p and path s_m.

In Fig.3.2 the 2D magnitude profile of the velocity in the plane (y_1, y_3) of copper is shown, where the y_3 axis is in the direction of propagation, *i.e.* normal to the parallel interfaces, and the y_1 axis is in the perpendicular direction, as previously illustrated. This plane correspond to a *slice* of the ultrasonic beam, which has of course a 3D extension also in the y_2 plane. The dimensions of the problem are:

- $s_1 = 38\,\text{mm}$ is the Rexolite width of the wedge;
- $s_2 = 25\,\text{mm}$ is the water gap between the copper plane slab and the Rexolite wedge;
- $s_3 = 10\,\text{mm}$ is the dimension of the copper wall.

The different plots show how the field intensity decrease far away the central axis, represented by the $y_1 = 0$ coordinate. Depending on the chosen frequency, the field generated by the transducer change in shape and width. With the same piezoelectric disc diameter, the angle beam spread vary significally. For example, at the same distance $y_3 = 38\,\text{mm}$ the relative decay in amplitude for the 5 MHz transducer, *i.e.* the ratio between the actual amplitude and the one at the source face, at $y_1 = 5\,\text{mm}$ from the central axis is 0.2, while for the 2 MHz transducer is 0.7. This means the former piezoelectric disc generates a more narrow beam where the more energetic part is focused. Indeed, at same distance from the source, the magnitude is higher for the 5 MHz transducer. This is important parameter to watch since the more enery is transferred through the interface, the less attenuated will be the next reflections. Indeed, wave conversion at interface generates dispersione and attenuation.

The fact that the beam remains well collimated is shown also in Fig.3.3, where the section is in the (y_2, y_2) plane. Here the slice is made in the parallel plane at the interface, so the angular spread of the beam is observed. The field is computed at the transducer contact face when the beam has traveled through the media forth and back, so the total path is $\sum_{i=1}^{6} s_i$. The shown plane si therefor computed at the interface bewteen the probe and Rexolite. Again, the beam is broader for the 2 MHz case than for the 5 MHz. The lateral spread is important since this means less interference if more than one transducer are placed side by side.

3.2 CONCLUSIONS

The simulation for ultrasonic beams produced by piezoelectric transducer has been computed using the Multi-Gaussian beam model. In that approximation, the computation of the field is quite simple and superposition of different material layer is done with simplicity. Lateral and transversal view allow a fast comparison of the magnitude field at different frequency. The plots have shown the differences in the angular spread and relative intensity respect to the initial generated field at source. This simple but significative simulation help in the decision of the piezoelectric disc transducer

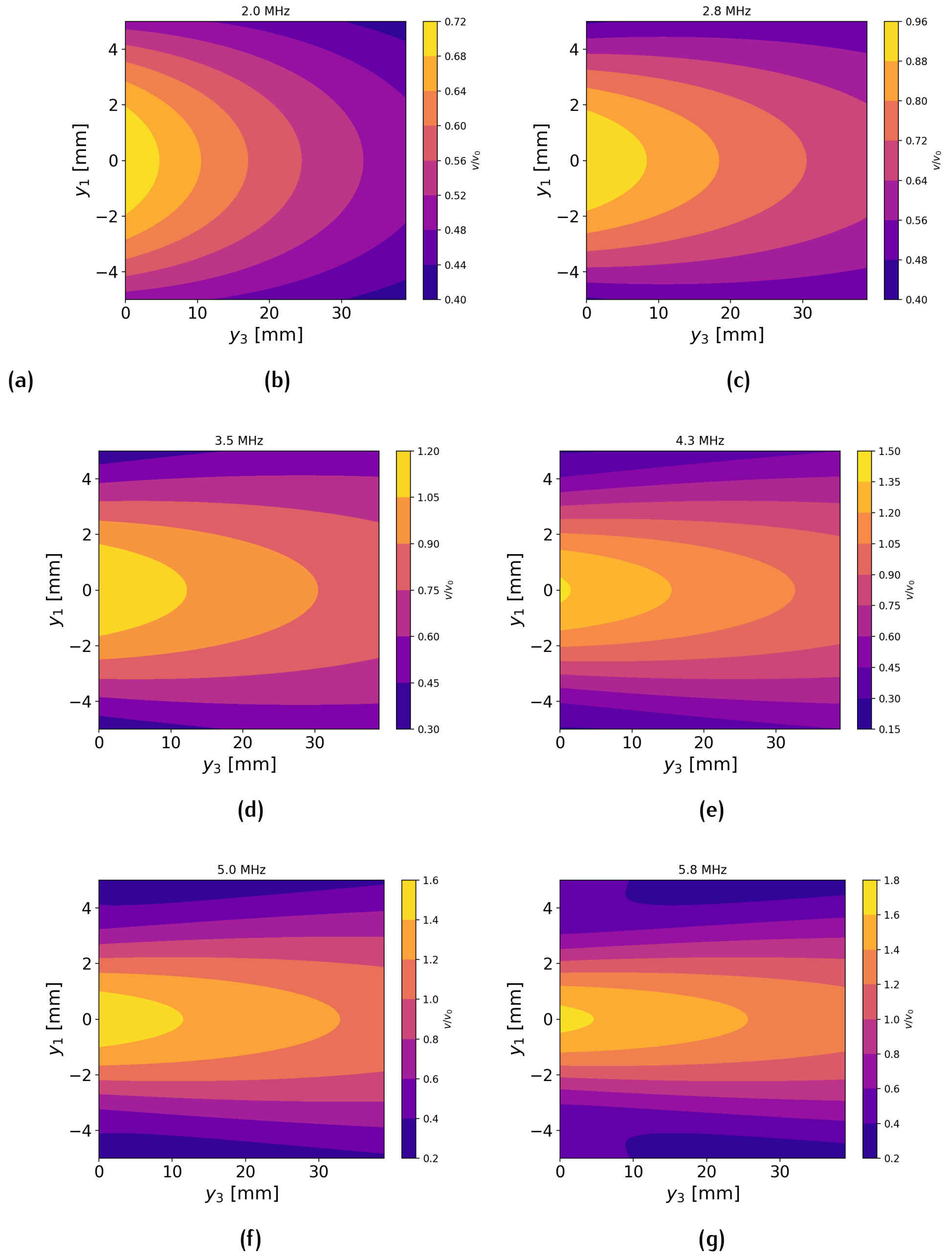

(a) **(b)** **(c)**

(d) **(e)**

(f) **(g)**

Figure 3.2: Velocity magnitude field in the (y_1, y_3) transducer plane. Simulation are reported for 2.0,2.8,3.5, 4.3, 5.0 and 5.8 MHz frequencies for $s_1 = 38\,\text{mm}$, $s_2 = 25\,\text{mm}$ $s_3 = 10\,\text{mm}$. The section shown is in the copper layer.

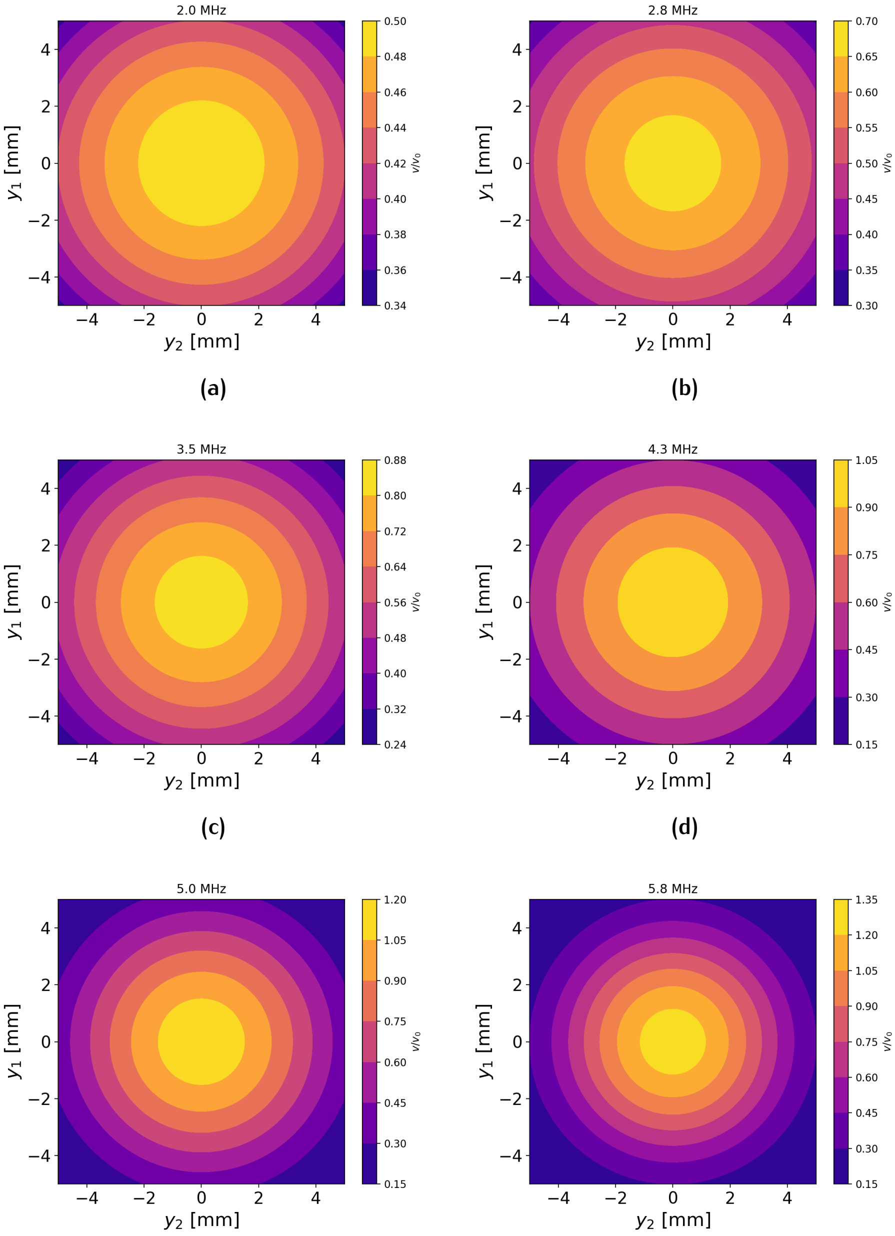

(a) (b) (c) (d) (e) (f)

Figure 3.3: Velocity field on the transducer surface, for test case with $s_1 = 38\,\text{mm}$, $s_2 = 25\,\text{mm}$ and $s_3 = 10\,\text{mm}$.

dimension and type, since the material of the disc changes depending on the chosen base frequency.

4 THE EXPERIMENTAL ULTRASONIC SYSTEM

4.1 OVERVIEW

This Chapter is devoted to the ultrasonic system setup. The first description regards the generic structure that every system must have. The description continues with the state of the art hardware, an easy-to-use commercial electronic board for generating ultrasonic signals, and used to perform non-destructive evaluation tests. In this way, a reference with this standard product allows the comparison with the proposed customized solution. Then, the ultrasonic setup used for the laboratory tests and for the first industrial prototype is described. Together with the hardware component, also the software for acquisition and signal elaboration with the experimental method and practical procedure is shown. Finally, it is described the methods and procedures that have allowed the realization of the calibration procedure that was one of the topic of the research activities.

4.2 GENERAL STRUCTURE OF UMS

The common ultrasonic system, shown in Fig.4.1 is made up of five principal components:

- Pulser/receiver;
- Cabling;
- Transducers;
- Oscilloscope;
- Inspected object;

This system involves the generation, propagation, and reception of short transient signals. In the electrical devices of the system, such as the pulser/receiver and cabling, these signals are electrical pulses. Once they arrive at the transducer, they are converted into mechanical oscillation by the piezoelectric element at the transducer face: acoustic/elastic waves start to propagate toward the inspected specimen in form of short time duration pulses in fluids or solids. In Fig. 4.1 (a) the specimen is immersed in water and the ultrasounds which enters the medium propagates until they encounter the other interface: the outgoing radiations are captured by a second transducer, acting like a receiver. When passing across multiple interface between different media, the ultrasounds reflects and part of the energy is lost. When the waves come to the receiver, the opposite piezoelectric effect take place: mechanical wave is now converted into electrical signal and travel through

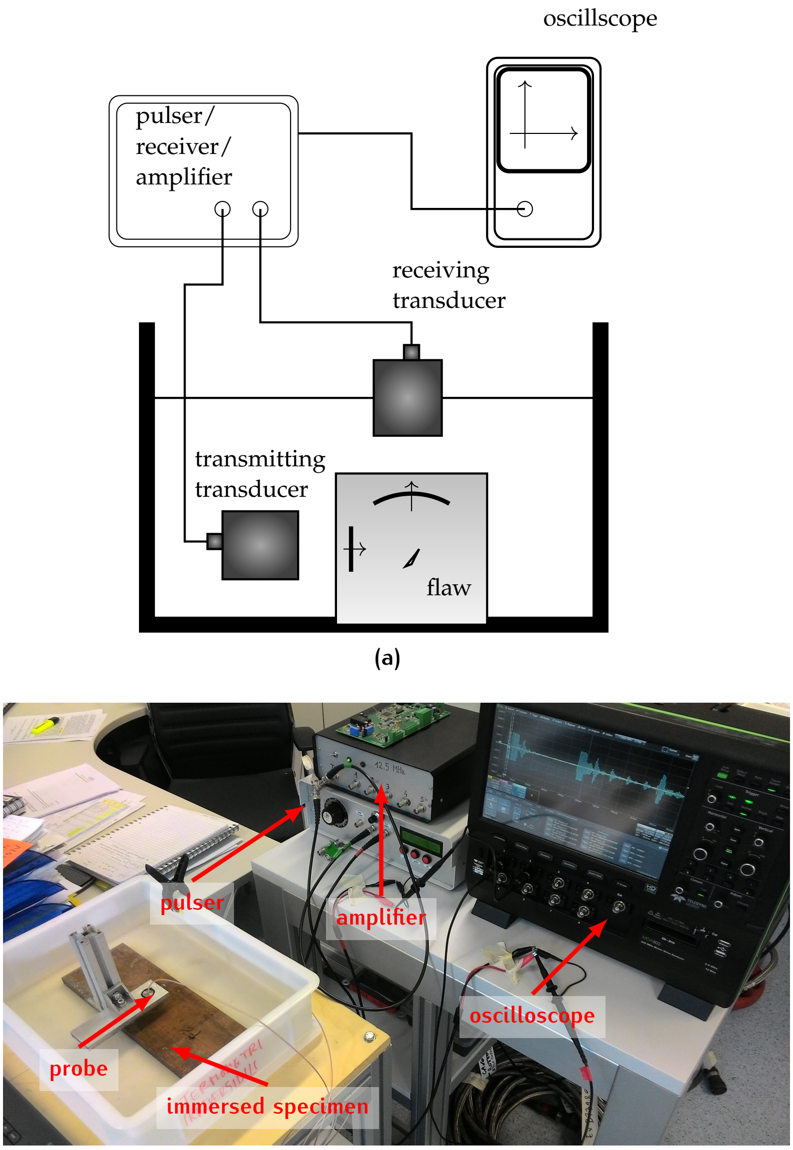

(a)

(b)

Figure 4.1: *(a)* Schematic depiction of an ultrasonic measurement system. *(b)* Ultrasonic measurement system in immersion configuration: only one transducer acting as both as transmitter and as receiver. The object specimen is surrounded by water and the probe is placed in vertical position, orthogonal to the planar surface.

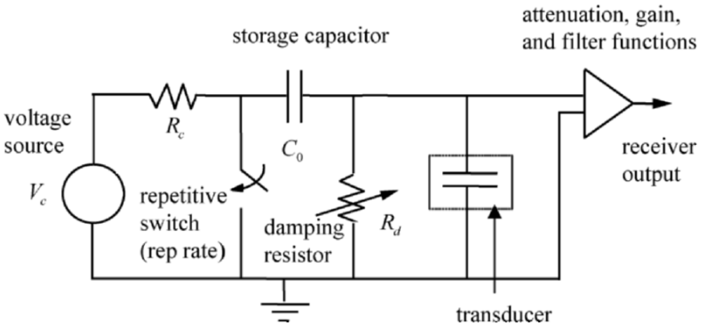

Figure 4.2: A simplified circuit representation of a pulser/receiver.

the cable from the receiving transducer to the receiver and the digital scope. However, and this is the case for our experiments, the same transducer can act as both receiver and transmitter. In Fig. 4.1 (b) is shown the setup used in the majority of the experimental test, and this is the pulse-echo configuration setup.

4.2.1 Pulser/Receiver

This is an electrical network that generates the electric signals which drives the transducers, *i.e.* the electromechanical components which transform the electric energy into acoustic one. In general, pulsers allow three type of control, which can be better described using Fig.4.2 as a reference.

One control is the energy setting, which basically controls the amount of energy stored in a capacitor, indicated in the same figure as C_0. This quantity is regulated by setting the voltage source: this varies the quantity of electric charge stored by the capacitor. The energy is periodically discharged into the transmitting transducer by closing the swicth of the electric circuit and this stimulates the piezoelectric component which oscillates for a short period at the frequency range of MHz. The repetition rate which sets the frequency of the sending pulses is the second type of control. Generally, this rate is set to ensure that the waves travelling in a component have had time to decay in amplitude to very small values before the next discharge occurs: in this way there is no overlapping of the received responses from one closing to the next which, if it occured, could cause triggering problems when the received signals are displayed in the oscilloscope screen. In fact, the oscilloscope is triggered by a signal generated in synchronization with the pulser discarges. Finally, the damping control on the pulser changes the value of a damping resistance R_d in the pulser receiver. Pulser's parameters are of fundamental importance for the final excitation pulse: the voltage amplitude and the pulse width are two most important. In each pulser there are primarily three settings, *i.e.* the pulse repetition rate, the pulse voltage amplitude (in volts), and the pulse width (in nanoseconds). The energy/ damping settings of the spike pulser and the voltage/pulse width settings of the square wave pulser control the amplitude and shape of the voltage and current at the output port of the pulser. Rectangular pulses are the standard for piezoelectric

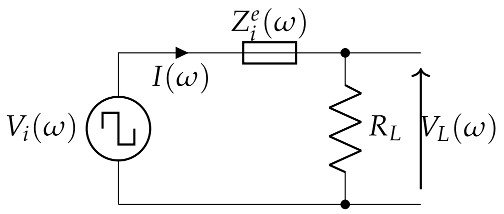

Figure 4.3: The Thévenin equivalent circuit for a pulser with attached a known load R_L, for measuring the impedance $Z_i^e(\omega)$.

component's excitation, and they must be synchronized with the natural frequency of the piezoelectric disc.

Last part of a pulser are the gain and amplitude controls. Generally amplifier components are embedded in the electric circuit of the pulser, soldered in the same board, but through transmission cables these two components can be connected and have both different hardware.

When designing ultrasonic system, both the electric than the mechanical (transducer, specimen inspected, couplant and so on) have to be matched in order to obtain the maximum transferred energy to the system. This could be done studying the *impedance matching* of all these components. From Thévenin theorem [24], we can determine those equivalent parameters which characterized the ultrasonic measurement system, using an equivalent electric circuit. The most important hypothesis is that we are working with a linear response device, *i.e.* a LTI (Linear-Time Invarian) system. Fig. 4.3 shows the equivalent circuit: measurements of $V_i(\omega)$ and $Z_i(\omega)$ are made for a specific system configuration, for example for a specific time width and voltage amplitude, realized with the same external electrical loading conditions. In this way, we have the complex impedance $Z_i^e(\omega)$ for a set of parameters. To find the latter we place a known load resistance, R_L at the output terminals of the pulser and measure the voltage $V_L(t)$ across this load, applying Fourier transform to this quantity gives $V_L(\omega)$. $V_i(\omega)$ is the equivalent Thévenin voltage source obtained by measuring the open-circuit voltage $V_0(t)$. From Fig.4.3 we see that

$$V_i - V_L = Z_i^e I \tag{4.1}$$

$$V_L = R_L I \tag{4.2}$$

and, eliminating the current I we have

$$Z_i^e = R_L \left(\frac{V_i(\omega)}{V_L(\omega)} - 1 \right). \tag{4.3}$$

Since these values depend on the instrument settings of the pulser they can be determined for several configurations.

Usually, the R_L external load is a 50 Ω resistor.

4.2.2 Cabling

The cabling system transfer electric signal to the transducers from the pulser and viceversa. However, these signals are not left unchanged, since cabling influence the signal shape. At MHz frequencies the electric cables slightly influence the outcoming signal and these can modify the final wavelet shape. Cables are coaxial conductors which transfer electromagnetic field form one ends to another. In particular, they are a two-conductor transmission lines, like the one in Fig. 4.4 (a). Since they are particular waveguide in the context of transmission lines, the following relation is valid:

$$\oint_{S_1} \left[\mathbf{E}_1^{(2)} \times \mathbf{H}_1^{(1)} - \mathbf{E}_1^{(1)} \times \mathbf{H}_1^{(2)} \right] \cdot \mathbf{n}_1 \, dS = \oint_{S_2} \left[\mathbf{E}_2^{(2)} \times \mathbf{H}_2^{(1)} - \mathbf{E}_2^{(1)} \times \mathbf{H}_2^{(2)} \right] \cdot \mathbf{n}_2 \, dS, \quad (4.4)$$

which is called *reciprocity theorem*. $(\mathbf{E}_1, \mathbf{H}_1)$ are the electric and magnetic field at the end of the cable acting over an area S_1, whose unit normal vector is $\mathbf{n}_1$, and the same for S_2. In a coaxial waveguide like these cables, it can be demonstrated [17] that exist a fundamental wave mode called *TEM* mode, *i.e.* transverse electromagnetic mode, where the field behave like in Fig.4.4 (a). The superscript (1) and (2) designate the fields when the cable is under two different driving or termination conditions, representing two different states. For such a propagating mode, the reciprocity relation Eq.4.4 reduces to a similar relationship involving current and voltages:

$$V_1^{(1)} I_1^{(2)} - V_1^{(2)} I_1^{(1)} = V_2^{(1)} I_2^{(2)} - V_2^{(2)} I_2^{(1)} \quad (4.5)$$

The situation is described in Fig.4.4 (b): the current I_1 is flowing into the cable at the left side, and the current I_2 is flowing out at the other end.Thus the voltage and current a one end port are linearly related to the voltage and current at the other end and the it is possible to model this as the two-port system

$$\begin{bmatrix} V_1 \\ I_1 \end{bmatrix} = \begin{bmatrix} T_{11} & T_{12} \\ T_{21} & T_{22} \end{bmatrix} \begin{bmatrix} V_2 \\ I_2 \end{bmatrix} \quad (4.6)$$

and det $[\mathbf{T}] = T_{11}T_{22} - T_{12}T_{21} = 1$.

To detect the *transfer matrix* **T** parameters (also known ABCD matrix), it can be used a network analyzer, an instrument in which the cables are attached at one port and the other at a second one. This is useful because in practice we have a cascade connection of more cables, or two-port networks. In this case network analyzer implement frequency sweeps to evaluate the parameters for the device attached on it. The T parameters of a two-port system consisting of a series of impedance Z between ports 1 and 2 are derived following [17]:

$$T_{11} = \frac{V_1}{V_2}|_{I_2=0} \quad (4.7)$$

$$T_{12} = \frac{V_1}{I_2}|_{V_2=0} = \frac{V_1}{V_1/Z} = Z \quad (4.8)$$

$$T_{21} = \frac{I_1}{V_2}|_{I_2=0} = 0 \quad (4.9)$$

$$T_{22} = \frac{I_1}{I_2}|_{V_2=0} = \frac{I_1}{I_1} = 1 \quad (4.10)$$

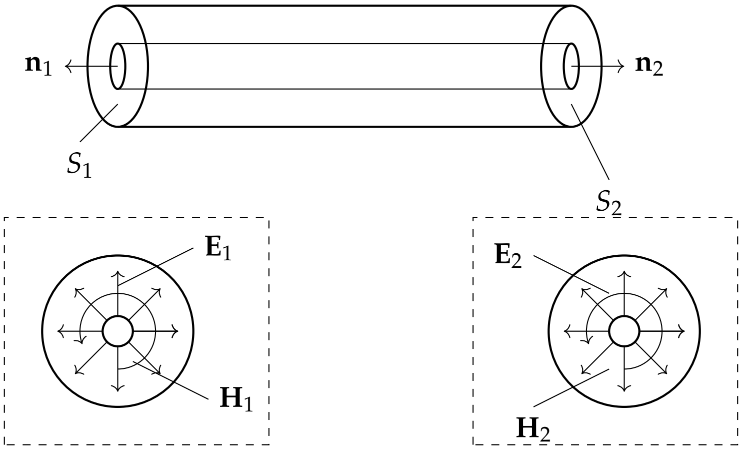

(a) Electric and magnetic field in TEM mode of a coaxial cable: $E_\phi = 0$ and $H_r = 0$ at r equal the internal and external conductor.

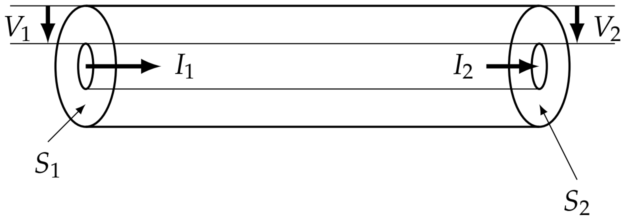

(b) A cable modeled in terms of the voltages and currents at the two end ports.

Figure 4.4

4.2.3 Ultrasonic Transducers

Ultrasonic transducer are the terminal part of the ultrasonic measurement system. These devices convert the electric energy into a mechanical one, *i.e.* acoustic energy in form of transient waves, through the so called *piezo-electric effect*. When an electric potential difference is applied to the end of such an element, it is converted into an elastic deformation and it start the oscillations. These piezoelectric materials can convert electric stimulus into mechanical vibrations having different modes. For an exhaustive and detailed description of the methods of construction, tests with different materials and working conditions, refer to [11]. In Fig.4.5 the schematic section of a transducer is shown.

A typical ultrasonic transducer is made of a very thin layer of piezoelectric crystal is plated on the contact face with a wear plate, a covering material. The latter has the role of protecting the front face of the crystal, because due to its thickness (about 100 µm) it is very fragile. On the back face of the crystal there's a layer of epoxy resin, which acts like an highly attenuating medium that causes the deformation of the shape and change in duration of the output pulse. The damping is a critical parameter to control and this backing layer covers a primary role. It has been observed that the higher the damping, obtained with more loaded particle in the resin, the more narrow will be the wavelet signal. To achive this, usually these metallic particles are of tungsten, which modify the sound-absorbing properties of the overall layer. In Fig.4.6(a) is shown the internal connection with the coaxial cables:

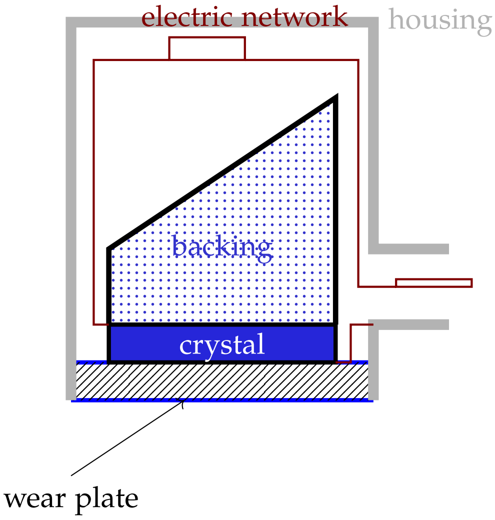

Figure 4.5: Schematic depiction of transducer internal structure. The crystal is the piezoelectric element which vibrates at a given frequency when electrically or mechanically stimulated. backing performs the role of damping the mechanical vibration, depending on the material it is made of. The wear plate

like already shown in the schematic representation, the two electrodes are connected to the internal junctions. The negative poles is connected to the external case, *i.e.* the ground, while the positive electrode is joined to the back side of the crystal, and it is responsible of the excitation mode. A datailed view is visible in the same Fig.4.6 (b), where the two terminal electrode are visible. One of the two is connected to the PZT crystal on the front face, visualized in (c). The piezoelectric material is a thin layer of a ceramic perovskite material, usually a PZT (Laed-Zirconate-Titanate) compound, but also barium titanate, lead metaniobate (LM) and piezo-composite materials. Here the crystal is not protected by the wear plate. The last figure (d) shows instead the same ultrasonic transducer fixed at the wedge material in Rexolite, as the one used for the experimental tests.

Material used in the construction of the piezoelectric ceramic can be grouped in two categories:

- soft materials: high mobility of the ceramic domains, so the polarization easily occur. They are used low power for ultrasonic generation, with frequencies starting from hundreds of kHz to tens of MHz. They are highly recommended for ultrasonic transducer where it is necessary sensibility of micron or nanometer, with electro-acoustic applications;
- hard materials: low mobility of the ceramic domains, requiring high polarization fields. Suitable for working in resonance for long periods of time, they are employed for high power ultrasonic generation, with frequencies of about kHz. For example, they are used for plastic welding, also known high-frequency welding.

For our purpose, the overall ceramic plates are of soft type, ideal to produce and receive a large frequency bandwidth. These ceramic disks have

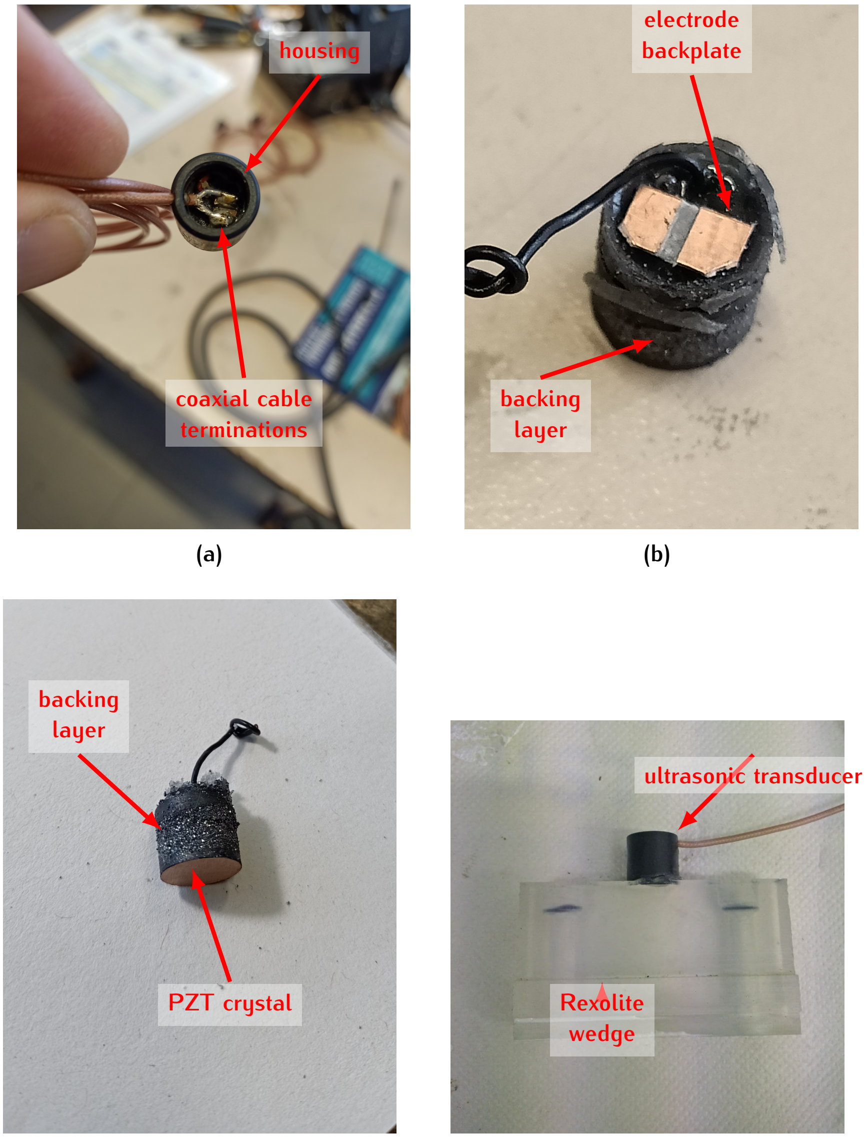

(a) (b)

(c) (d)

Figure 4.6: (a)The coaxial cable terminal connections on the transducer's backing - upper view. (b) Metal backplates for electrode connections where the coaxial termination are soldered. (c) Lateral side of an uncovered transducer which the PZT crystal. (d) Search unit composed by the ultrasonic transducer plus the Rexolite wedge material, for a straight beam transducer.

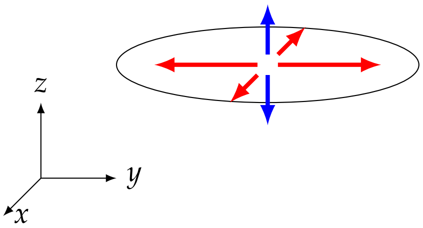

Figure 4.7: Fundamental vibrational modes for PZT crystal of an ultrasonic transducer.*Red*: radial mode (in plane (x, y)); *blue*: axial mode (z axis).

two independent and fundamental modes of vibration: an axial mode, corresponding at a *piston mode* oscillation, along the normal axis z of the transducer's face; and a radial mode, corresponding at dilation and contraction of the face, Fig.4.7.

4.2.3.1 *Wedge material*

The choice of this substrate has to be thoughtful, since in order to allow an efficient propagation and transmission, each materials has different mechanical properties. Usually, polymeric material with acoustic impedance comparable to water are effective for these tasks. PMMA (Polymethil Methacrylate), also known with commercial name of Plexiglas, is a transparent thermoplastic used as an alternative to glass. Moreover, PMMA is commonly used as delay line for its acoustic impedance similar to water, so the transferred energy to water is maximum. Moreover, PMMA has a glass transition temperature T_g of about 105°C , which made it the suitable choice to be coupled with water. The other tested material which has similar mechanical properties to PMMS is the cross-linked polystyrene, with commercial name Rexolite. Its acoustic impedance is quite similar to water and suitable for the role of a wedge material in this application.

4.2.3.2 *Matching layer*

The purpose of the matching layer is to match the acoustic impedance of the crystal with the acoustic impedance of the load (water, wedge, test object, etc.). It provides conditions for the acoustic energy to be transmitted from the crystal to the load with the least possible loss of energy. If the acoustic impedance of the crystal and the load are exactly equal, all ultrasonic energy generated by the crystal will be transmitted at the interface. Three types of matching layers are commonly used depending on the transducer application: matching layer for water (immersion inspection), matching layer for wedge material, and wear plate for straight beam contact probe for the inspection of metals. In the previous Fig.4.6 (d) the transducer is attached to the wedge by the second type of the matching layer previously described. However, since the search unit works in an immersed setup, the wedge has not a matching layer for the contact condition and the Rexolite interface is directly immersed in water.

Figure 4.8: Teledyne LeCroy MDA803 digital scope, 8 channel, sampling rate 2.5 GS/s.

4.2.4 Oscilloscope

The last important element in an ultrasonic system is the oscilloscope.It is a necessary instrument to sampling the electric signals to and from the transducers. In Fig.4.8 there's shown the laboratory oscilloscope, representing a commercial product which can be considered a state of the art device. With this instrument is possible to detect and acquire the sampled electric signal. The trigger is usually set on the raising edge of the rectangular pulse used for generate the ultrasonic pulse. This instrument allows to acquire digital signal with high resolution; furthermore, its versatility and possibilities permit to use with ease and to explore many configuration and channels at contemporary. This oscilloscope represents the state of the art in terms of instrument precision and performance, but it is not feasible to use such a device for an industrial, custom solution for real time process control, and this for several reasons. The first reason is that this is a laboratory instrument, which a very high sensibility, many and optional functions which are not indispensable for the final application. The second reason is the obvious difficulty of including such an instrument in a custom device, since the greatest problem will be its size. Another reason is the harsh environment conditions because they influence the durability and reliability of the outcomes. The steelplant is not the standard environment for a laboratory device: this is certainly the most critical aspect.

4.3 STATE OF THE ART WITH EUROSONIC-MISTRAS

To perform comparisons with the most accurate and precise measurements affordable with a commercial device, it has been used the EUROSONIC-Mistras UTC110 ultrasonic module. The same cabling and transducer architecture has been used with this ultrasonic board, in order to evaluate the influence of the generation system. The device, shown in Fig.4.9, is compact and with few input and output ports: a USB for power supply and data transfer, two ports for probe connection and other 2 ports to allow series connection with other same modules. The only use mode has been the pulse echo mode, already seen.

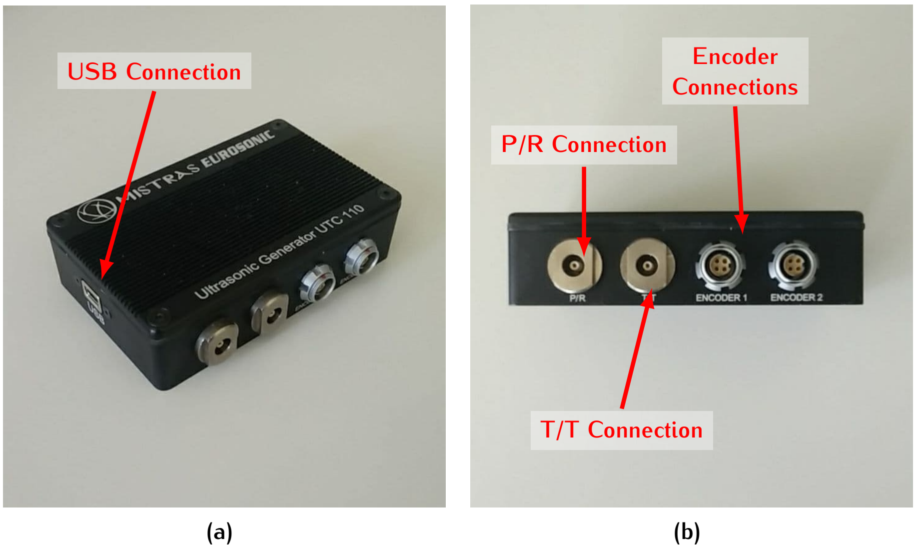

Figure 4.9: Ultrasonic module UTC110 by Eurosonic-MISTRAS. (a) Lateral view of the electronic board. USB connection allows power supply and data transfer. (b) Port connections. P/R is Pulser/Receiver mode connection. It works in the Pulse/Echo model with the same probe - Reflection mode selected by the software. T/T is Through Transmission mode connection. One probe is used as a transmitter and another one as a receiver - previously mode selection by the software.

Specification of the used ultrasonic module UTC110 can be found in their website [12] and in Tab.4.10.

4.3.1 Software for managing and visualization

A graphical user interface has been realized to setting parameters and to visualize the signals, in Python using the Qt framework. For the software part managing drivers and acquisition, the SDK allowed to write C++ code containing the essential routines for the operation and control of the basic functions.

In Fig. 4.11 there is a screenshot of the graphic interface: there are the boxes used for setting the card parameters and in the black window the signals in real-time are displayed. The customized interface allow to set and modify in real time the following parameters:

1. Time width for the pulse function;
2. Amplitude for the pulse function;
3. Repetition rate;
4. Gain;
5. Time-window boundaries for signal visualization;

Regarding the temperature measurements they have been performed with a digital thermometer with 4 channels. The temperature acquisition has been

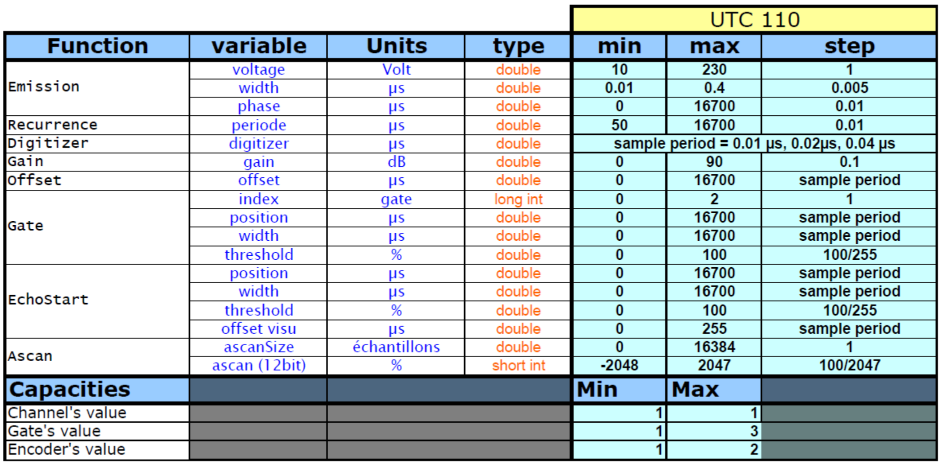

				UTC 110		
Function	**variable**	**Units**	**type**	**min**	**max**	**step**
Emission	voltage	Volt	double	10	230	1
	width	µs	double	0.01	0.4	0.005
	phase	µs	double	0	16700	0.01
Recurrence	periode	µs	double	50	16700	0.01
Digitizer	digitizer	µs	double	sample period = 0.01 µs, 0.02µs, 0.04 µs		
Gain	gain	dB	double	0	90	0.1
Offset	offset	µs	double	0	16700	sample period
Gate	index	gate	long int	0	2	1
	position	µs	double	0	16700	sample period
	width	µs	double	0	16700	sample period
	threshold	%	double	0	100	100/255
EchoStart	position	µs	double	0	16700	sample period
	width	µs	double	0	16700	sample period
	threshold	%	double	0	100	100/255
	offset visu	µs	double	0	255	sample period
Ascan	ascanSize	échantillons	double	0	16384	1
	ascan (12bit)	%	short int	-2048	2047	100/2047
Capacities				**Min**	**Max**	
Channel's value				1	1	
Gate's value				1	3	
Encoder's value				1	2	

Figure 4.10: Ultrasonic module UTC110 specification (source [13]).

integrated in the GUI software; in this way, a real-time trend is visible on the screen of the PC used for controlling the card and setting the parameters. In Fig.4.12 is depicted the experimental apparatus with the UTC110 card, without the inspected object, with the digital thermometer also connected to the PC. The overall software diagram is shown in Fig. 4.13. The software allows a command line interface to save single dump or continuous signals, along with a txt files with parameters.

The user interface has been designed in order to give some useful information during the measurement processes, and to help the user. An useful tool is the real time evaluation of the temperature, from the 4 channels. In Fig. 4.14 (b) there are the 4 temperature acquired at each instant. When acquisition is started, and signals are acquired, temperature are also registered in a header of the file. Real time visualization allow to control temperature and choose the right time at which starting acquisition, when the temperature is, for example, constant over a short period of time. In this sense it has been implemented the real time histogram for the time of flight measurement, *i.e.* the dispersion histogram of the last tens of acquired points. To evaluate signal shape and verify how it degrades with temperature it has been decided to perform real time evaluation of the FFT of a portioned part of the signal. Indeed, since attenuation is observed when temperature increment occur, FFT revealed additional information about frequencies contribution in the wavelet distortion. For example, increasing attenuation involves increasing of higher frequency components with the effect of changing the shape: this introduce more noise, disturbing the measure and getting worst results.

4.4 CUSTOMIZED ULTRASONIC SETUP

In this section the customization of the ultrasonic setup is described. It makes the prototype of the real working sensor in production. Despite the presence of high-performance scope and commercial ultrasonic system, the needs of made a dedicated version has been already discussed. For practical applications, there are many DSP (Digital Signal Processor), suitable for

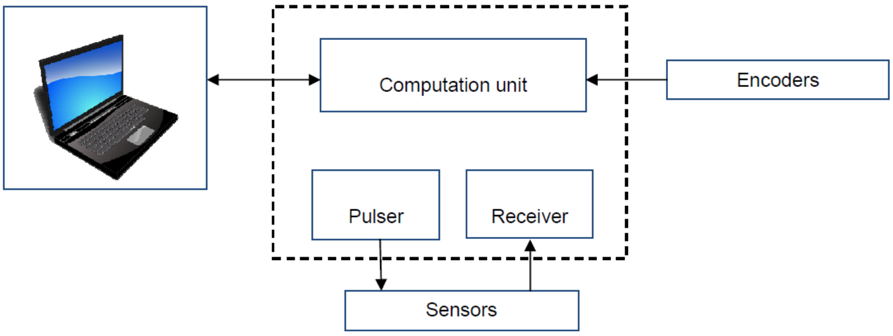

(a)

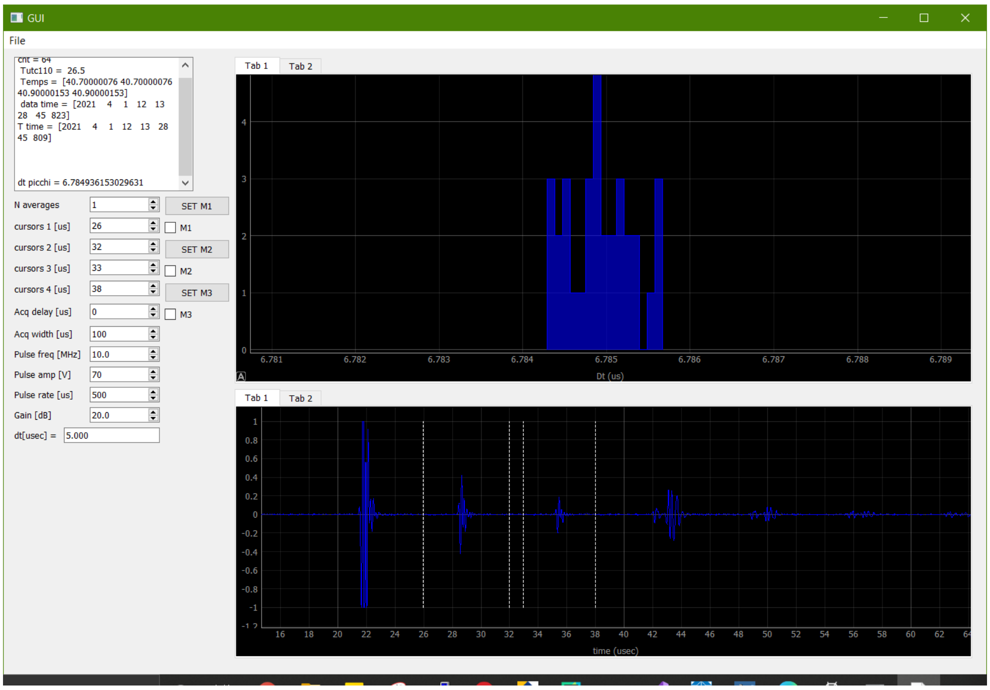

```
cnt = 64
 Tutc110 =  26.5
 Temps =  [40.70000076 40.70000076
40.90000153 40.90000153]
 data time =  [2021    4    1   12   13
28   45  823]
T time =  [2021    4    1   12   13   28
45  809]



dt picchi = 6.784936153029631
```

N averages 1 SET M1

cursors 1 [us] 26 ☐ M1

cursors 2 [us] 32 SET M2

cursors 3 [us] 33 ☐ M2

cursors 4 [us] 38 SET M3

Acq delay [us] 0 ☐ M3

Acq width [us] 100

Pulse freq [MHz] 10.0

Pulse amp [V] 70

Pulse rate [us] 500

Gain [dB] 20.0

dt[usec] = 5.000

(b)

Figure 4.11: (b) Graphical User-Interface (GUI) for the command setting of the Eurosonic-MISTRAS board and real time visualization. One left: Text label for temperature measuerement and timestamp. On the sliding box teh

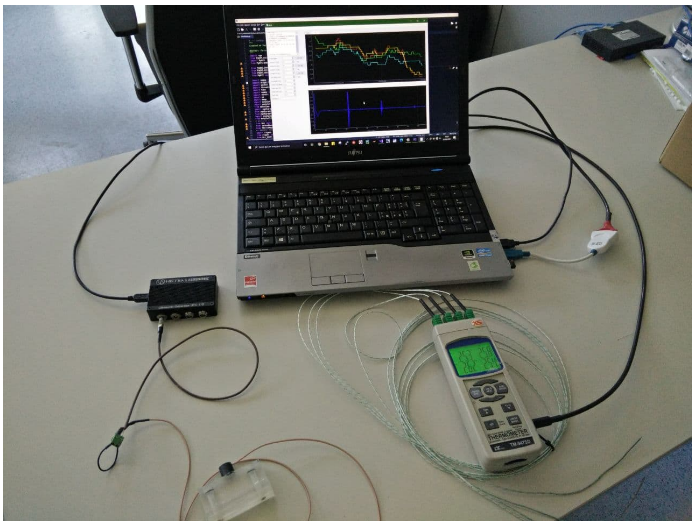

(a)

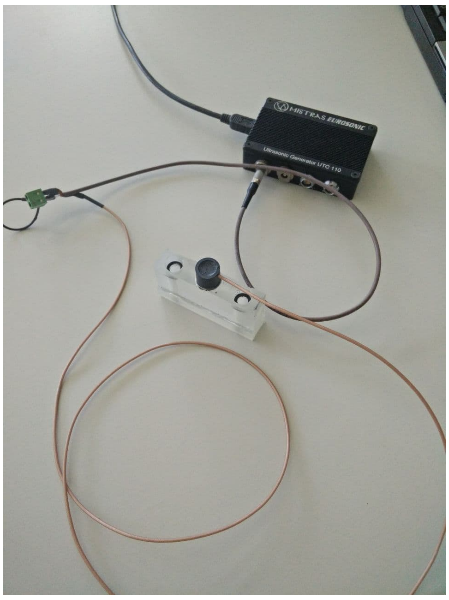

(b)

Figure 4.12: Ultrasonic acquisition system. *Left*: UTC card with connections to PC and Ultrasonic transducer. The GUI is visible on the PC's screen; *Right*: Detailed view on the UTC car with LEMO connector for the transducer.

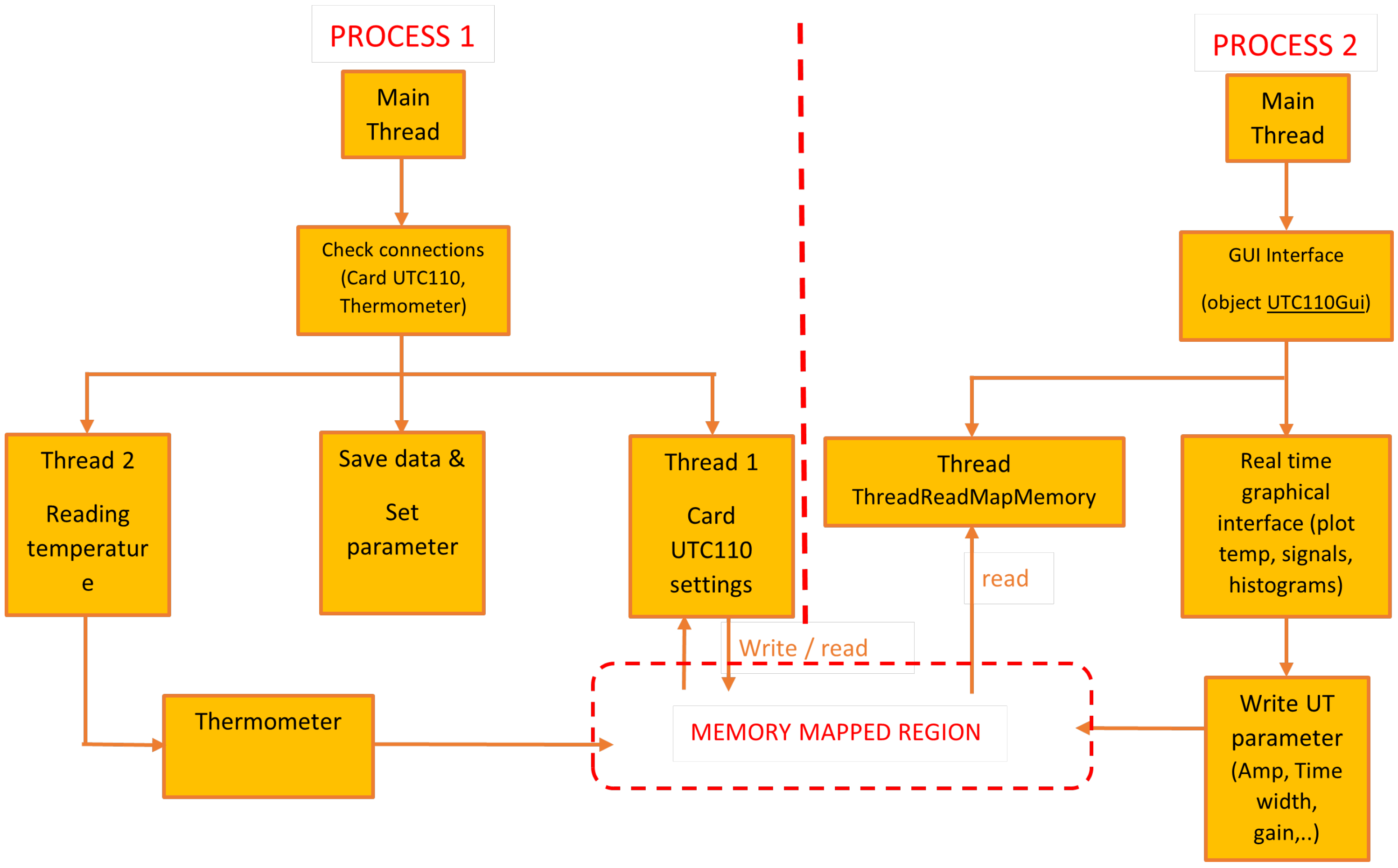

(a)

Figure 4.13: Flowchart of processes execution: independent tasks communicate each other through a memory mapped region.

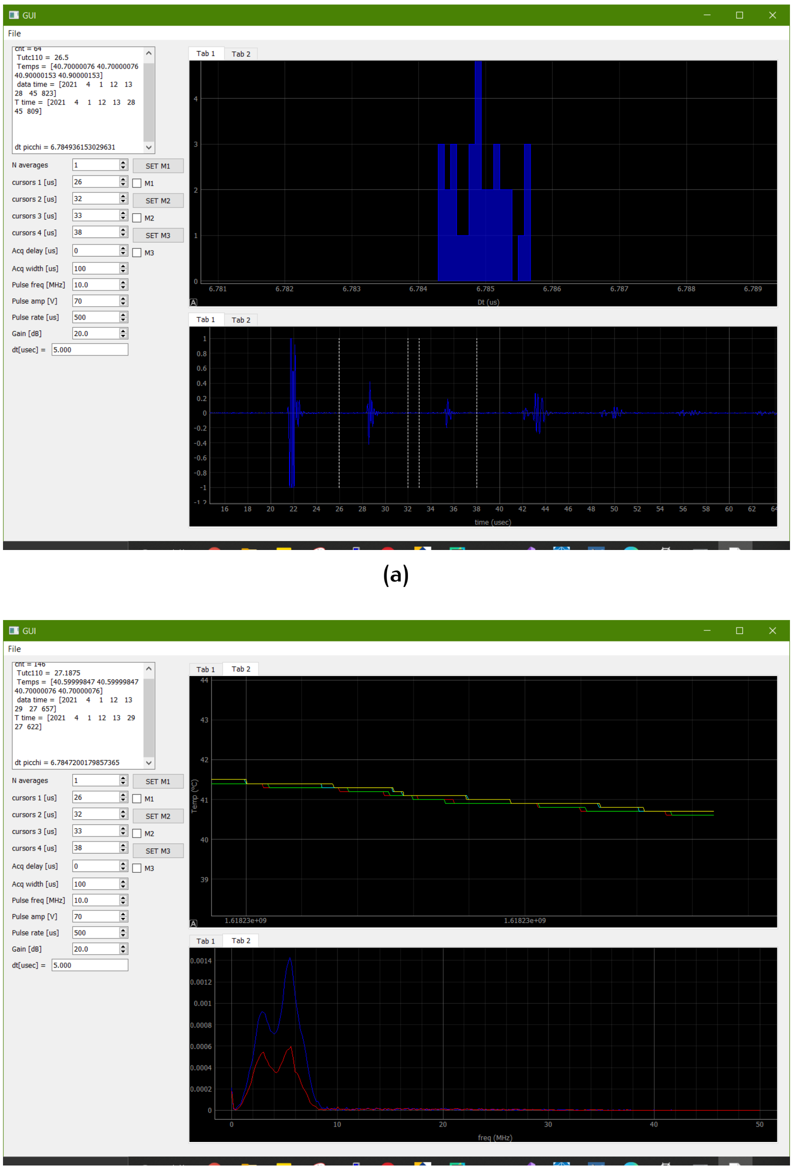

(a)

```
cnt = 64
 Tutc110 =  26.5
 Temps =  [40.70000076 40.70000076
40.90000153 40.90000153]
 data time =  [2021    4    1   12   13
28   45  823]
T time =  [2021    4    1   12   13   28
45  809]


dt picchi = 6.784936153029631
```

N averages 1

cursors 1 [us] 26 ☐ M1

cursors 2 [us] 32

cursors 3 [us] 33 ☐ M2

cursors 4 [us] 38

Acq delay [us] 0 ☐ M3

Acq width [us] 100

Pulse freq [MHz] 10.0

Pulse amp [V] 70

Pulse rate [us] 500

Gain [dB] 20.0

dt[usec] = 5.000

(b)

```
cnt = 146
 Tutc110 =  27.1875
 Temps =  [40.59999847 40.59999847
40.70000076 40.70000076]
 data time =  [2021    4    1   12   13
29   27  657]
T time =  [2021    4    1   12   13   29
27  622]


dt picchi = 6.7847200179857365
```

N averages 1

cursors 1 [us] 26 ☐ M1

cursors 2 [us] 32

cursors 3 [us] 33 ☐ M2

cursors 4 [us] 38

Acq delay [us] 0 ☐ M3

Acq width [us] 100

Pulse freq [MHz] 10.0

Pulse amp [V] 70

Pulse rate [us] 500

Gain [dB] 20.0

dt[usec] = 5.000

Figure 4.14: Graphical User Interface for UTC110. *(a)*: real time Δt distribution between first ($R1$) and second ($R2$) in copper (*above*); entire signal (*below*). *(b)*: temperature trends for 4 channels (*above*); FFT windowed signals (*below*).

this kind of implementations, that can be used integrated with the overall system of transducer and other components. The choice was to completely customize the electronic hardware design; for this reason, many time was spent to design the electrical part of the ultrasonic system. Moreover, an important consideration has been made around the working environment of the sensor, where the experience and know-how of the company have represented an important contribution on the realization. Limits depending on the available electronic hardware have been considered also in the design of the algorithmic part of the project. In these cases, some tricks have been deployed, considering both hardware cost and performance. The electronic devices have been developed and tested in laboratory, making comparisons with the state of the art measurement. In Fig. 4.15 is the first experimental setup developed for the first measurements. The graphical interface was quite similar to the one encountered for the Eurosonic, since the aim is always the same.

4.4.1 Characterization of Ultrasonic transducers

One of the main characteristics we decided to investigate was the temporal width of the generated wavelet in the ultrasonic generation process. The acoustic oscillations stimulated by the electrical signal have a finite temporal resolution before decaying; depending on the damping factor. Due to the mechanical properties of backing and matching layers, different shape signal could be obtained. In Tab.4.1 are reported the material properties for the most common piezo-crystal materials. These values all influence the final ultrasonic beam shape, the values of the minimum and maximum amplitude, the beam angle and others. Also, different piezoelectric ceramic diameter influences the output shape of signals: with equal nominal frequency crystal, the beam extension can vary depending on the diameter size. Indeed, with a more narrow diameter, the radiation acoustic lobe is larger, reducing the energy density through the specimen. With the aid of the simulation through the Gaussian beam model, several configuration have been tested in laboratory.

Several test confirmed that the a 10 mm diameter and 5 MHz probe to be used in an immersion, normal incidence setup. Generation, propagation and reception processes in a common NDE setup usually take some microseconds or at most few tens of microseconds. This is principally due to the high material velocities, and the small dimensions of the setup under study. Moreover, a common ultrasonic pulser generates electrical stimuli every hundred of milliseconds: in this interval we expect to have the overall physical propagation plus the electronic elaboration to visualize signals and do some sort of elaboration. The main properties which influences the final output shape are the type of the piezoelectric crystal and its thickness. The greater the thickness, the slower will be its oscillatory motion, as expected.

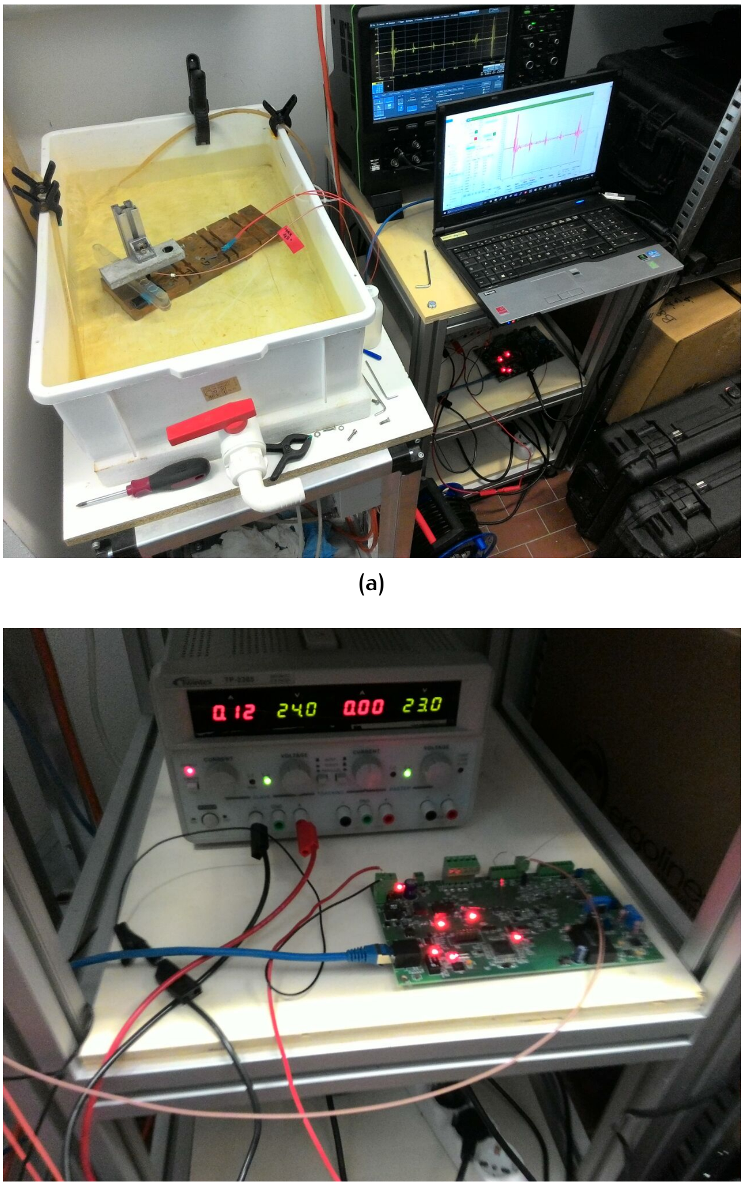

(a)

(b)

Figure 4.15: Details of experimental setup for temperature variation test with custom electronic. (a) Laboratory test with immersion setup in pulse-echo configuration. Laptop, cabling, probe, K-thermocouple, digital scoper and power unit supply are the components of the setup. (b) The electronic board with the integrate circuits and the power unit supply.

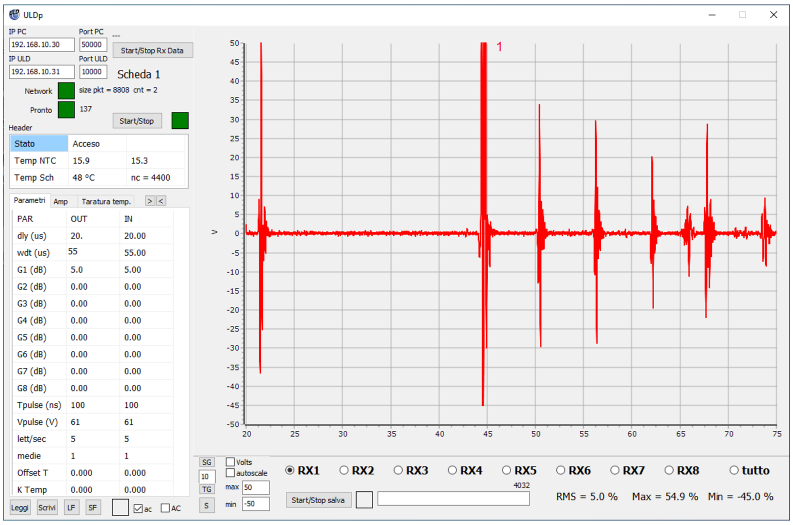

IP PC 192.168.10.30
Port PC 50000
IP ULD 192.168.10.31
Port ULD 10000
Scheda 1
size pkt = 8808 cnt = 2
Pronto 137

Stato	Acceso	
Temp NTC	15.9	15.3
Temp Sch	48 °C	nc = 4400

PAR	OUT	IN
dly (us)	20.	20.00
wdt (us)	55	55.00
G1 (dB)	5.0	5.00
G2 (dB)	0.00	0.00
G3 (dB)	0.00	0.00
G4 (dB)	0.00	0.00
G5 (dB)	0.00	0.00
G6 (dB)	0.00	0.00
G7 (dB)	0.00	0.00
G8 (dB)	0.00	0.00
Tpulse (ns)	100	100
Vpulse (V)	61	61
lett/sec	5	5
medie	1	1
Offset T	0.000	0.000
K Temp	0.000	0.000

☑ ac ☐ AC
10
☐ Volts
☐ autoscale
max 50
min -50
● RX1 ○ RX2 ○ RX3 ○ RX4 ○ RX5 ○ RX6 ○ RX7 ○ RX8 ○ tutto
4032
RMS = 5.0 % Max = 54.9 % Min = -45.0 %

Figure 4.16: Screenshot of the software tool for signal visualization and acquisition. Also in this interface the parameters are settable, then this electronic board guarantee a multichannel device:

Physical property	Unit of measure	Crystal material	
		Lead Zirconate Titanate (PZT)	Piezo-composite
Acoustic impedance	Mray	30-39	8-12
Coupling electromagnetic coefficient, k_T		0.40-0.53	0.5-0.7
Coupling coefficient for radial vibration mode, k_p		0.58	<0.1
Dielectric constant, κ		250-2000	200-600
Density	g/cm^3	7.8	3.5-4

Table 4.1: Characteristic of some piezoelectric materials, data reported from [7].

Backing material	Density	Speed of sound
	ρ_b [kg/m^3]	c_b [m s^{-1}]
Zeonex E48R	1010	2593
Zeonex 790R	1010	2489
Epotek 353ND	1240	2578

Table 4.2: Parameters of some selected backing materials.

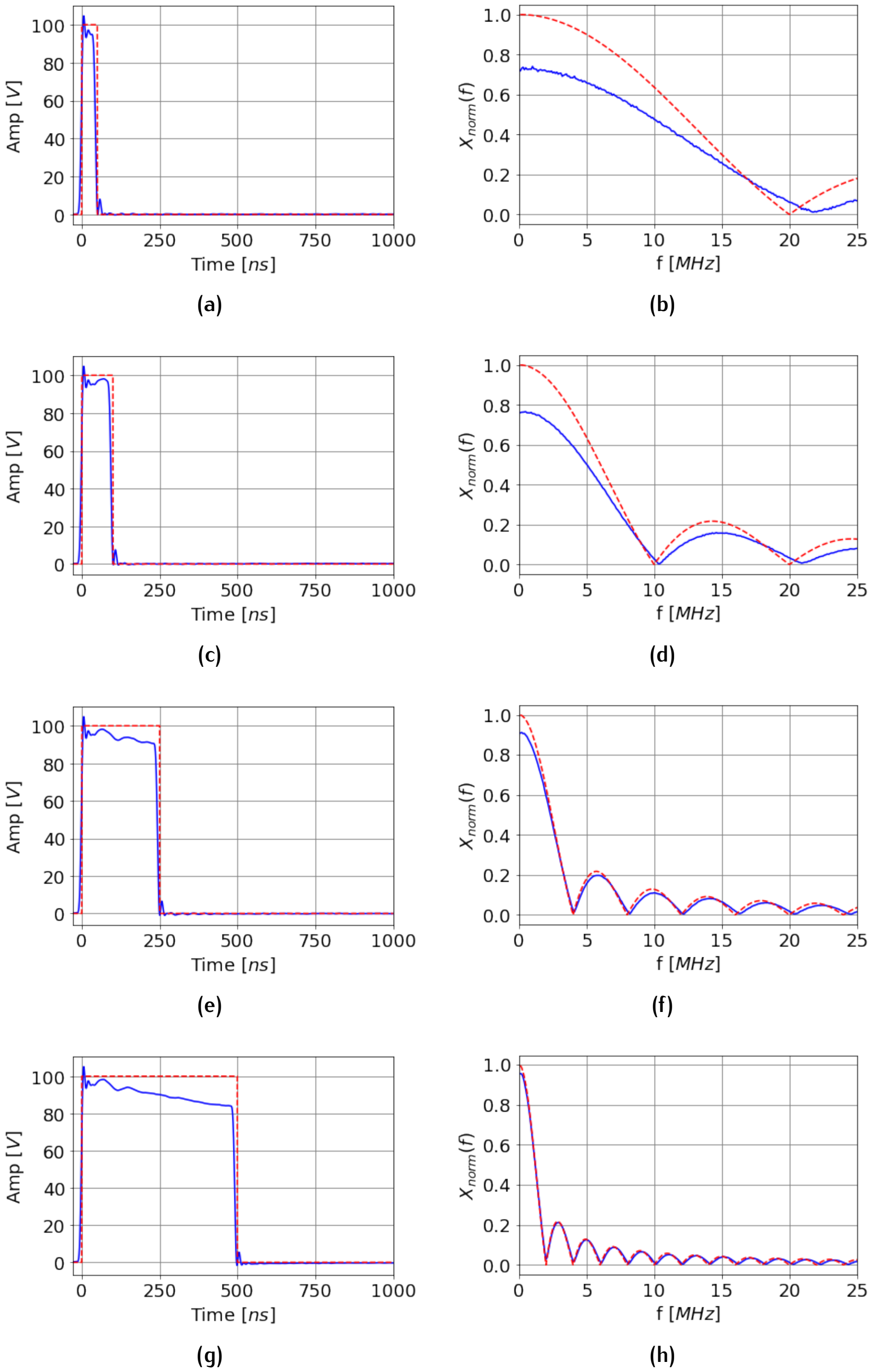

(a) (b) (c) (d) (e) (f) (g) (h)

Figure 4.17: *Left plots*: output rectangular pulses with no probe (open-circuit) attached (*blue*) and ideal rectangular pulse (*red dashed*). *Right plots*: normalized magnitude spectrum of corresponding measured (*blue*) and ideal (*red*) pulses.(a)-(b) 50 ns;(c)-(d) 100 ns; (e)-(f) 250 ns; (g)-(h) 500 ns.

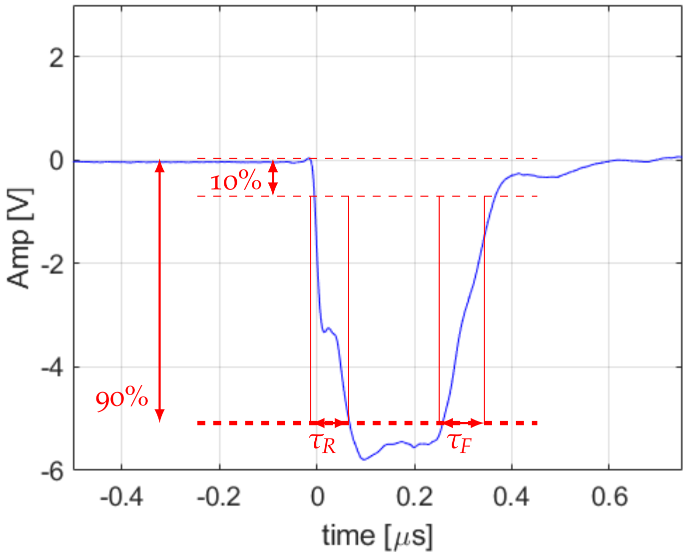

(a)

Figure 4.18: Measured rectangular pulse at the pulser termination, with load. The parameters are the following: τ_R is the *rise time* , *i.e* the time for a signal to change from a minimum value to its maximum value, generally the 10% and the 90% of the signal amplitude; τ_F is *fall time*, which is the reverse of the previous definition.

4.4.2 Impulse function

To produce the most energetic signal by the ultrasonic probe, it's quite important to study of the correct impulse stimulation. The first thing is to determine how the latter influences the final shape of the wavelet. Generally, the most common impulse function is in form of rectangular pulse, like those in Fig.4.17 (a)-(c)-(e) where are shown different measured pulse width (in *blue*) along with the ideal form of the pulse. In the right figures are depicted the normalized spectrum of these pulses and the *sinc* function, because it is the DFT of an ideal rectangular pulse [10]. With these figures we observe the limitation of the *home-made* pulser, which cannot generate a well-shaped pulse with duration less of 50 ns. Indeed, the problem is related to the *rise time* τ_R and the *fall time* τ_F of the rectangular step. In Fig.4.18 the measured negative square pulse is shown with the load/probe attached.

To show the different behaviours, we have chosen two different kind of probes, one with nominal central frequency of 2 MHz, the other with 10 MHz. Test were performed with the simple configuration in Fig.4.19, with an immersed setup.

When a load, like an ultrasonic probes, which has own internal impedance (we have seen previously how to model these devices), is connected to the circuit, the electric pulse which is going to excites the probes is slightly modified. In the left side of Fig.4.20, we observe how the rectangular pulse appears when the probes are attached. The signal is measured by placing the oscilloscope probes parallel to the first channel, which is the one connected to the exit of the pulser. On the right side of the same Figure, the magnitude DFTs of the rectangular pulses are shown, to compare the ideal

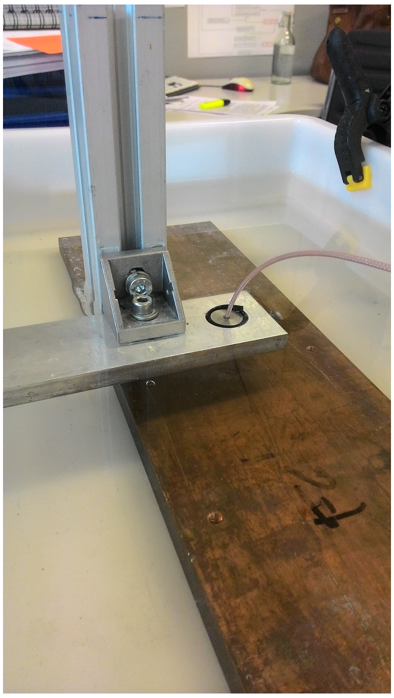

(a)

Figure 4.19: Pulse-echo setup for immersion tests. In the figure the planar copper slab is immersed in a tank full of water and the search unit is fixed at 15 mm above the copper surface.

DFT function with the real one. Since the energy associated at a corresponding frequency is proportional to the magnitude of the DFT spectrum, we are interested where the ratio $X(f)/X_{max}(f)$ is higher than possible.

The signal is measured by the second channel, parallel to the probe. These signals are reported in Fig.4.21, along with the magnitude DFTs for positive frequencies, in order to see various frequency contribution. We observe that the real central frequency is slightly below the 2 MHz; but looking at the wavelet, the maximum amplitude is obtained with the choice of the pulse width equal to half-period of the central probe frequency.

The same reasoning applies also for the 10 MHz ultrasonic probes, where this time the optimum pulse duration has to be of 50 ns. As we have just seen, since the pulser doesn't generates an optimal rectangular pulse, the final results are that the excitation is not perfectly synchronized with the right frequency and the transfer energy is not maximum, like in case in Fig.**??**(b). However, for the 10 MHz case, we observe a narrower wavelet, compared to the previous, since they are more time resolved; but, in frequency domain (*right* plots), the bandwidth is broader than the other for the 2 MHz case. Having a narrow wavelet might be quite useful if, but in conditions of low amplitudes, the reception process is more unstable and subjected to noise in general. It means that an accurate time position evaluation of the peak is quite hard, and, in addition, there's no a prominent sub-peak respect to the others inside the same wavelet. These facts reveal the difficulty of a possible continuation using this kind of piezoelectric disc.

We have found experimentally that the most corresponding excitation pulse is that of half period duration of the excitation pulse. For example,

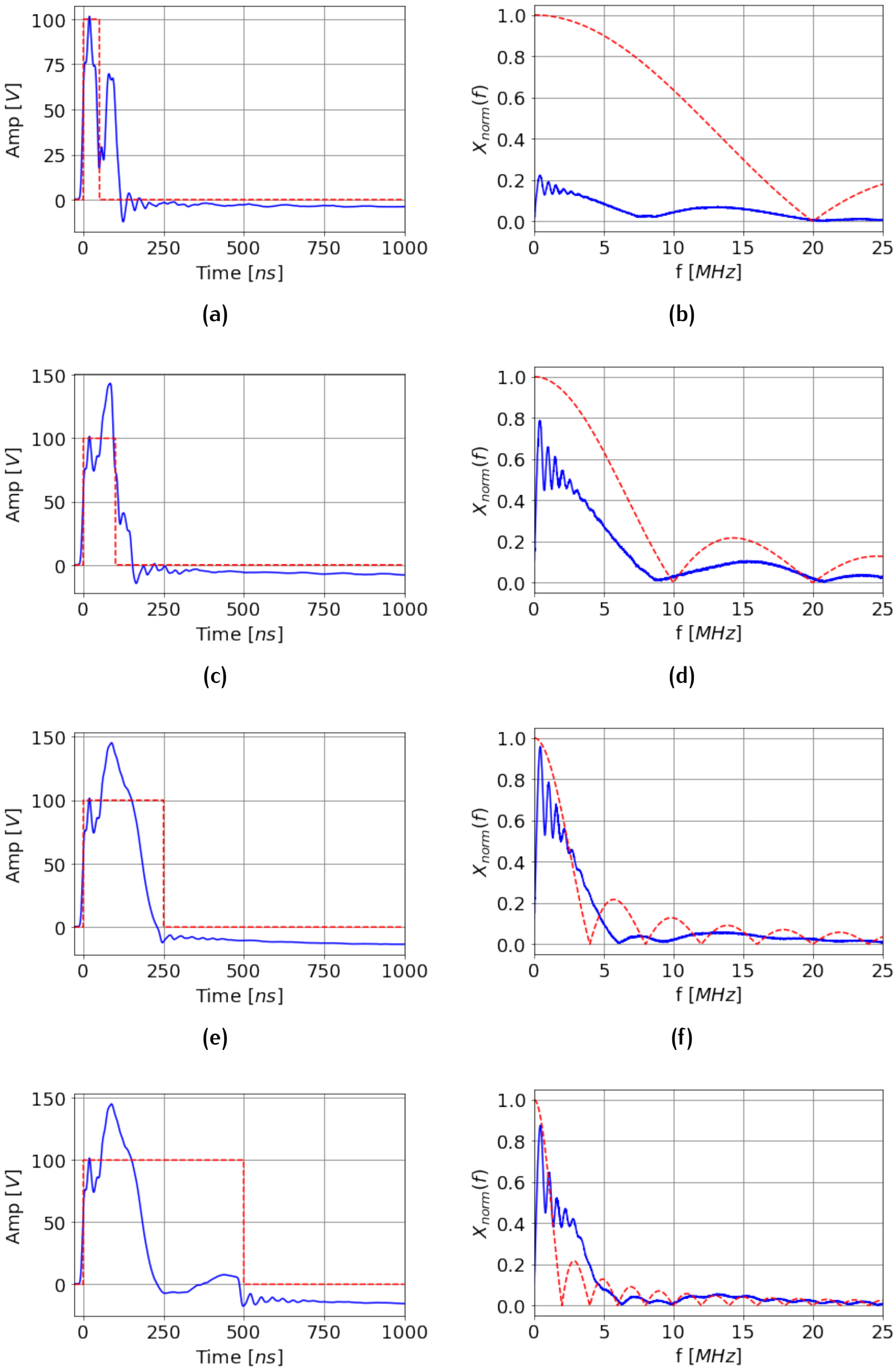

(a) (b)

(c) (d)

(e) (f)

(g) (h)

Figure 4.20: *Left plots*: output rectangular pulses with 2 MHz probe attached (*blue*) and ideal rectangular pulse (*red dashed*). *Right plots*: normalized magnitude spectrum of corresponding measured (*blue*) and ideal (*red*) pulses. (a)-(b) 50 ns;(c)-(d) 100 ns; (e)-(f) 250 ns; (g)-(h) 500 ns.

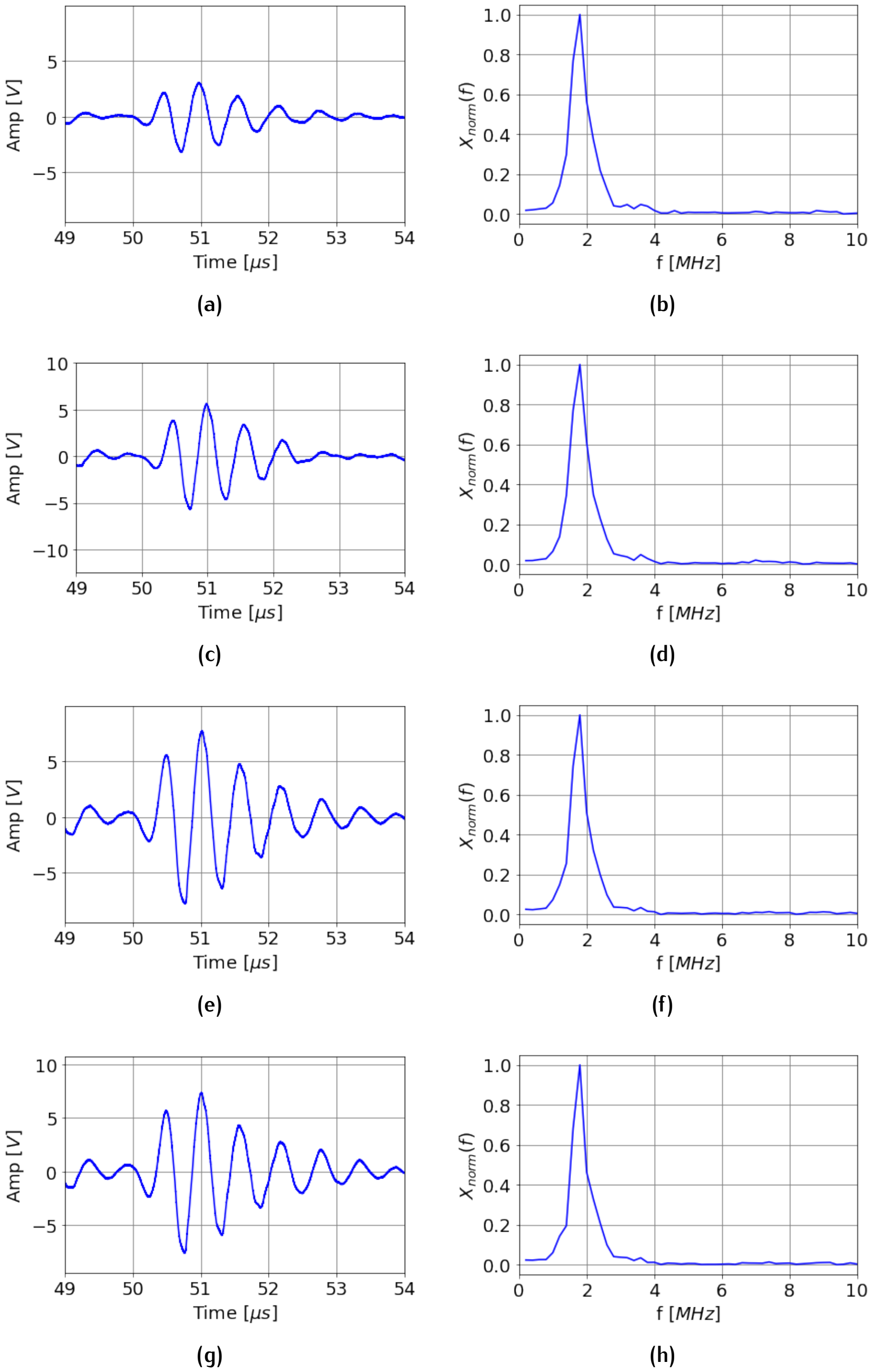

(a) (b)

(c) (d)

(e) (f)

(g) (h)

Figure 4.21: *Left plots*: Ultrasonic wavelet from 2 MHz probes reflected in the copper slab (see Fig.4.19). *Right plots*: corresonding normalized magnitude spectra. (a)-(b) 50 ns;(c)-(d) 100 ns; (e)-(f) 250 ns; (g)-(h) 500 ns.

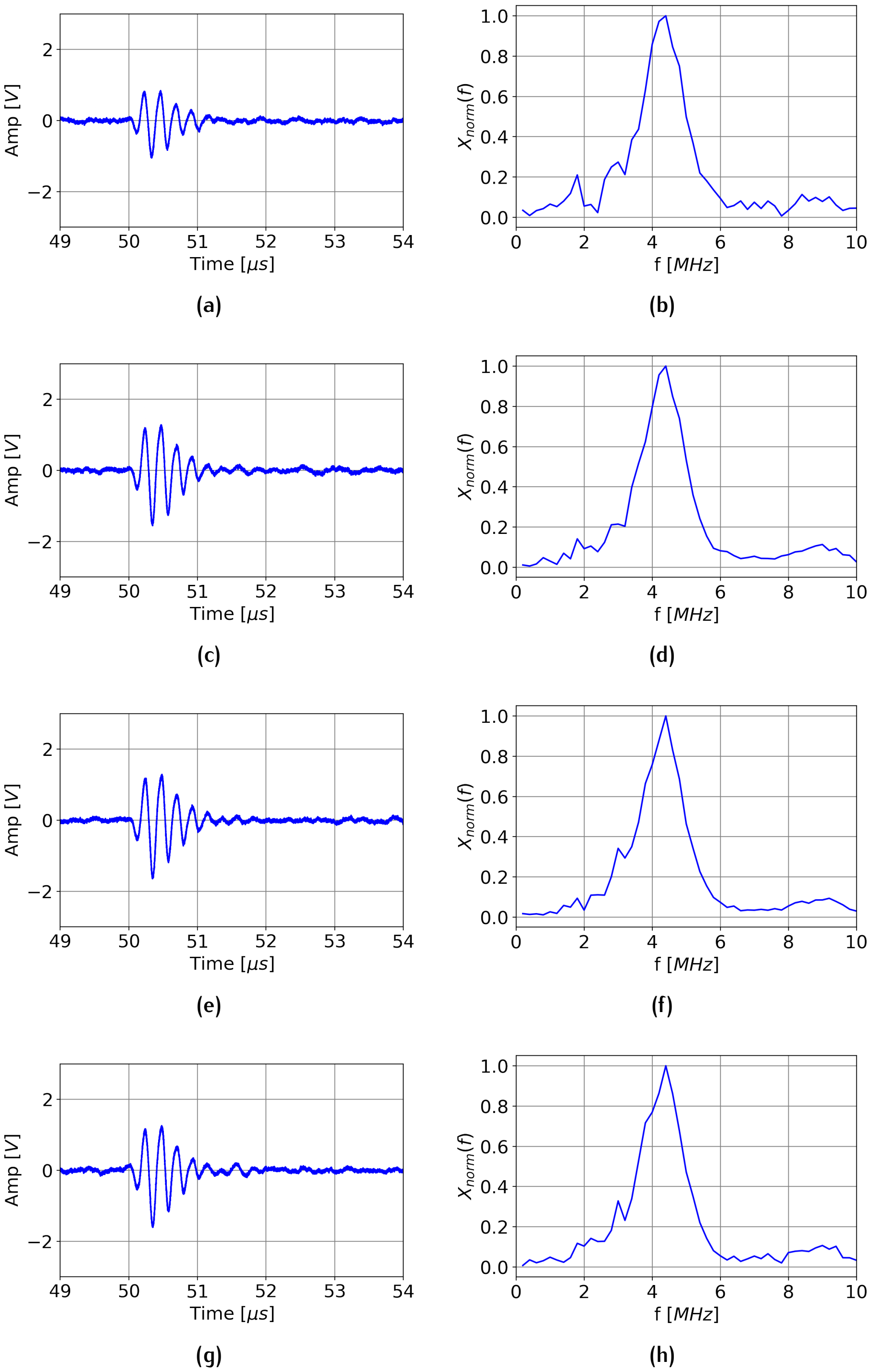

Figure 4.22: *Left plots*: Ultrasonic wavelet from 10 MHz probes reflected in the copper slab (see Fig.4.19).*Right plots*: corresponing normalized magnitude spectra. (a)-(b) 50 ns;(c)-(d) 100 ns; (e)-(f) 250 ns; (g)-(h) 500 ns.

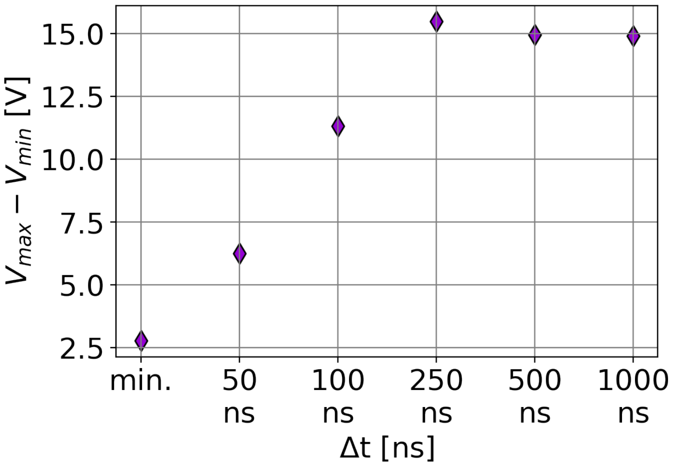

(a) Amplitude vs. pulse width for 2 MHz

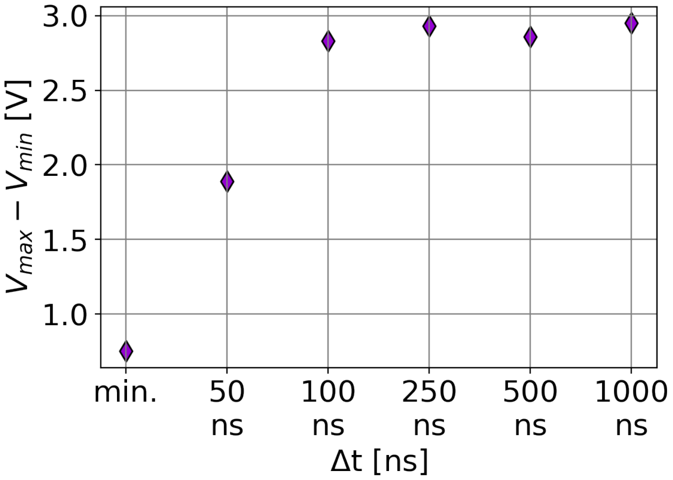

(b) Amplitude vs. pulse width for 10 MHz

Figure 4.23: Peak-to-peak amplitude of ultrasonic wavelet in Fig.4.21, shown as function of the pulse width.

with 2 MHz nominal frequency probes, the period correspond to 500 ns, or 0.5 µs, and the duration of the excitation pulse must be half of this, about 250 ns. This is also demonstrated by plotting the wavelet paek-to-peak amplitude produced against the different time width, in Fig.4.23(a). Indeed, the latter reports the situation both for 2 MHz than for 10 MHz probes. For the 2 MHz case, as previously said, it is clear the importance of setting the time width of the pulse at 250 ns, whereas for the 10 MHz the unexpected situation is that the peak-to-peak amplitude in not reached at the 50 ns value. An explanation for this is seen in Fig.4.22, where, even though the pulse width is chosen shorter and shorted, the final shape of the wavelet doesn't change: this can only mean that the specimen(copper) acts like a low-pass filter which filters out frequency higher than 5 MHz. Moreover, So, even with a shorted pulse, the wavelet's central frequency remains of value about 2 MHz. Also, with this observation we may conclude that using probes with nominal frequency higher than 5 MHz, could be quite inefficient, since they are more fragile and subject to wear.

4.4.3 Piezoelectric material selection

Frequency analysis allow to distinguish how piezoelectric discs defferently react to various stimuli and how the excited shape changes. For this reason, several test have been done in order to classify and select the best suited probes to be used. We selected three kind of commercial 2 MHz ultrasonic transducer, that we distinguish simply by calling them *type 1*, *type 2* and *shockwave*, where the former two are from different vendors, while the latter has a different kind of piezoelectric material, *i.e.* is made of piezocomposite. These signal are generated with a pulser voltage of 6 V and pulse width of 250 ns. A low voltage pulse is selected to maintain a low stress on the piezoelectric material, while the width is selected by the appropriate previous reasoning. Fig. 4.24 shows the different ultrasonic wavelet. The *type 1* transducer is the one with broader resolution in time, since many oscillation occur before completely attenuation, but it is also the most energetic one, at equal pulse stimulation. The *type 2* has similar behaviour to type 1 probe, but is more attenuated and a principal peak is distinguishable. *Type 3* instead is the more damped, with a single, negative, prominent peak. On the edge, it is completely damped, so this last one has the broadest bandwidth. In (d), the previous three wavelets are compared and the effect of the damping is quite evident. Probes 3 seems to be finer than the others, but its crystal is made of piezocomposite material, which is more fragile than the classic PZT.

So far,we have presented these two frequency type of transducers, even though in ultrasonic world there are many other possibilities. In this manner, we wanted to show the most relevant differences between these two extreme cases, but we have also done tests with 5 MHz transducer in laboratory. For these probes, we find that in the frequency domain the shape of the DFT is quite similar to those of 10 MHz; meaning that the copper acts like a low-pass filter for the ultrasonic beam. For our purpose, we find that 5 MHz probes are maybe the most effective, meaning a good compromised between wavelet resolution and transmitted/received energy even after multiple reflection inside the specimen.

4.4.4 Backing

Backing is usually a layer of epoxy resin used to control damping for the produced signal. Depending on the material, its load and the thickness deposited over the back plate influences the final outcome. Loading backing is a mechanical procedure where, before the resin solidifies, it is charged with heavy particle dust, usually tungsten, to increment the mass of overall backing. Moreover, a common procedure after the deposition of backing is the centrifugation: an ultrasonic probes installed in a housing and loaded with the epoxy resin is placed in a centrifuge. At the end the loaded particle in the mixture are distributed in a uniform way inside the compound. On the other hands, these procedure require additional working time and additional costs. Fig.4.25 shows the difference between two identical, 5 MHz probes, stimulated at the same frequency, but with the only difference of the centrifugated backing. This signal is a reflection inside the copper, after a

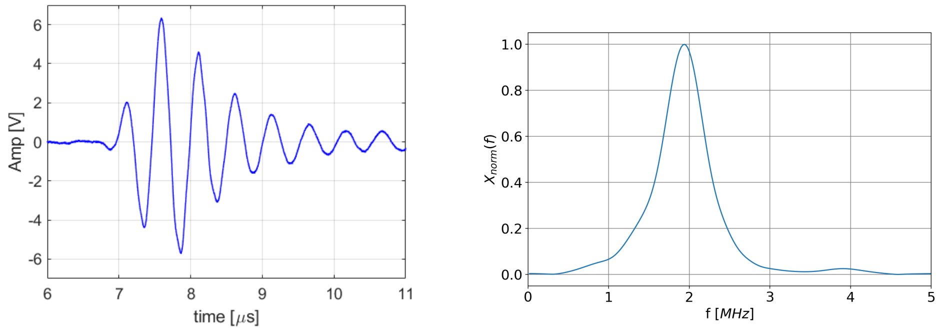

(a) Type 1 wavelet **(b)** Type 1 magnitude spectrum

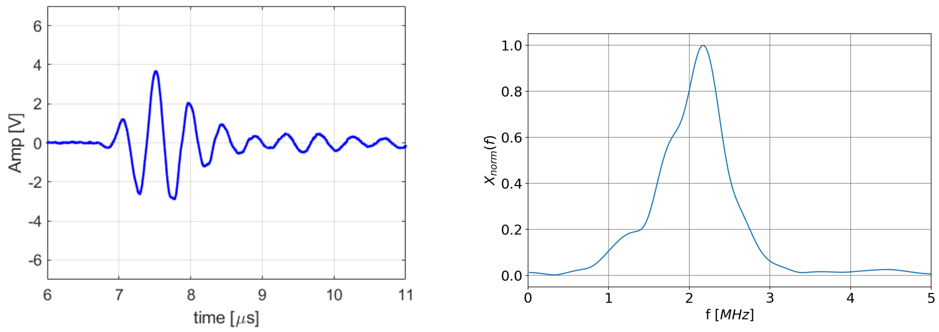

(c) Type 2 wavelet **(d)** Type 2 magnitude spectrum

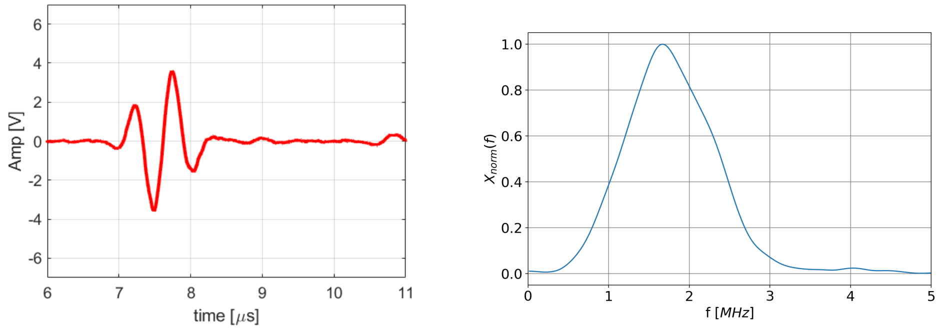

(e) Type 3 wavelet **(f)** Type 3 magnitude spectrum

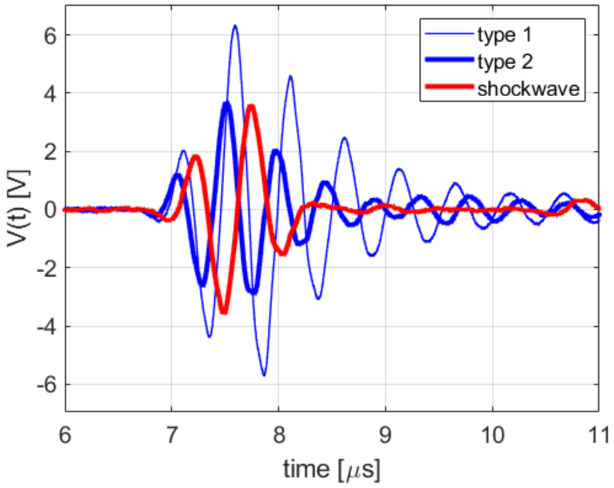

(g) Comparison of the three wavelets, 2 MHz

Figure 4.24: Signal and DFT comparison from different ultrasonic probes.

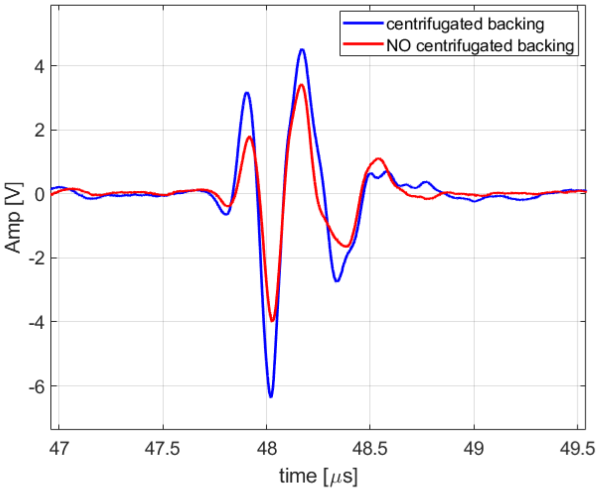

Figure 4.25: Comparison between probes at 5 MHz nominal frequency. *Blue*: with centrifugated backing; *blue*: with not centrifugated backing.

path including a substrate (Rexolite) and water. The blue signal is the one with the centrifugation, whereas the red has not: the difference between the two absolute peaks are evident, and also the shape is slightly different. However, this difference has not too importance for our scopes, since even with a non centrifugate backing, a narrow wavelet is obtained.

Looking again at Fig.4.25, we find from that 5 MHz probes are the most suitable ones in terms of final amplitude and time resolution, having a single prominent peak, instead of multiple sub-peaks.

4.5 STEPS FOR TEMPERATURE ACQUISITIONS

The main issue of these experiments regards how to perform a controlled temperature measurement at different steps, at the same time with ultrasonic acquisition. Instead to directly heat the copper specimens, the most efficient way if the higher temperature target does not overcome 55 °C-60 °C is to use a thermal bath with an heat circuit including a pump and a boiler. With a thermocouple, it is possible to monitor the increase of temperature of the water and, at same time, since the heating proceed slowly, of the copper. Since copper is an excellent thermal conductor, its temperature strictly follows the trend of the water temperature which is immersed in. However, the more the process of heating takes long, the more accurate will be the sample temperature measure. The experimental procedure we have followed is the same for all the temperature tests we performed, with this logic:

1. Start with a T_0 equilibrium temperature of the overall system water and copper;

2. Take acquisition of time of flight (TOF) in copper specimen at T_0;

3. Increase the temperature of the water/copper system by an interval ΔT;

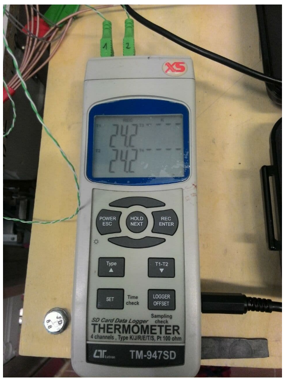

Figure 4.26: Digital thermometer used in experiments. 4 channel, 0.1 °C sensitivity.

4. Take acquisition of TOF at temperature $T + \Delta T$;
5. Repeat cycle 3-4 until the maximum boiler temperature is reached;

The digital thermometer TM-947SD (Fig.4.26) has 4 channels for data acquisitions, and an available SD storage. It works with at most 4 different thermocouples, in this configuration we have chosen of type K. The console application in C++ has been designed in order to acquire digital temperature through the RS232 serial port. The temperature are then transmitted to the GUI to visualize the trend in real time, and saved in a header along with the other card parameters (pulse width, amplitude, gain and so on). Instrument resolution is 0.1 °C. To achieve the higher precision, certified thermocouples have been used to obtain a mean reliable value of the temperature detection, with a uniformity around the point of measurements. The choice is practically dictated from the preliminary simulation model, which shows that the temperature constant behaviour in the volume near the interested region. The best way has been the perforation of the copper specimen in that region, drilling small size diameter channel at the nearest measurement point in the copper.

4.6 CONCLUSIONS

In this Chapter all the instrumentations and the charaterization of the ultrasonic transducer parameters have been explored in details. The setup has been described briefly in its general terms, and then the different implementation for the various tests. In particular, the differences have been emphasized between the state of the art, referred to the Eurosonic-Mistras device and the custom protoptye. Eventually, the description of each important part of the transducer has allowed to understand the need for the task which is to measure time differences between the echoes of the same signal. The topic of the signal elaboration will be discussed in the next Chapter.

5 METHODS AND PROCESSING OF EXPERIMENTAL DATA

5.1 OVERVIEW

This Chapter shows the numerical techniques adopted for the processing part of the software, aimed at real-time signal reconstruction. The goal is to retrieve a method for performing a precise measurement of the time-of-flight (TOF) from the ultrasonic signals generated with the experimental system described above. As a first approach, cross-correlation has been used, since it is the most immediate technique for studying the difference between two very similar portions of a signal, such as two echoes of the same signal may be. Despite the method's high accuracy, it is excessively onerous for the computational load of a microcontroller which executes instructions in real-time, for a high repetition rate. Therefore, for these reasons, a combined reconstruction technique based on signal interpolation with the addition of quadratic regression on the maximum peak's neighbors has been studied. This technique reconstructs a digital sampled signal from low-frequency sampling, that is, slightly grater than 2-3 times the maximum detectable frequency in the system: the limit for reconstructing a signal in a fully determined way is given by the *sampling theorem*. This procedure reduces the computational and economic cost for the realization of the electronic components. In this way it is possible to obtain a stable and more accurate estimate of the time peak and amplitude that would not be possible to obtain on the sampled data alone. Through the application of a low-pass filter in the affected portion of the signal, to which a *padding* of zero between samples has been applied, a denser curve of points is obtained. Maximum estimation is then performed with a quadratic regression calculation on the area around the peak of maximum amplitude. This procedure is then applied to both signal echoes, called Cu_1 and Cu_2, and then the time difference is calculated. This procedure is still implemented in software written in C++ that acts in real time on the acquired signal.

5.2 DESCRIPTION OF THE PROBLEM

The ultrasonic probe used in the experimental measurements is the same one that was described in Chapter 4, and which we resume here for convenience, in Figure 5.1(a). The transducer is coupled with the wedge material, which is placed at a distance from a copper plate that would form the wall of the mould in the industrial plant. In between, there is a water gap. The propagating beam travels from the transducer through the wedge and the water gap to the inner surface in the copper, then is reflected. The signal that is detected on the oscilloscope is shown in Fig.5.1(b). In this signal we observe, starting from the excitation pulse detected at the beginning, the successive echoes in temporal order that the transducer receives. The first signal, in the area between 20 µs and 30 µs, represents the superposition of two signals.

5.2.1 Boundary conditions on the geometry

The configuration of the layers shown in Fig.5.1 is possible in a way that the two intermediate reflections constitute the internal reflection signals in the copper plate are as isolated as possible from the rest of the signal. To realize this measurement the following boundary must be satisfied:

$$\Delta t_{Rex} = \Delta t_W \tag{5.1}$$

$$\frac{2\,L_{Rex}}{c_{Rex}} = \frac{2\,L_W}{c_W}. \tag{5.2}$$

Therefore, the condition 5.1 is rewritten in terms of the water thickness L_W. The ratio between the velocities of Rexolite and water is approximately

$$\frac{c_{Rex}}{c_W} \simeq \frac{2.2\,\mathrm{mm\,\mu s^{-1}}}{1.5\,\mathrm{mm\,\mu s^{-1}}} \simeq 1.47 \tag{5.3}$$

$$L_{Rex} = L_W\,\frac{c_{Rex}}{c_W} \tag{5.4}$$

$$= 1.47\,L_W. \tag{5.5}$$

This allows the thickness of the Rexolite to be chosen to match the existing thickness of water. Especially when it comes to the design of the industrial setup, an important constraint in the design is definitely the thickness of water between the wall of the mould and the surface of the Rexolite, i.e., the material supporting the probe. In fact, the thickness of water is the fundamental parameter that governs the intensity of heat transfer of the ingot, as the heat transfer coefficient h will depend on it. Changing the thickness of the water gap changes the cross section of the water channel and the flow conditions. Therefore, this thickness can be changed within certain limits, in a way to not compromise the heat transfer in that critical region, the region of early solidification.

5.3 CROSS-CORRELATION

The first approach we have applied for the accurate calculation of the TOF through time position peak difference is the cross-correlation, which represent the measure of similarity between two signal as a function of translation in time, applied to one of them [29], and it's the simplest idea to calculate the time difference. In this context this technique appears appropriate, since the successive reflection are indeed almost identical, although attenuation acting through propagation in material changes the signal amplitude as it goes on.

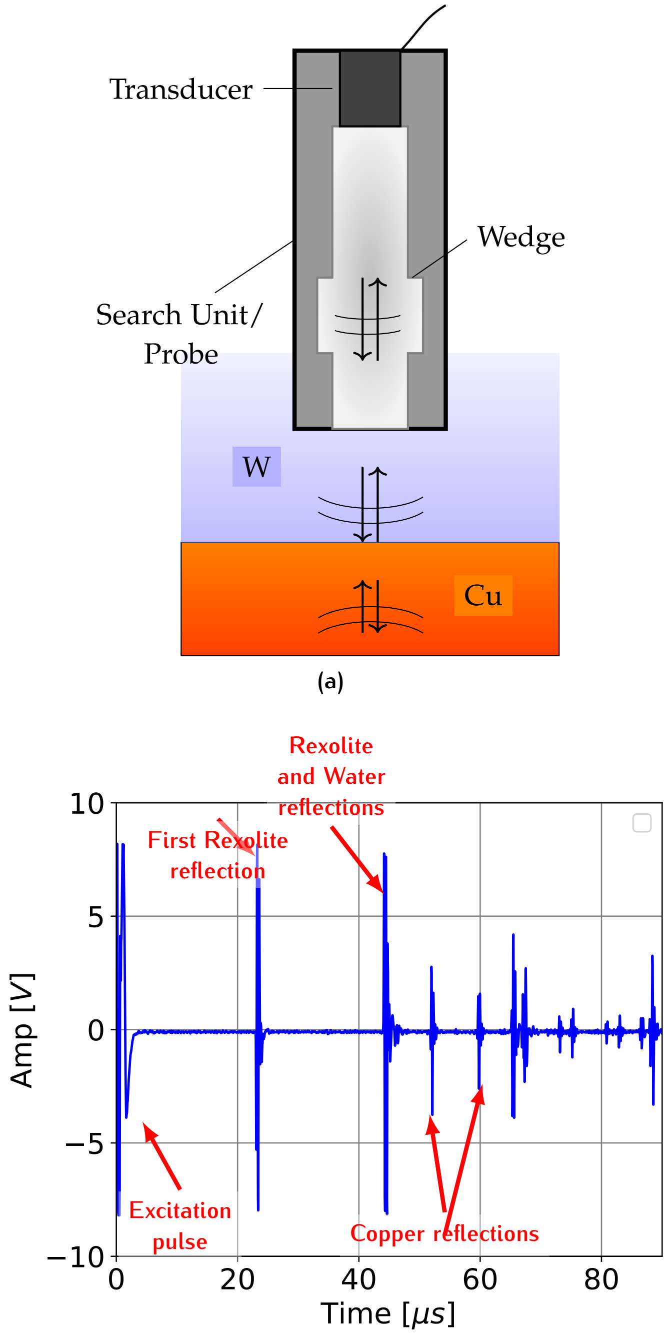

(a)

(b)

Figure 5.1: (a) Model of the three system layer. (b) Ultrasonic signal measured in a three-layer system with the following widths $L_{Rex} = 38\,\text{mm}$, $L_W = 26\,\text{mm}$, $L_{Cu} = 19\,\text{mm}$.

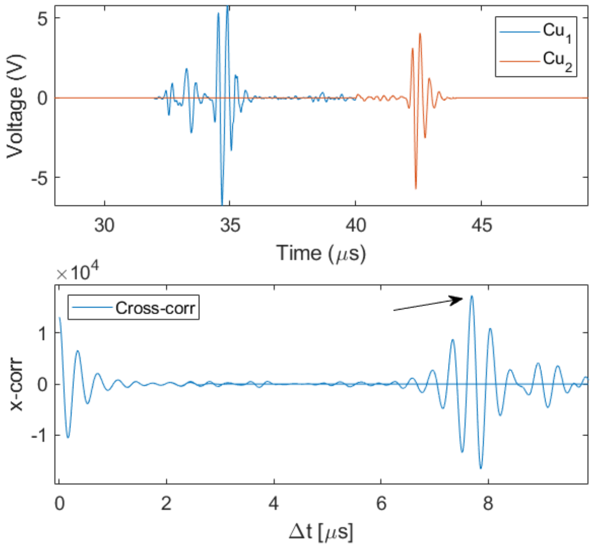

Figure 5.2: *Above*: the two section of signal with Cu_1 and Cu_2. *Below*: cross-correlation of two signal. The black arrow indicates the maximum corresponding to the time delay Δt.

Indeed, the second reflection in copper, called with notation Cu_2, is expected to be attenuated replica of the first wavelet Cu_1, but only translated in the time axis. Keeping this two portion of signal independently, consider the first portion Cu_1 and the second one Cu_2: the cross-correlation evaluates the integral of the product of all the possible displacement values, bringing forward the second signal Cu_2. By definition, we have

$$R_{Cu_1,Cu_2}(t) = (Cu_1 \star Cu_2)(t) = \int_{-\infty}^{+\infty} Cu_1^*(t) Cu_2(t+\tau)\, d\tau. \tag{5.6}$$

The maximum value of this integral is so obtained when the two signal coincide, so when they are overlap. Since they are not identical, cross-correlation does not result in an unique peak, but in a oscillating behaviour as expressed in Fig.5.2. The maximum position in time of the resulting wavelet then correspond to the time delay $\Delta t = t_{Cu_2} - t_{Cu_1}$.

If this approach is applied for every signal acquisition at each temperature, the linear relation is found. Disadvantages of using the cross-correlation techniques are primary that it is very computationally expansive, if we want to implement it in a real-time application like this particular one. There's no problem in keeping post-process analysis, but it is not feasible with an industrial embedded microcontroller, where low resources do not allow computationally efforts such like this. This is the reason why we have searched for other numerical techniques to extract the most valuable information from the signals.

5.4 SAMPLING PROCESS

Periodic sampling is the process of acquisition of discrete samples from a time-continuous signal ([10]). Since we can't store in a computer infinitesimal spaced samples, we practically need to set a convenient sampling rate

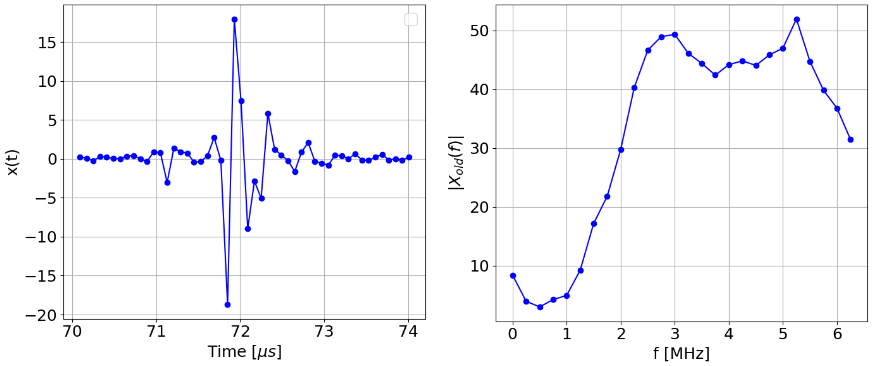

(a) (b)

Figure 5.3: (a) Segnale campionato a 12.5 MHz su finestra primo picco del rame, *i.e.* Cu_1; (b) DFT del segnale finestrato. Il numero di punti è la metà rispetto a quelli del segnale per ragioni di simmetria.

to acquire the continuous time signal, being sure to recover then from these values the original information.

Il criterio più importante da considerare quando si opera nel campo del campionamento del segnale digitale è il *criterio di Nyquist* [16],[25] . Essi stabilisce un limite teorico da non superare se si vuole ottenere da un segnale reale delle informazioni senza perderle. Infatti, lo spettro in frequenza di un segnale raccoglie delle informazioni fondamentali che nell'atto del campionamento possono andare perdute. In practice, it says that to recover the original spectral content for a signal, we have to choose a *sampling rate* $f_s \geq 2f_{MAX}$ at least greater than two times the signal *maximum frequency component* f_{MAX}, usually indicated as B. Ultrasonic signals like those generates from a common NDE system are of course *band-limited signal*, where the spectral amplitude decays to zero outside a certain band interval $\pm B$ ([10]). [1]. Fig. 5.3 (a) shows a registered 12.5 MHz sampled signal, along with its magnitude frequency response (b), obtained performing the Discrete Fourier Transform (DFT). Since real signals are finite and sampled signals, DFT operation generates discrete complex values outputs. Due to DFT symmetry, half of the complex DFT outputs are redundant, so only $N/2+1$ positive-frequency points are shown. The sampling period is

$$\Delta t_s = \frac{1}{f_s} = \frac{1}{12.5\,\text{MHz}} = 80\,\text{ns} \tag{5.7}$$

We first notice that this sampling rate is at least sufficient in order to capture the frequency information in the signals. Referring to the same signal, the first point near the maximum is the lowest absolute point, meaning that the resolution to distinguish the rapid oscillation is Osservando lo stesso segnale, ci si accorge come il punto più vicino al punto di massimo sia quello di minimo, indicandoci che questa frequenza di campionamento non è sufficiente per ottenere unan buona stima del picco massimo. Questo perché l'acquisizione del segnale digitale dipende in buona parte anche da fattori

---

[1] This is of course an approximation: band-limited signal merely implies that signal energy in these region is below the sensitivity of our system.

casuali come il jitter dell'elettronica, e quindi non si può essere sicuri che i punti effettivamente presi rappresentino i valori massimi e/o minimi del segnale.

This depends on the low ratio f_s/f_c like the one used in our experiments; the main effect on the sampled signal is that frequency at high values are not completely attenuated. To calculate the minimum requested points per wavelength, to describe the resolution of the sampled countnerpart, we can make the following considerations: let's assume the signal is approximated with a monochromatic wave propagating with frequency f_c, sampled at f_s. While the sampling frequency is 80 ns, the period of the wavelet can be assumed to be

$$T = \frac{1}{f_c} \simeq \frac{1}{3\,\mathrm{MHz}} \simeq 333\,\mathrm{ns}. \tag{5.8}$$

Then the number of samples per wavelength is about

$$n = \frac{T}{T_s} = \frac{T}{\frac{1}{f_s}} = \frac{333\,\mathrm{ns}}{80\,\mathrm{ns}} \simeq = 4.2. \tag{5.9}$$

In these conditions the estimation of peaks amplitude is affected by imprecision. [19] assume that in order to recover the true or most probable amplitude the signal must be sampled at least 5/6 f_c, other even 10 f_c. In this case, we can just say that recover amplitude information is quite difficult, and not reliable. This fact can also be critical for the correct reconstruction of the original spectral components since the discrete spectrum of the sampled signal, which is periodic in the frequency domain, can overlap in the band portion between the maximum frequency value limited by the bandwidth and the Nyquist frequency (half sampling frequency).

This means that we expect high frequency components above the Nyquist frequency cannot be captured by this sampling rate; indeed, the 12.5 MHz sampling rate isn't sufficiently above the requested threshold established by the Nyquist criterion, since the maximum frequency component isn't zero at $f_s/2$. However, that this recommendation has fundamental importance if we want to recover the original information about all the frequency components of the signal, in the entire spectrum range. Despite this, the method of interpolation does not invalidate the conclusion here obtained. The introduction of an interpolation technique based on *low-pass filtering* attenuates these components and does not influence the final behaviour of the relative time-position peaks between multiple reflections, although the final shapes of these signals have changed.

5.5 SIGNAL INTERPOLATION

Interpolation is a digital processing technique used to reconstruct signal samples between the original ones. Sometimes it's not possible to perfome the requested sampling due to electronic limit or other reasons: interpolation by low-pass fitering is a numerical solution to retrieve the desirable request. Foundation of interpolation techniques can be found in a large amount of literature, and it has a long history [10]. Roughly speaking, we can summarize

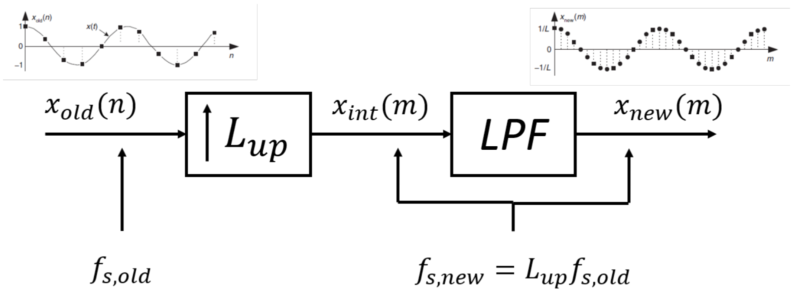

(a)

Figure 5.4: The interpolation by low-pass filtering scheme.

this technique in this way: null values are inserted between the old $x_{old}(n)$ samples by a number $L-1$, creating a longer sequence. In Fig. 5.4, this operation is depicted like the raw signal that enters into the first box, where the operator $L\uparrow$ acts doing the so called *zero-stuffing*, inserting $L-1$ zeros between each sample. Next, the intermediate signal $x_{int}(m)$ enters in the low-pass filter box, here depicted as LPF, exiting in the new smoothed form $x_{new}(m)$. The $x_{new}(m)$ signal has an amplitude reduce by a factor L, which is the upsample factor. So when the output signal is obtain, each sample must be multiplied by L.

In Fig.5.5 we describe the intermediate steps for the interpolation, applied to the example reported in Fig.5.3. The sampled frequency is $f_{s,old} = 12.5\,\mathrm{MHz}$ and the chosen upsample factor is $L = 8$. When the zero are inserted between the original samples $x_{old}(n)$, obtaining the sequence $x_{int}(m)$, the resulting spectra $X_{int}(f)$ contains multiple *images* within the interval $[0, f_{s,new}]$. This fact is a direct consequence of performing the DFT on a L times longer signal with 1 *original* sample and $L-1$ zeros padded between two original samples. The new generated spectra is therefore more dense and has more points. The procedure at this point is to low pass filter through *ad-hoc* designed digital filter the intemediate x_{int} output: the overall process produce a delayed signal which has a slightly different shape from the original one. The output depends on the parameters of the filter: the order, the upsample factor L, and the cutoff frequency. Moreover, due to the upsampling process, the insertion of $L-1$ zero-valued samples produce an amplitude loss factor when a unity-gain low-pass filter is used, which is compensated by multiplying by the L_{up} term. In the process of new signal construction, it occur that the majority of the multiplication becomes zero, since the *zero-stuffed* signal has $L-1$ zeros for each non-null sample: the peak sample value of $x_{new}(m)$ is equal to the peak sample value of $x_{old}(n)$ divided by L. The cutoff value of the filter changes the original shape, removing higher frequencies of the signal. These components create the ripple around the principal peak. As a secondary effect, the final shape of the signal appears slightly different from the original one, in terms of sub-peak shapes and higher frequency content. Of course this could be a problem if the aim of this procedure is to retrieve Questo può essere un problema se lo scopo che abbiamo è quello di ricostruire nella maniera più accurata possibile il segnale, nei suoi dettagli. Invece, ci interessa ricavare un intorno di punti che rappresenti il massimo, e su cui fare la regressione di una parabola.

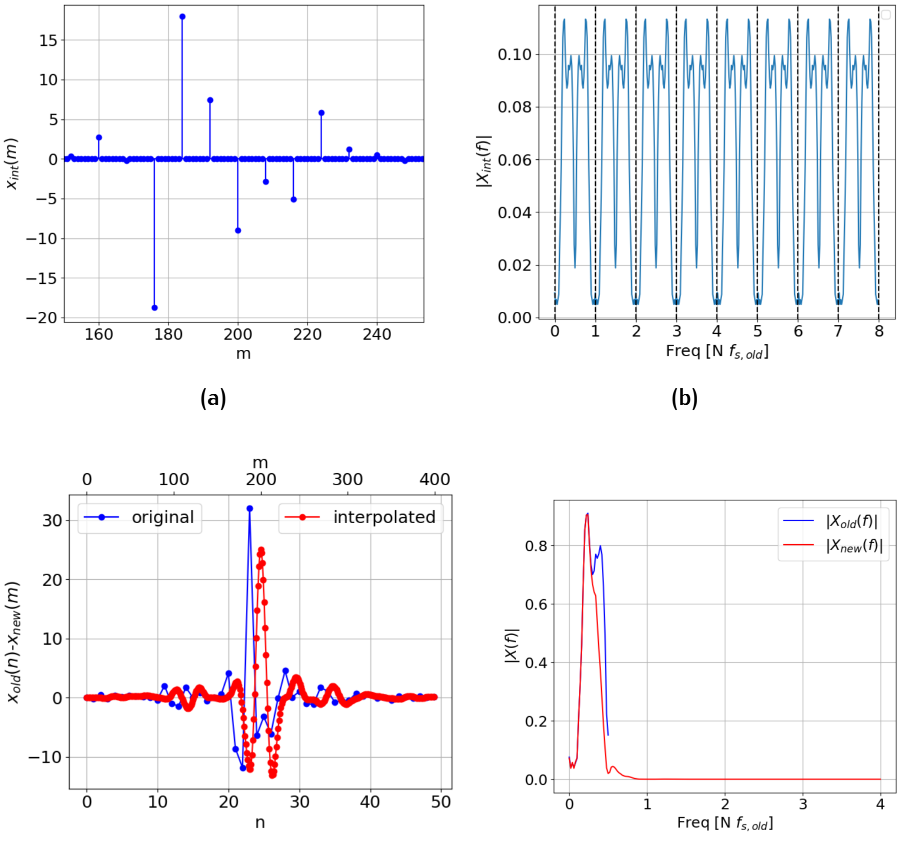

(a) **(b)**

(c) **(d)**

Figure 5.5: (a) Zero-stuffed signal sequence with $f_{s,new} = L_{up} f_{s,old}$, from signal in Fig.5.3; (b) Magnitude frequency response of zero-padded signal; (c) comparison between original (*blue*, $x_{old}(n)$) and interpolated one (*red*, $x_{new}(m)$); (d) Comparison between original (*blue*, $X_{old}(n)$) and interpolated (*red*, $X_{new}(m)$) magnitude frequency response.

Even though the filtering process generates some time delay in the time domain, this difference cancels out if the same filter is applied to two adjacent windowed signal, like can be two successive echoes measured in a pulse-echo configuration. In this way, also this problem cancel out and does not influence the final outcomes.

5.5.1 IIR low pass filter

Here we analyze the IIR (*Infinite Impulse Response*) filter design. The choice for this filter type is primary due to his higher performance compared to (FIR) *Finite Impulse Response* filter of the same order, reaching a sharper transition region roll-off and a reduced pass-band ripple. The order, in digital filter design, corresponds to the number of the feedforward and feedback coefficients. Moreover, the IIR filter requires less multiplication for each output sample, resulting in less computational operations. For details regarding theoretical aspect of digital filter design, see again [10].

The main problem is to determine the filter coefficients. The structure of a general IIR filter is:

$$\begin{aligned} y(n) = \frac{1}{a_0}[b_0 x(n) + b_1 x(n-1) + \cdots + b_P x(n-P) + \\ + a_1 y(n-1) + a_2 y(n-2) + \cdots + a_Q y(n-Q)], \end{aligned} \qquad (5.10)$$

where b and a are the feedforward and feedback coefficients. $x(n)$ are the signal samples to be filtered, while $y(n)$ are the outcomes. We observe that the n outcomes depend on the previous output, so this kind of filter is computationally expensive. It's clear that the more feedback coefficients we use, the elaboration will be expensive and the filtering operation too. In order to evaluate these coefficients and analyzing their properties, we develop a Python program with the aid of the open-source SciPy package. It contains standard libraries to perform many tasks in data analysis, an we focus on those regarding the signal processing and filtering. Starting from the key parameters like cutoff frequency, order and sampling frequency, we use the Python routine `scipy.signal.butter` to recover the N-th order Butterworth digital filter coefficients. Butterworth filters are designed to have the maximally flat filter magnitude response, with no amplitude ripple in either the passband or the stopband. However, they have the widest transition region respect the other popular design function, but this is not a problem, since the original bandwidth is limited and frequency response decays fast outside the region around the central frequency. Taking an example, for $L = 8$, the new sampling rate becomes $f_{s,new} = 100\,\text{MHz}$, so the new spectrum with its multiple images can be completely filtered out at the higher frequency, leaving unaffected the most important part. Indeed, the flat response of the Butterworth filter allows this.

Fig.5.6 show the two digital filter in a Bode diagram with their frequancy and phase response.

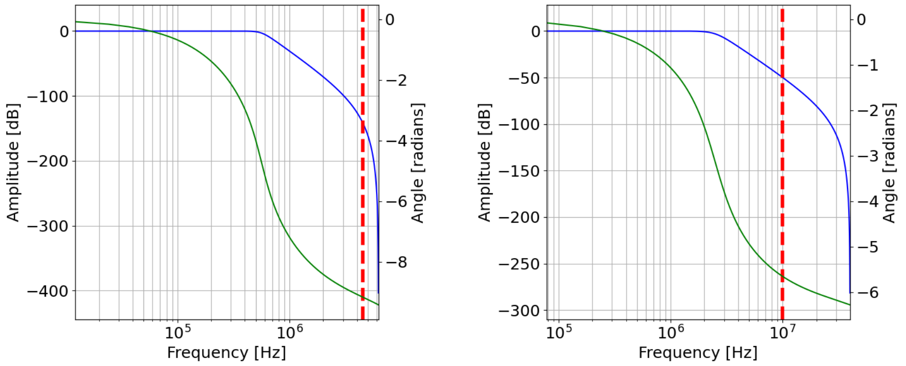

(a) IIR filter: $f_s = 12.5\,\text{MHz}$, $f_{cutoff} = 4.5\,\text{MHz}$, order 6.

(b) IIR filter: $f_s = 80\,\text{MHz}$, $f_{cutoff} = 10\,\text{MHz}$, order 6.

Figure 5.6: Properties of the digital filters applied in the analysis for the 12.5 MHz and the 80 MHz signals.

5.5.2 Least square fitting procedure

Referring again to the Fig. 5.3, we have emphasized the need to estimate quite accurately the position of the main peak. Ultrasonic signal can be very different, depending on transducer properties: different epoxy resins most influence the final shape of the ultrasonic signal, modifying the characteristic frequency band of the transducer [24]; piezoelectric cristal width and size could modify the nominal central frequency oscullation; different concentration of loading particle in the backing can improve more or less the damping factor, and so on. The reasons for various shape generally depend on particular needs for the user, and for our purposes, it turn out to be very convenient.

In this configuration, we made the assumption that the small region around the peak can be described by a *second order* polynomial, this for several reasons. Indeed, since we assumed that the materials in which ultrasounds propagate are homogeneous, we expect no particular deformation fo the original wavelet. Deformations on signal shapes generally occur when ultrasounds encounter internal defects, here scattering produce deformation and generation of other peaks that can be detected. In our case we have preliminary assumed the material under consideration is homogeneous: any possible defects and inhomogeneity due to the industrial processes are assumed to be negligible, compared to the used wavelengths in this field. The width of the layers under consideration are small enough to assume that we are considering the wave propagation phenomena in the near-field region. Indeed, we can use the approximation of plane waves. Another source of attenuation and deformation comes from grain scattering, due to the small size of the finite crystalline grain: this effect brings to a net loss of an amount of energy in the signal, that occurs in the direction of propagation [23]. During the propagation, these grain centres act like scattering sources for the shortest wavelength components, or highest frequency, acting in this way like a low-pass filter. So, considering long propagation paths contributes to a more relevant effect of shape distortion. However, this deformation effect

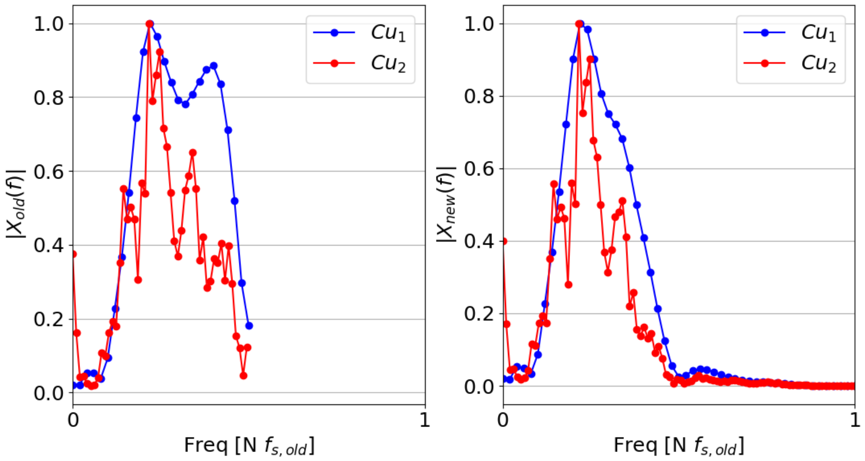

Figure 5.7: *On the left*: frequency magnitude response for Cu_1 and Cu_2 comparison for 12.5 MHz sampled signal. *On the right*: frequency magnitude response for Cu_1 and Cu_2 reconstructed wavelet with the following parameters of low pass filter: $L_{up} = 8$, cutoff frequency $f_{cutoff} = 4.5$ MHz, order $N = 6$.

is assumed to be negligible respect to other aspects, and in our experiments the ultrasonic path is always too short to see the effects of this material dispersion [11]. With these considerations, the assumption of regular shape and no deformation of the signal is a good approximation, so we expect that once a symmetric wavelet has been generated, the successive reflection maintain at least the main frequency components and that they do not vary noticeably between each other. In Fig. 5.7, these frequency magnitude response of Cu_1 and Cu_2 wavelets are represented: in the left there are the original spectra, where we observe that the magnitude of Cu_2 is more noisy than the first due to the lower signal to noise ratio; in the right, we observer the spectra of the new $x_m(n)$ signal. Compared to the those on the left, the action of the low-pass filter bring down the last bins near the $f_{s,old}/2$ (Nyquist frequency) limit. Also, this is more evident for the second wavelet Cu_2. The main contributions coming from the central bandwidth near the 2 MHz are not altered.

The interpolation scheme, has allowed to increment the resolution of the peak time positions of the acquired ultrasounds. However, the time discretization has passed from $t_{s,old} = 80$ ns for the original one, up to $t_{s,new} = 10$ ns for the upsampled one. The need of having a higher sensibility on the outcome of time peak position, respect than the only interpolated signal, we develop a procedure to recover this information by using a least square fit over the points around the main peak region.

In Fig. 5.8 (b) we observe the estimate for the parabolic curve in this small region. This procedure is quite simple, since the estimation of the LS coefficients can be done analytically and implemented in a numerical procedure. In conclusion, the overall procedure, interpolation plus least-square fit isn't quite computationally expansive.

The LS method gives us the coefficients describing the polynomial curve which best describe the shape of this region. Given N_{fit} the number of points around the maximum and k_{max} the discrete index where is located

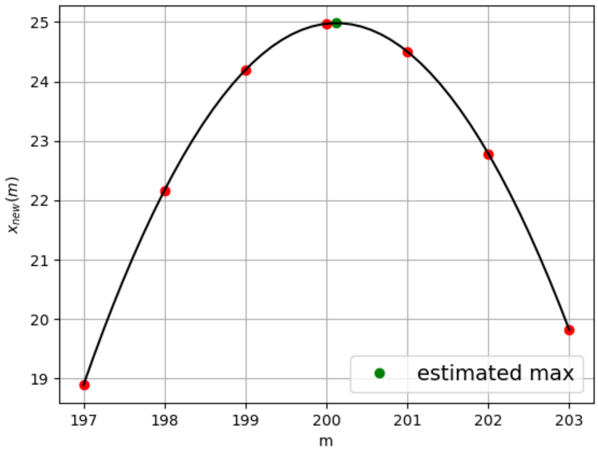

(a)

Figure 5.8: Zoom on signal peaks where LS fit procedure is applied: the red dot represent the interpolated samples of the signals, the black continuous line is the estimated curve. The green dot is the final estimate of the maximum.

the maximum, the LS method minimize the sum of the differences between the estimate $\hat{x}_k$ and the $x_{new}(m)$ value, symmetrically chosen around the peak:

$$R^2 = \sum_{k=k_{max}-N_{fit}/2}^{k_{max}+N_{fit}/2} \left(\hat{x}_k - x_{new}\left[k\right]\right)^2 \tag{5.11}$$

where $\hat{x}_k$ can be expressed like a second-order polynomial, in function of the time index $t[k]$:

$$\hat{x}_k = a_0 + a_1\, t[k] + a_2\, t[k]^2 \tag{5.12}$$

.

5.5.3 Python class `InterpFilter`

In this section we report the fundamentals part of the numerical codes used for the signal analysis, performed with the electronic hardware just explained, which have produced the shown results. The core part is the interpolation algorithm, already explained in the scheme in Fig.5.4. To perform such analyses the numerical codes have been gathered in a Python modules. The digital filter construction is made by the class `InterpFilter` which contains the key properties of the digital filter and the methods to perform the *upsample* procedure.

The method of the class are:

- `__init__`: for the initialization of the type of the filter (Butterworth, Chebyshev, . . .), f_{cutoff}, order N, sampling frequency f_s and upsample factor L_{up};

- `fbuildinterpfilter`: return the coefficient a and b of the filter defined in Eq.5.10, along with ω and h, the frequency (units of f_s) and the response function H:

$$H(e^{j\omega}) = \frac{b_0 + b_1 e^{-i\omega} + \cdots + b_P e^{-i\omega P}}{a_0 + a_1 e^{-i\omega} + \cdots + a_Q e^{-i\omega Q}}. \tag{5.13}$$

- `fupsample`: realises the *zero-padding* procedure and the *upsample*, by filtering the zero-padded signal with the low pass filter;
- `write_param_filter`: write the filter parameter on file;
- `plot_bode` : plots the Bode;
- `impulse_response`: calculates the impulse response function, *i.e.* the response of the filter at the Dirac delta excitation.

```python
class InterpFilter:

    def __init__(self,ntfilter):
        '''
        Initialize IIR filter parameters
        '''
        self.filtertype = ntfilter.type
        self.cutoff = ntfilter.cutoff
        self.order = ntfilter.order
        self.fs = ntfilter.fc
        self.Lup = ntfilter.Lup

    def fbuildinterpfilter(self):
        '''
        Build IIR filter coefficients
        '''
        fsup = self.fs*self.Lup
        nyq = 0.5*fsup
        norm_cutoff = self.cutoff/nyq
        b,a = dsp.butter(self.order,norm_cutoff,output=’ba’)
        # w, h = dsp.freqs(b, a)
        # DIGITAL FREQUENCIES (default N=512)
        w, h = dsp.freqz(b, a)#, plot=self.plot_bode)
        return a,b,w,h

    def fupsample(self,vdata,debug=False):
        '''
        Zero-padding and interpolation
        '''
        vdata = np.array(vdata)
        self.fsup = self.fs*self.Lup
        # filtertype =’butter’
        a,b,w,h = self.fbuildinterpfilter()
        xup = np.zeros(vdata.size*self.Lup)
        for i in range(1,vdata.size):
            xup[::i*self.Lup]=vdata[i]

        return self.Lup*dsp.lfilter(b,a,xup)

    def write_param_filter(self,order,fs, Lup):
        '''
```

```
        Save filter coefficients
        '''
        fsup = fs∗Lup
        a,b,w,h = self.fbuildinterpfilter(fsup)
        print("coef a filter: ", a)
        print("coef b filter: ", b)
        print("coef w filter: ", w)
        print("coef h filter: ", h)

        file = open("coef_filtri.txt","w")
        out = "Lup = " + str(Lup) + "\n"
        file.write(out)
        out = "filt_na = " + str(order+1) + "\n"
        file.write(out)
        out = "filt_nb = " + str(order+1) + "\n"
        file.write(out)
        out = "filt_order = " + str(order) + "\n"
        file.write(out)

        for i in range(0,order+1):
            out = "filt_a" + str(i) +  " = " + str(a[i]) + "\n"
            file.write(out)
        for i in range(0,order+1):
            out = "filt_b" + str(i) +  " = " + str(b[i]) + "\n"
            file.write(out)
        file.close()

    def plot_bode(self,w,h):
        '''
        Plot Bode diagram
        '''
        # multiply for f_s/2pi renormalize
        flp = w ∗ self.fs/2.0/np.pi
        fig, ax = plt.subplots()
        ax.semilogx(flp, 20 ∗ np.log10(abs(h)),’b’)
        ax_phase = ax.twinx()
        angles = np.arctan(np.imag(h)/np.real(h))*180.0/np.pi
        ax_phase.plot(flp, angles, ’g’)

        ax.set_title(’Butterworth filter frequency response’)
        ax.set_xlabel(’Frequency [Hz]’,fontsize=ULTRA_SIZE)
        ax.set_ylabel(’Amplitude [dB]’,fontsize=ULTRA_SIZE)
        ax_phase.set_ylabel(’Angle [radians]’,fontsize=ULTRA_SIZE)
        ax.margins(0, 0.1)
        ax.grid(which=’both’, axis=’both’)
        ax.axvline(self.cutoff, color=’green’) # cutoff frequency

    def impulse_response(self,):
        '''
        Calculate filter impulse response
        '''
        delta_dirac = np.zeros(512)
        delta_dirac[0] = 1.0
        a,b,w,h = self.fbuildinterpfilter()
        iir_response=dsp.lfilter(b, a, delta_dirac)

        fig, ax = plt.subplots()
        ax.plot(iir_response,’b-o’)
        ax.set_xlabel("n",fontsize=ULTRA_SIZE)
        ax.set_ylabel("h(n)",fontsize=ULTRA_SIZE)
```

```
        ax.grid()
        return iir_response
```

Code Listing 5.1: Class `InterpFilter`

5.5.4 Function `fitquadratico`

The second part of the interpolation algorithm deals with the parabolic fit on the upsampled signal. This is done taking points in the near of the maximum, and performing the regression on these selected ones. The `polyfit` NumPy's function performs this operation quite well, fitting a polynomial of desired order. It returns the coefficient which are used to retrieve the maximum position, which is done by the called `parable_vertex` function.

```
def parable_vertex(p):
    '''
    Calculate vertex coordinates (x,y)
    in the parable :
    x_v = -b/2a ;  y_V = c - b^2/4a

    Parameters
    ----------
    p : (a,b,c) parable coefficients

    Returns
    -------
    x : x coordinate
    y : y coordinate
    '''
    x = -0.5*p[1]/p[0]
    y = p[0]*p[2]-0.25*p[1]*p[1]
    y/= p[0]
    return (x,y)

def fitquadratico(x,npoints=3,imax=None):
    '''
    Calculate vertex of the fitted parable

    Parameters
    ----------
    x : Input array of x points
    npoints : number of points in the left and right
    imax : x-index position of maximum


    Returns
    -------
    vert : (x, y) of parable vertex
    p : (a,b,c) parable coefficients
    r : array of x-coordinate index (imax-npoints;imax+npoints+1)
    x[imax] : x coordinate position of interpolated maximum

    '''

    if imax==None:
        imax = np.argmax(x)
    r = np.arange(imax-npoints,imax+npoints+1)
    p = np.polyfit(r,x[r],2)
```

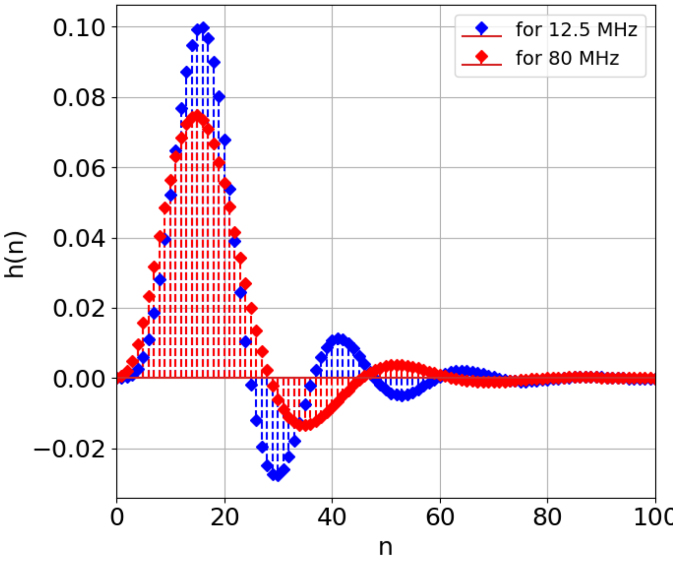

Figure 5.9: Impulse response function of IIR filter. *Blue curve*: 12.5 MHz original sampling frequency, $L_{up} = 8$, cutoff frequency 4.5 MHz, order 6. *Red curve*: 80 MHz original sampling frequency, $L_{up} = 4$, cutoff frequency 10 MHz, order 4

```
    vert = parable_vertex(p)
    y = p[0]*r**2 + p[1]*r + p[2]
    #print('imax ' ,imax, x[imax])
    return (vert,p,r,x[imax])
```

Code Listing 5.2: Function `fitquadratico`

5.5.5 Implementation of real-time algorithm

To speed up the analysis and the prototyping, the previous codes have been written in Python. Then, in the software for microcontroller, these codes have been translated in C++, because this language is one of the most efficient and performing. It has been implemented the same function seen before, from the Python class `InterpFilter`. Despite with Python is possible to use the numerical library NumPy, for the C++ code the filter function has been translated, using the formula 5.10. This because the functions to be implemented on the microcontroller do not take advantage of already provided basic libraries. The code is reported in the Code Listing5.3.

```
void FilterOnce(double* pbIn, int Np, double* pA, int Q, double* pB, int P,
    double* pbOut) {
    /*

        Filtering  updating memory states

      INPUT

        pbIn:           input vector to be filtered
        Np:             number of point to be filtered
        pA, pB:         filter coefficients
        Q,P:            number of feedback (a) and feedforward (b) coefficients
```

```

      OUTPUT

        pbOut:          output filtered vector
    */

    double* pX = new double[nParB];
    double* pY = new double[nParA];

    for (int i = 0; i < nParA; i++) pY[i] = 0;
    for (int i = 0; i < nParB; i++) pX[i] = 0;

    int     i, j;
    double  yn;

    for (i = 0; i < Np; i++)
    {
        for (j = (nParB - 1); j > 0; j--)
            pX[j] = pX[j - 1]; // Shift register for X

        pX[0] = pbIn[i]; // Update new state

        yn = 0.0;

        for (j = 0; j < nParB; j++)
        {
            yn = yn + pB[j] * pX[j];
        }

        for (j = 0; j < (nParA - 1); j++)
            yn = yn - pA[j + 1] * pY[j]; // assumes pA[0]=1; pA[1]*pY[0]=pA[1]*y
    (n-1)

        for (j = (nParA - 2); j > 0; j--)
            pY[j] = pY[j - 1]; // Shift register for Y. pY[nParA-1]*pA[0]=yn*1

        pY[0] = yn; //Update y(n-1) for next loop

        pbOut[i] = yn;
    }

    delete[] pX;

    delete[] pY;
}
```

Code Listing 5.3: Function `FilterOnce`.

5.6 ULTRASONIC TEMPERATURE MEASUREMENTS ANALYSIS

From a theoretical point of view, it has been observed that the relation with the elastic constants and the temperature is approximatively linear for temperature below 500 °C. This is traduced in the relation with the acoustic speed, sinche the velocity depends on the elastic constant. In that way, the linear approximation is

$$\Delta t = mT + q, \tag{5.14}$$

with m representing the angular coefficient in the plane $(T, \Delta t)$. For the cases of planar copper slab with different thickness, the estimated angular coefficient m change significantly. The explanation is that its value depends on the thickness L_{Cu} of the copper. This happens because m represents the increment of TOF respect to a variation in temperature, *i.e.*

$$m = \frac{\delta(\Delta t)}{\delta T}. \tag{5.15}$$

The variation at numerator depends on the thickness under consideration: if we consider the same temperature variation for different specimen, thicker slabs will undergo to a greater variation on the time-of-flight (TOF) Δt, expressed by $\delta(\Delta t)$, since ultrasound beam has to travel a longer distance and this influence the magnitude in numerator of the latter equation.

The purpose of this Section is to show how the interpolation technique that performs signal reconstruction is suitable for estimating the time of flight (TOF) of ultrasound under varying sample temperature conditions. Then, from this, the velocity is computed with the classical formula 2.77 in Section 2.6. As explained at the beginning in the Introduction of this paper, the goal is to derive a temperature measurement from these sets of measurements, but this can be done if the measurement technique proves to be reliable. One way is to test, by acquiring on multiple copper samples taken from used ingot moulds, that the estimated time-of-flight as temperature changes reproduces a repetitive pattern. In literature, several techniques, in addition to time-of-flight estimation, have been investigated; for example, in **??** the method of measuring time-of-flight by precise phase-shift measurements is used. In practice it is measured how the phase of steady state frequency ultrasonic wave changes between the transmitted and received signal respect to the temperature. However, this practice is useful for measuring temperature in the core of certain objects where the simpler pulse-echo common method would not work because of the strong attenuation of the medium. In our case, this technique is effective because the thickness we consider is usually of the order of $1 - 2\,\mathrm{cm}$.

Regarding the procedure to make measurements in the heated copper, two approaches were followed. The first in chronological order involved the preparation of a setup consisting of a thermal water bath where the copper plate is immersed and the temperature is adjustable by thermostat, which allows slow scanning in temperature up to about 60°C. The second approach, used later to make measurements at higher temperatures, involved the use of a gas bunsen heater, where the copper plate was directly heated. This approach, although rudimentary, yielded good results. Mainly the analyses concerned how to determine by linear regression the value of angular coefficient and intercept of the model. The following discussion refers mainly to two sources [**book:round**] and [14].

5.6.1 Algorithm development

In practice, signals in the pulse-echo configuration are recorded during the acquisition phase, and then the time-of-flight measurement is obtained from the difference of the absolute times of the individual echoes. The procedure for extracting this information involves interpolation analysis. Libraries for make elaboration on the collected data were written in Python, because it was necessary to collect numerous measurement campaigns in each temperature scan made several times for different copper samples. The general flow for obtaining flight time estimates is as follows:

- Data pre processing:
  - Band-pass filter application, necessary for plant-acquired data, for the higher signal noise than those collected in laboratory;
  - Inversion of the signal if higher peak is downside;
  - Subtraction of the mean signal;
- Interpolation procedure;
- Fit procedure;
- Saving of the data;

5.6.2 Regression coefficients

The linear regression formula in this case assume the following structure.

$$y_i = \beta_0 + \beta_1 x_i. \tag{5.16}$$

Reformulating the previous relation in terms of the quantities under study in our experiments, the only one independent variable or *predictor* is the temperature, and the *response* corresponds to the velocity v. The vector of the parameters $\boldsymbol{\beta}$ has dimensions 2, since for linear regression there are only β_0 and β_1. From now, it will be convenient to perform the substitution with the used physical quantities, to become familiar with the notation used in the following.

$$\beta_0 = q_v \qquad \beta_1 = m_v \tag{5.17}$$

$$x_i = T_i \qquad y_i = v_i \tag{5.18}$$

that can be rewritten in matrix notation as

$$\mathbf{v} = \begin{bmatrix} v_1 \\ v_2 \\ \vdots \\ v_n \end{bmatrix} \qquad \mathbf{T} = \begin{bmatrix} 1 & T_1 \\ 1 & T_2 \\ \vdots & \vdots \\ 1 & T_n \end{bmatrix} \qquad \boldsymbol{\beta} = \begin{bmatrix} q_v \\ m_v \end{bmatrix} \qquad \boldsymbol{\varepsilon} = \begin{bmatrix} \varepsilon_1 \\ \varepsilon_2 \\ \vdots \\ \varepsilon_n \end{bmatrix} \tag{5.19}$$

In this situation, the Eq.**??** for the *confidence interval* CL = $1 - \alpha$ reduces to

$$v(T) \in \hat{v}(\mathbf{T}) \pm t_{1-\alpha/2}\hat{\sigma}(\hat{v}(T)). \tag{5.20}$$

with the estimate for the variance equal to

$$\hat{\sigma}^2(v(T)) = \frac{\sigma^2}{n}\left[1 + \frac{(T-\bar{T})^2}{\bar{s}_T^2}\right]. \tag{5.21}$$

$\bar{s}_T^2$ is the center of gravity of data, *i.e.* $\bar{s}_T^2 = \frac{1}{n}\sum_{i=1}^{n}(T_i - \bar{T})^2$. From this, we observe that if the predictor are chosen in a range outside the observed ones, *i.e.* we are going to do an extrapolation, the error increases since the numerator in the square parentheses increases. For this reason we have tried to design experiments where the temperature ranges can be extended as larger as possible, covering the widest physical interval of temperatures. Now, we will analyse the hypotheses tests which are helpful in measuring the usefulness of the model.

5.6.3 Test on the single regression coefficient

We are now interested in testing hypothesis on the individual regression coefficient, for example to decide if a model is most suitable with an additional variable or perhaps with the deletion of one or more. The hypothesis for testing the significance of any individual regression coefficient are

$$H_0 : \beta_j = 0 \tag{5.22}$$

$$H_1 : \beta_j \neq 0. \tag{5.23}$$

If $H_0 : \beta_j = 0$ is not rejected, then this indicates that x_j can be deleted from the model. The test statistic is

$$T = \frac{\hat{\beta}_j}{\sqrt{(\mathbf{X}^T W \mathbf{X})^{-1}_{jj}}} \tag{5.24}$$

$$= \frac{\hat{\beta}_j}{s(\hat{\beta}_j)} \tag{5.25}$$

and the null hypothesis is rejected if $T > t_{1-\alpha/2,n-k-1}$, and the $\hat{\beta}_j$ has an explanatory power, *i.e.* it is significantly different from 0. High values of T indicate a relative small error and thus the importance of the parameters. The denominator of the previous expression is the *standard error* of the regression coefficient $\hat{\beta}_j$. These two are the hypothesis tests that have been applied to the analyses fo the data acquired by the experiments that we are going to see.

5.6.4 Outliers detection

Before starting with already seen analyses, it is a common procedure to perform an outliers research. The problem of outliers detection is quite important since considering or not these value in the regression model could produce very different results. An interesting way for looking for they is to compute the *standardized residual*:

$$z_i = \frac{y_i - \hat{y}_i}{\hat{\sigma}} \tag{5.26}$$

$$= \frac{e_i}{\hat{\sigma}}. \tag{5.27}$$

These standardized residuals have zero mean and approximately unit variance; so, they are useful in looking for outliers. In practise, most of these standardized results should lie in the interval $-3 \leq z_i \leq 3$ and any observation with a value outside this region is potentially unusual and might be carefully analysed.

5.7 MEASUREMENT TECHNIQUE FOR HIGH TEMPERATURE TESTS

The main problem of the previous setup regards the high temperatures which Rexolite has to face. From datasheet [18], the recommended operational temperature has to be maintained under the *transition glass temperature* T_g, *i.e.* the temperature at which the amorphous polymer structure turn viscous liquid or in a rubbery state. In this region the physical properties changes dramatically, for example hardness or elasticity. It is therefore important to maintain the maximum heating temperature for Rexolite far below this critical value. The expedient we realized in laboratory has been to re-design in a particular fashion the Rexolite piece, in order to provide an internal structure of grooves to allow water circulation. In this way, the water flow entering on one side cools and keeps the temperature down, even though it remains in contact with the heating surface. The Rexolite piece is depicted in Fig.5.10, where, from different views, we observe the presence of the internal groove where the water circulates. The process of drilling has been performed by a CNC machine; in particular, we designed the piece to meet these specifications:

1. Drilled holes for support have been designed like for the previous piece, to fix it to the specimen after having applied the high temperature ultrasonic couplant.
2. Another drilled hole to insert the K-type thermocouple (see Fig.5.10) (c), to monitor the temperature increase near the area of the ultrasounds;
3. The contact area is only the portion where is located the probes and the two lateral screws. In this way it cannot be heat transfer by conduction and the amount of heat to the piece is reduced. This area is highlighted by the red dashed lines;
4. Again from Fig.5.10 (c), the water channel is visible in the region around the probes (view from the downside in the figure).

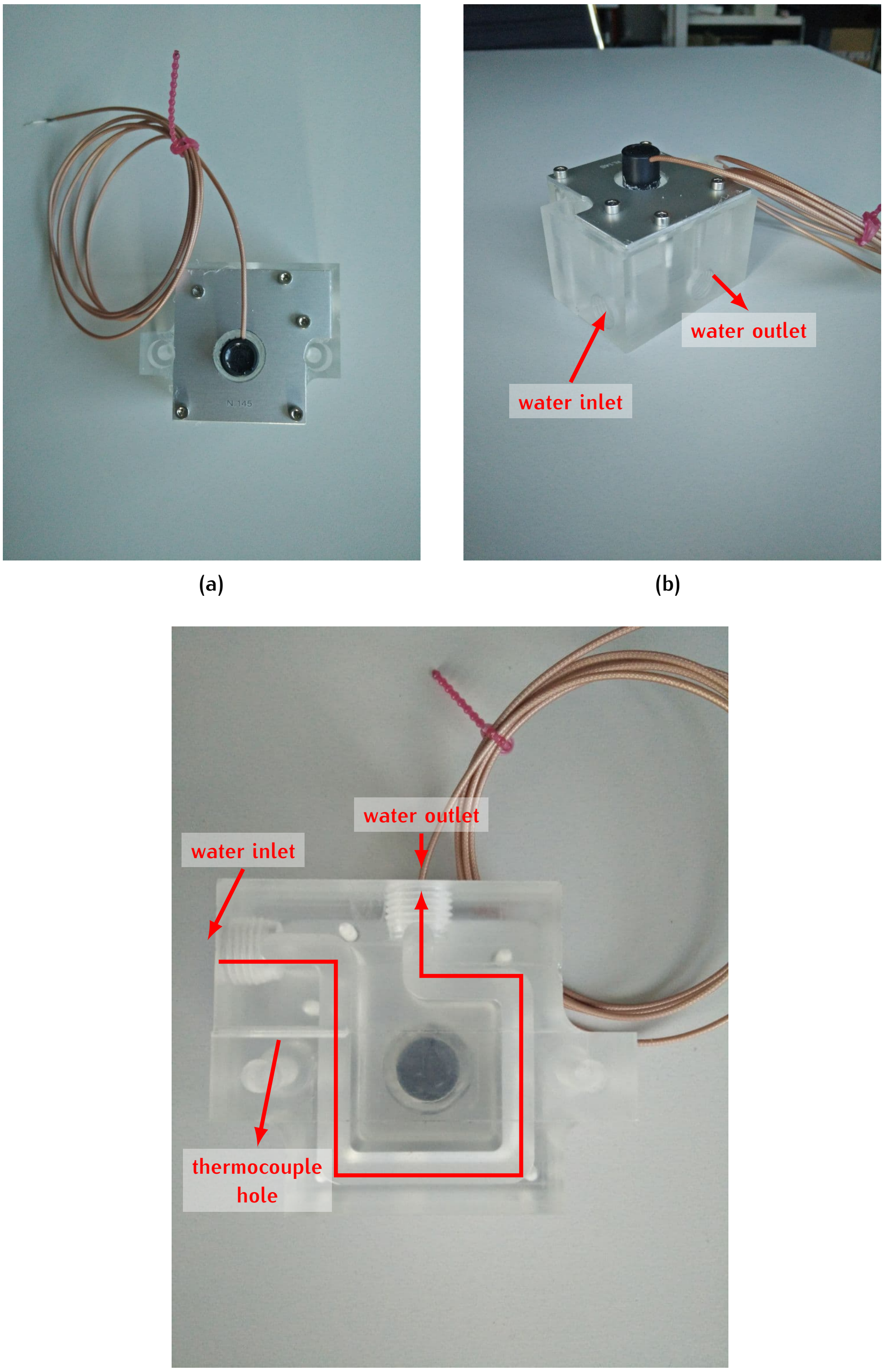

(a)

(b)

(c)

Figure 5.10: CNC Rexolite piece with drilled cavity for water cooling process during measurements. (a) Upper view; (b) Lateral view where the inlet and outlet for the water channel are visible.

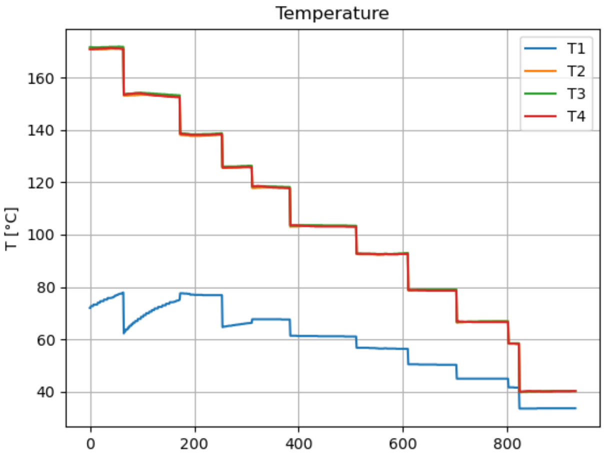

(a)

Figure 5.11: The temperature trens for the 4 thermocouples during an experimental campaign. $T2$, $T3$, $T4$, are the temperature sensor in the copper, while $T1$ is the one in the Rexolite®.

5. The probes is fixed with an epoxy resin;

This piece is shown in Fig.5.12 above the copper specimen, with the tube connections and the thermocouples fixed in the drilled holes. Three thermocouple are positioned in the drilled holes in copper, while the last is used to monitor the temperature at the lower edge of the Rexolite, nearest the interface. The behaviour of temperatures can be compared in Fig.5.11, where the Rexolite sensor show how the maximum detected temperature near the internal interface remains far below the T_g recommended limit. The trend of other three temperature is shown: the discrete steps occur since the data acquisition is active only when requested, that is, when the temperature is maintained constant and acquisition at this value can be done. The complete experimental apparatus with the elaborated Rexolite® piece is depicted in Fig.5.12. Water circulation is maintained by the closed-circuit made of these elements: the pump, the water reservoir, the pipes and the Rexolite.

In this way, we obtain the clear advantages respect the previous measurements:

- Fixed position on the copper specimen for overall duration of test, with the possibility to repeat in the same geometric condition the test;
- Extended temperature range of measurement.

5.8 CONCLUSIONS

This Chapter have shown all the necessary methods used to calculate in the best way the time of flight between two successive measurements of echoes in copper. The construction procedure made by the interpolator filter, has been applied in the real-time algorithms of the software for direct measurement on the acquired signal. Regarding the laboratory testing part, multiple

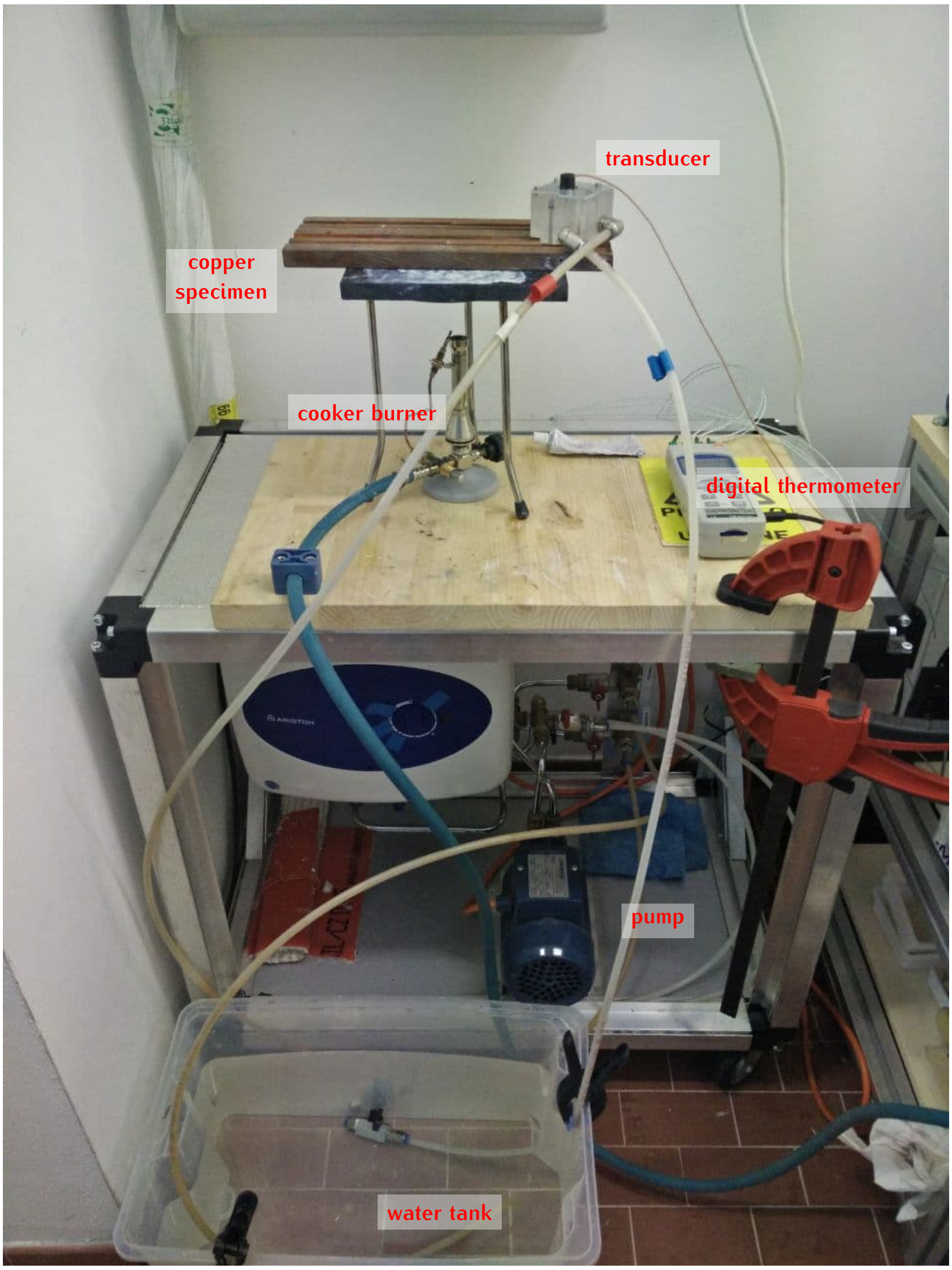

(a)

Figure 5.12: Experimental setup with the new designed Rexolite piece.

attempts have been made to reach the point of a measurement at high temperatures ($\geq 150\,^{\circ}\mathrm{C}$) that was satisfactory. The next Chapter will look at the results of these measurement campaigns.

6 ULTRASONIC TEMPERATURE MEASUREMENTS AND RESULTS

6.1 OVERVIEW

In this Chapter the results of the applied interpolation technique and of the tests performed in temperature variation are shown. The results are presented in two distincted sections: in the first the interpolation procedure is applied to the recorded signal to demonstrate the validity of the procedure. The interpolation tecnique has been applied both in the 12.5 MHz recorded sample and in the 80 MHz. This because the former was the first experimental attempt for the custom electronics, while the latter has been the next step in the enhancements of the sensor. Therefore, it is very interesting to compare the different results before and due to the improvement of the increased sampling rate. In the second part, it will be shown how the interpolation works when the aim is to measure the TOF due to the differences in temperature. The tests has been performed with the setups described in the Chapter 4.

6.2 RESULTS OF THE INTERPOLATION PROCESSING

6.2.1 12.5 MHz sampling frequency

The first results are referred to the interpolation technique applied to 12.5 MHz sampled signals. The output set of filter parameters has been obtained by testing different combinations and evaluating the best result in terms of precision of the measure. The time width has been calculated as a difference between the subsequent peaks S1 and S2 from the original signal, obtaining a discretization of $t_{s,old}$. In the process which is under consideration the time width changes slightly, but its entity is under the resolution of the only raw signal. Using the upsample factors $L_{up} = 8$, the Δt distribution shown in Fig. 6.1(a),(b) was recovered. The red points represent the oscillation of Δt from successive acquired signals. The corresponding dispersion is visualized in the histogram (red) , along with the blue one which represent the dispersion of the upsampled Δt. The improvement in the discretization for the quantity is well determined, indeed the standard deviation is reduce by a factor $5.86/3.44 = 1.70$. For the case of a lower upsample factor, the final results are quite similar: the differences are negligible and the gain of using a higher upsample factor isn't paid. Eventually, with the upsample factor $L_{up} = 12$ no significant improvements are obtained. Since the standard deviation for the upsample factors (blue) is strictly smaller than the two previous case, the improvements with the least square fit is negligible. One can just said that increasing the upsample factor and performing the least square fit around the maximum does not improve the resolution at all, and that the

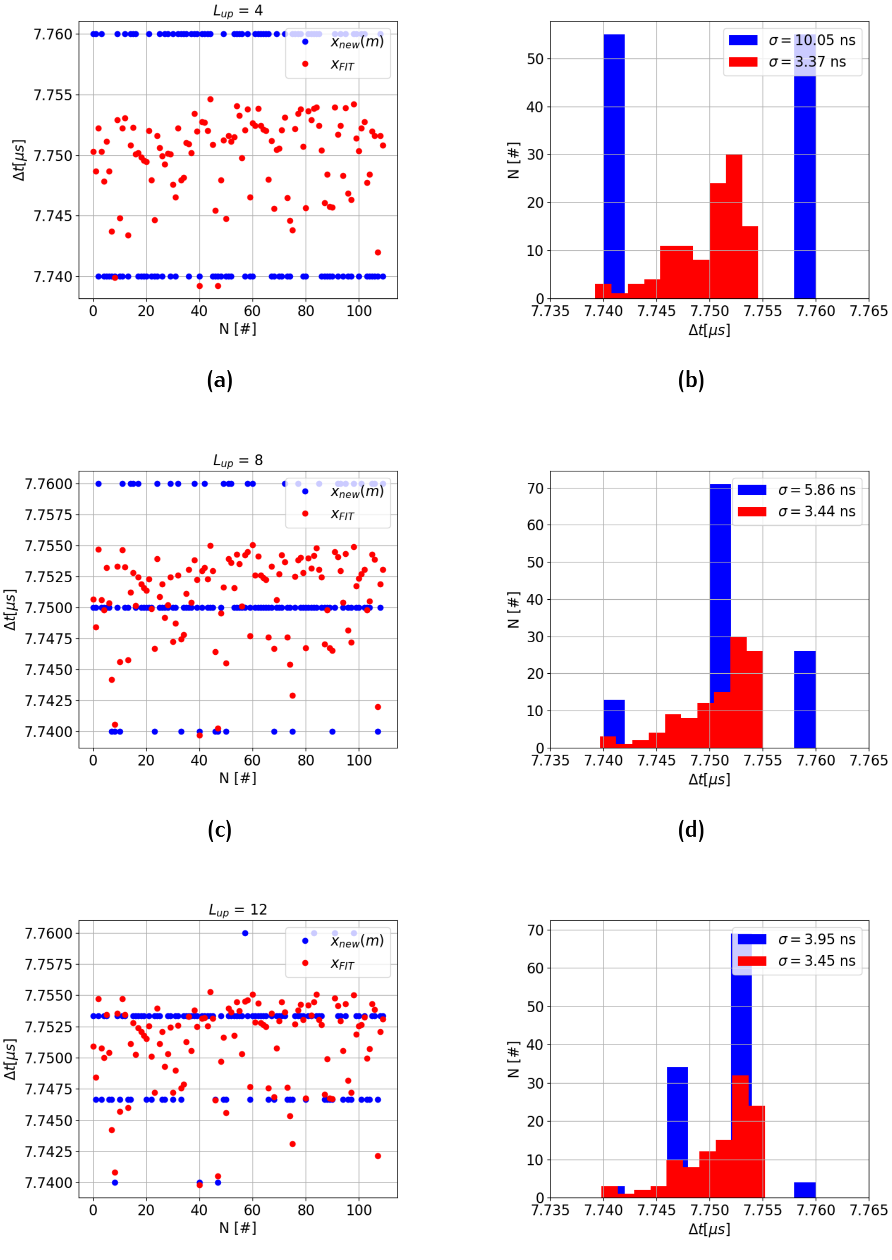

(a)

(b)

(c)

(d)

(e)

(f)

Figure 6.1: Results with different upsample factor L_{up}. (a)-(c)-(e) Dispersion of Δt calculated for the upsampled signal (*blue*) and the regression made on the same upsampled signal (*red*), over the time. (b)-(d)-(f) The histograms of the previous points. The difference in the dispesion of the regression point is quite similar through the entire range of the upsampling factor, meaning that the procedure is quite stable and reliable.

distribution of the red bins is at some point completely random. But notice again Fig. 6.1: when the L_{up} factor increases, the blue bins distribution tends to be like the red one, which in all three cases is quite similar. Indeed, instead to perform interpolation with a high factor, which could be quite computationally expensive and useless since the majority of the multiplication between filter coefficients and signal sample are zero, it can be chosen to perform interpolation with a lower upsample factor, plus LS fit. Now let's analyse the contribution of another filter parameter, the cut-off frequency of the low-pass filter. In Fig. 6.2 it can noticed the influence on the final dispersion of the Δt. The upsample factor remains always the same, *i. e.* $L_{up} = 8$, the modification can only depends on the cut-off parameter. Absolute values of σ_{up} and σ_{fit} increase, but the worst thing is the introduction of some bad Δt , very far from the mean values of the samples (Fig. 6.2(e)-(f)). The effect of using different filter parameters are shown also in Fig. 6.3, where the upsampled signals are depicted along with the original ones and, in the right side, their corresponding magnitude frequency response. As previously seen, the zero-stuffing procedure in the signal time-axis has the effect to create multiple *images* of the discrete spectra, repeating at each multiple of the old sampling frequency $f_{s,old}$ (see again Fig. 5.5 (d)). Those images are *real* and, using the low pass filter, the frequencies in the interval between the highest passband signal one ($\frac{f_{s,old}}{2}$) and the new $f_{s,new}$ can be reduced. These components modify the final shape of the reconstructed signal, and also the final outcome of the Δt quantity. So, due to the initial sampling frequency $f_s = 12.5\,\text{MHz}$, in order to cancel out the replicates, it's better to chose a cut-off frequency slightly low the old half sampling frequency and this has been done by a trial-and-error approach the value of 4.5 MHz. Indeed, it can observed from right picture in Fig. 6.3 three different magnitude frequency response, using three different digital filters whose the only difference is the cutoff. In Fig. 6.3 (b), the sharper roll-off on the higher frequency side cuts the blue original response, producing the corresponding red signal in the left (a). In the red one signal high frequencies does not appear, and this causes a smoothed version of the original counterpart. Conversely, when the chosen cutoff increases, for example up to 6 MHz near the *Nyquist frequency* as in Fig. 6.3(d), enter in the magnitude response frequency components due to the spectral images caused by the interpolation process. This effect is clearly more evident in the last picture, Fig. 6.3 (f), when the $f_{cutoff} = 8\,\text{MHz}$ allows the noticeable presence of the second peak in the red circle. This is reflected in the outcome signal in the time domain, always in red, reported in (e): it's shape completely differs from the original counterpart, moreover, instead of being attenuated, the outcome has a more prominent peak and unphysical oscillation can be observed.

6.2.2 80 MHz sampling frequency

The last results refer to the acquired signals at the 80 MHz sampling rate. Despite the idea of interpolation comes into the field because the original available rate was 12.5 MHz, it has been decided to apply this technique to these signals. Since the logical steps are about the same, the results are

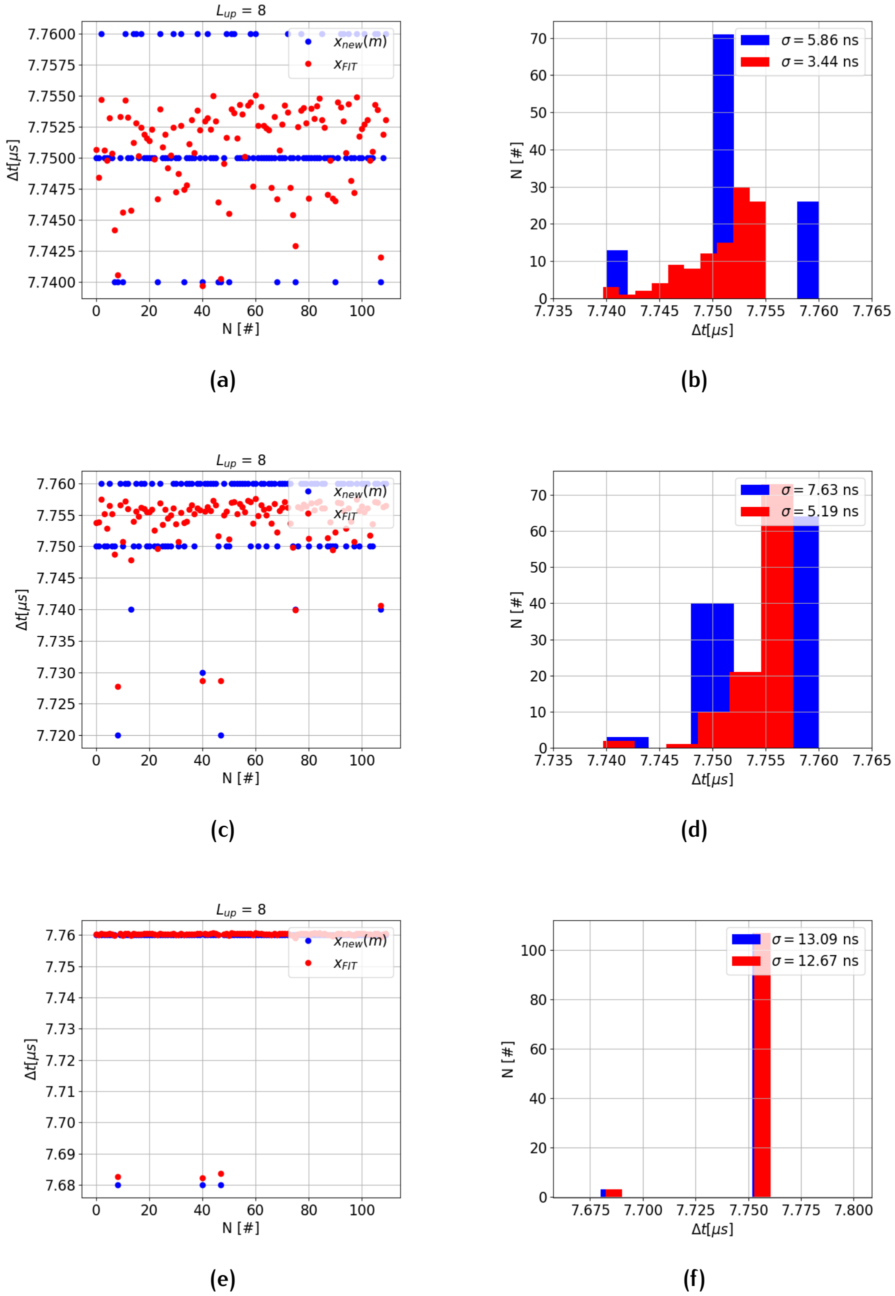

Figure 6.2: Results with different filter cutoff. (a)-(c)-(e) Dispersion of Δt calculated for the upsampled signal (*blue*) and the regression made on the same upsampled signal (*red*), over the time. Filter cutoff : (a) 4.5 MHz, (c) 6 MHz,(e) 8 MHz. (b)-(d)-(f) The histogram of the corresponding dispersion diagrams. At the same L_{up} value, the filter cutoff gretly influences the σ both for the upsamplad and the fitted points.

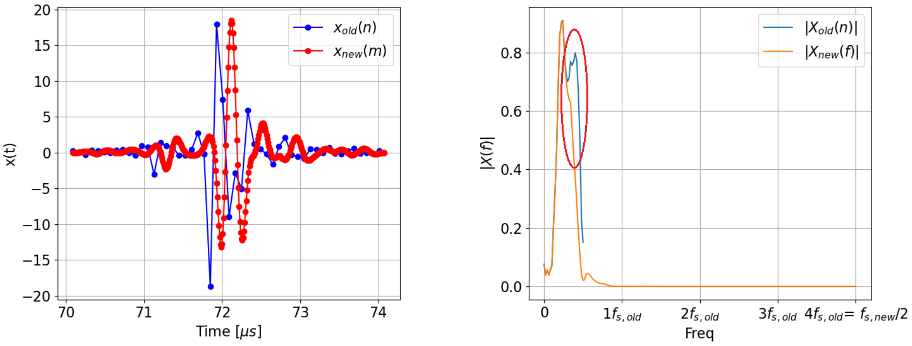

(a) *Filter cut-off at* 4.5 MHz

(b)

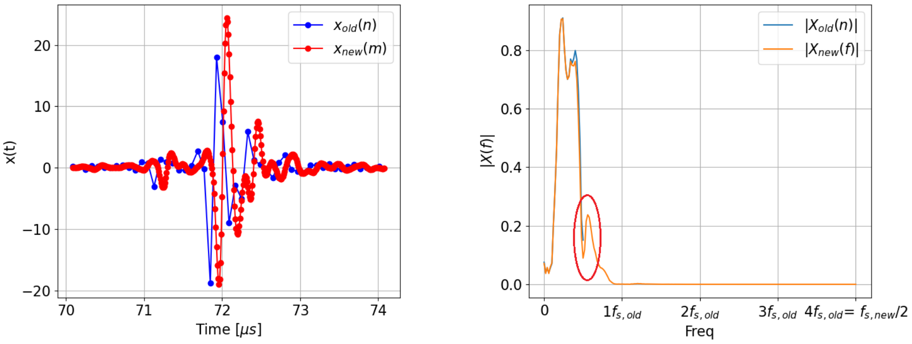

(c) *Filter cut-off at* 6 MHz

(d)

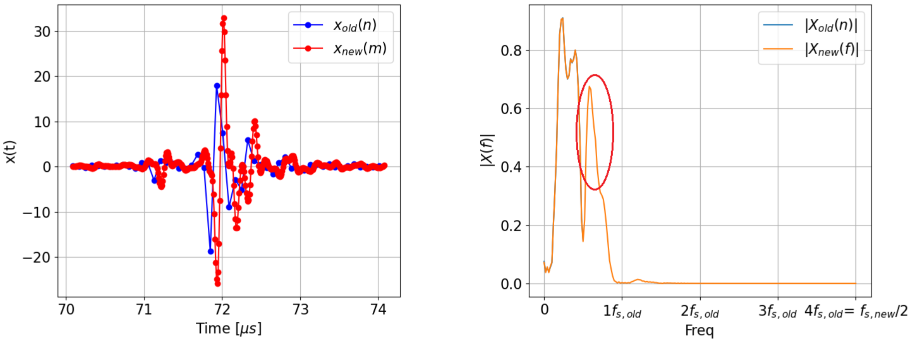

(e) *Filter cut-off at* 8 MHz

(f)

Figure 6.3: Results in terms of shape recostruction of the signal. (a)-(c)-(e) Original first echo signal (*blue*) and interpolated signal (*red*) at (a)-4.5 MHz, (c)-6 MHz, (e)-8 MHz cutoff frequency of the filter. (b)-(d)-(f) Magnitude frequency response at the corresponding 4.5 MHz, 6 MHz and 8 MHz. In the red circles the region of spourious residual frequencies that alter the reconstructed shape in red. In the last (f) the highest frequency peak is responsible of the noiser part of the signal.

Sampling frequency $f_{s,old}$ (MHz)	Central frequency $\simeq f_c$ (MHz)	Frequency ratio $\simeq \frac{f_s}{f_c}$	Upsample factor L_{up}	Cutoff frequency f_{cutoff} (MHz)	$\sigma(\Delta t)$ (ns)
12.5	3.0	4.2	4	4.5	3.37
12.5	3.0	4.2	8	4.5	3.44
				6	5.19
				8	12.67
12.5	3.0	4.2	12	4.5	3.45
80	3.0	26.7	4	10.0	3.34
				5.0	3.17

Table 6.1: Standard deviation of Δt obtained with different parameters of the interpolator low-pass filter

directly shown in Fig. 6.4. The most important thing to notice, is the comparison between the new sampling rate and the main frequency component which characterize the wavelet:

$$\frac{f_{s,new}}{f_c} = \frac{80\,\text{MHz}}{3.5\,\text{MHz}} \simeq 26.7. \tag{6.1}$$

This ratio is higher than the previous one, and it's clear that the final results will be more accurate, in particular the shape reconstruction problem. At this point, since the original bandwidth remain practically the same (compare the response in Fig. 6.4(b) respect to Fig. 5.5(b)), using an initial sampling rate of 80 MHz just satisfies the *Nyquist criterion* entirely. However, an interpolation factor of $L_{up} = 4$ produce the red signal (e), and the corresponding frequency response contains all the relevant information if a cutoff of 10 MHz (f) is chosen. Indeed, with this L_{up} the real images are placed at multiples of 80 MHz and so they are completely attenuated. The final result is highly accurate and similar to the original shape. Eventually, the Δt distribution of the LS fit is not quite different than the upsampled one. In Tab. 6.1 all the results obtained in this study are reported.

6.3 RESULTS OF TOF MEASUREMENTS BY INTERPOLATION PROCESS

6.3.1 Measurements with EUROSONIC-Mistras setup

To increase the accuracy of the measurement, tests with the EUROSONIC-Mistras UTC110 electronic card have been performed, using the digital thermometre to acquire signals and temperature togheter. The temperature acquisition has been integrated in the GUI software; in this way, a real-time trend is visible on the screen of the PC used for controlling the card and set-

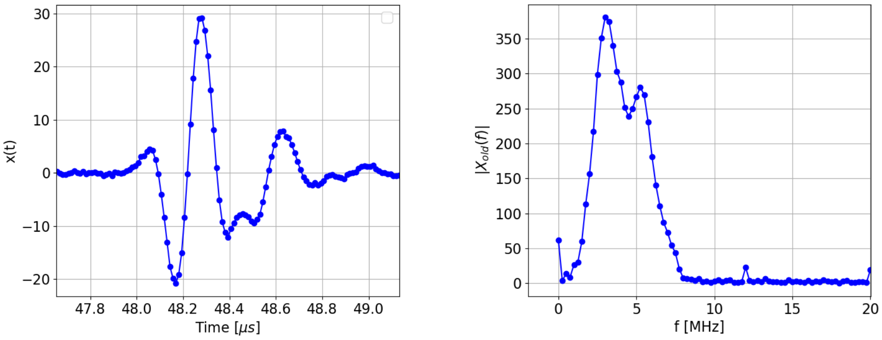

(a) Original 80 MHz sampling. **(b)** DFT of original signal (a).

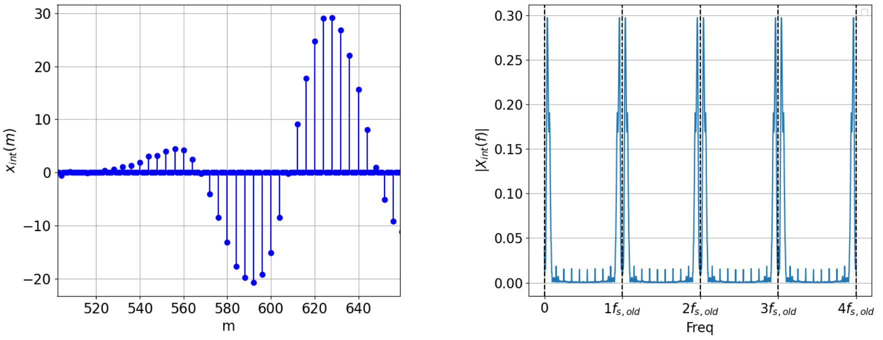

(c) Zero-stuffing procedure. **(d)** Aliased spectrum of (c).

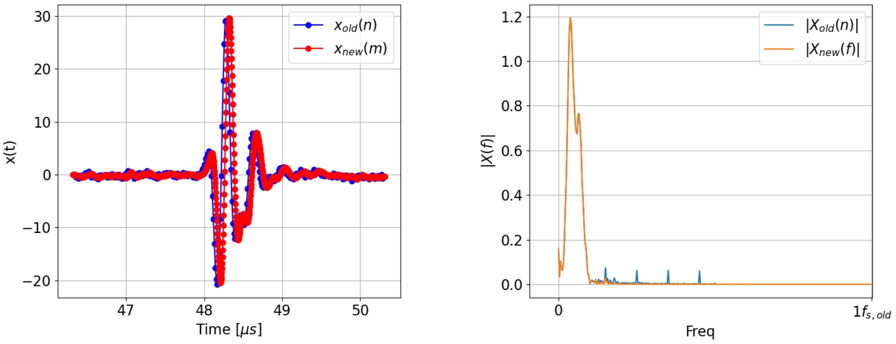

(e) Superposition of original and upsampled signals. **(f)** Final spectrum of $x_{new}(f)$.

Figure 6.4: Interpolation technique application on 80 MHz signal. The reconstructed signal (*red*) is very similar to the raw one (*blue*). This means that the reconstructed frequency component is almost reproduced also in the upsampled form.

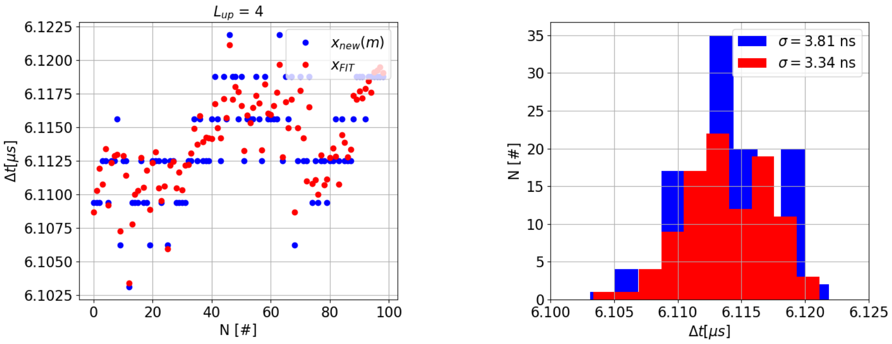

(a)

(b)

Figure 6.5: Δt dispersion on the interpolated 80 MHz sampled signal.

ting the parameters. The setup under study is shown in Fig.6.6 with these dimensions:

- $L_{Rex} = 38\,\text{mm}$;
- $L_W = 16\,\text{mm}$;
- $L_{Cu} = 16.48\,\text{mm}$;

In Fig.6.7 (a), (b) the linear outcome of the continuous acquisition during the heating process is shown. The *blue* point represents the Δt calculated as the difference between the raw signal, this time sampled at 100 MHz, with the observed discretization is 0.01 μs. In *red* are shown the differences between the interpolated points: these ones are obtained via upsample of the underlying raw signal and interpolation around the maximum with an upsample factor $L_{up} = 4$. The Fig.6.7 (c) depicts the same data as the previous two figures, but with the temperature behaviour. Even with this higher sample rate (100 MHz) the interpolation technique guarantees the god identification of the linear behaviour caused by the temperature variation. In the registered 30 °C temperature range (from 25 °C to 55 °C), an overall variation of at most 30 ns appears: if one had to consider only the sampled signals at 100 MHz, *i.e.* a minimum variation of 10 ns between each sample, the precision of this measurement would be quite insufficient to detect variations caused by small temperature change. An interesting view is the dispersion of the measurements at about the same temperature, take during the test. With this, the need to observe the relative dispersion that occurs at different temperatures, to see if the measurement is less precise raising the temperature. In Fig.6.8 each graph shows the dispersion near the indicated temperature. The histogram are realized taking about hundred points near the temperature value, and the σ is calculated. On the overall temperature extension, the dispersion remains quite similar: the overall noise measurement remains constant.

Tha last comparison regards the acoustic velocity in function of the temperature. To compare the results with the custom hardware ultrasonic system, the P-wave velocity of this measurement has to be measured, Fig.6.6 (c).

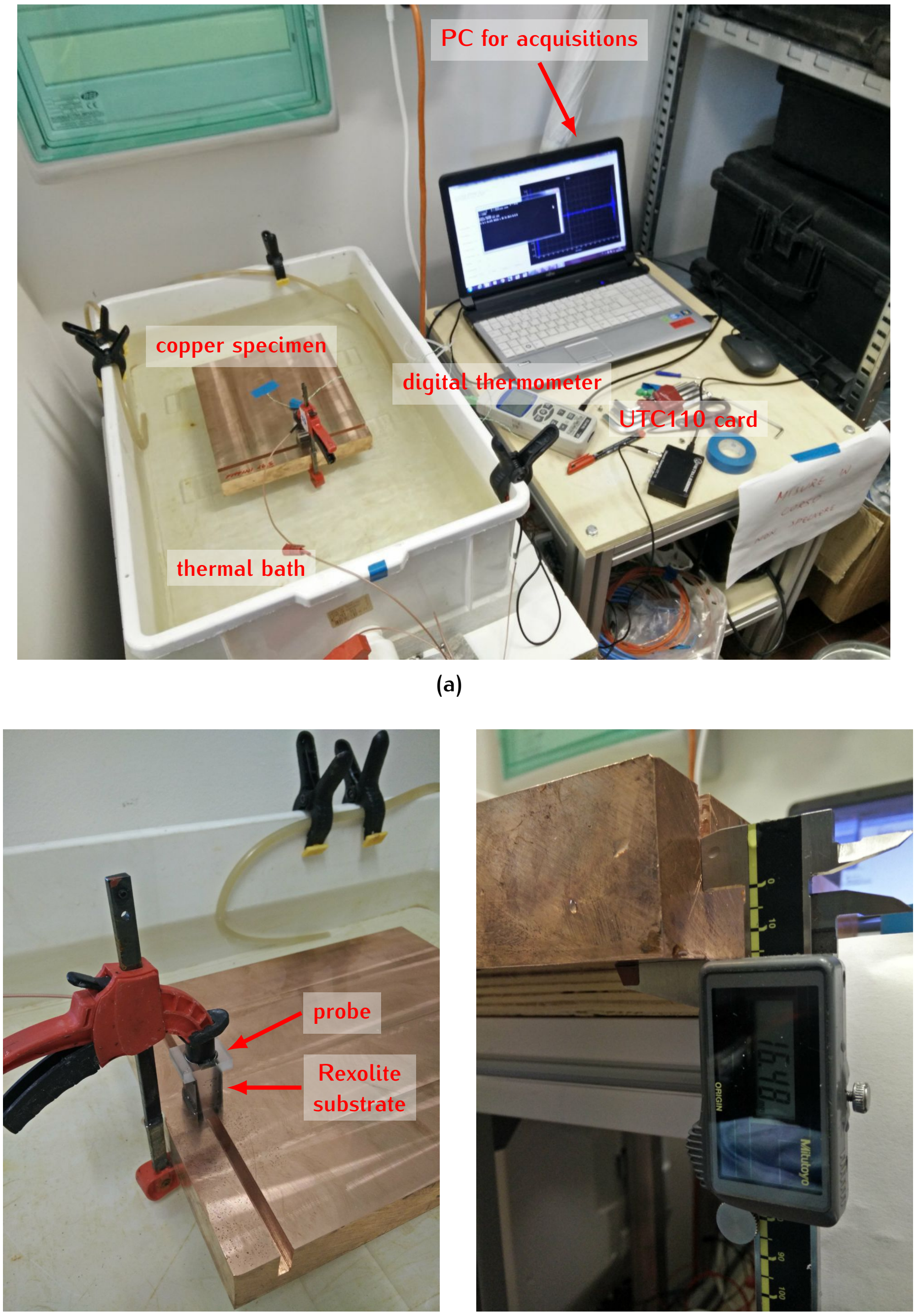

(a)

(b)

(c)

Figure 6.6: Experimental setup with the Eurosonic-MISTRAS® hardware, in planar copper slab with water channel.*Above*: the UMS setup with the UT card, digital thermometer and PC. *Below*: the probe position and the thickness measurement.

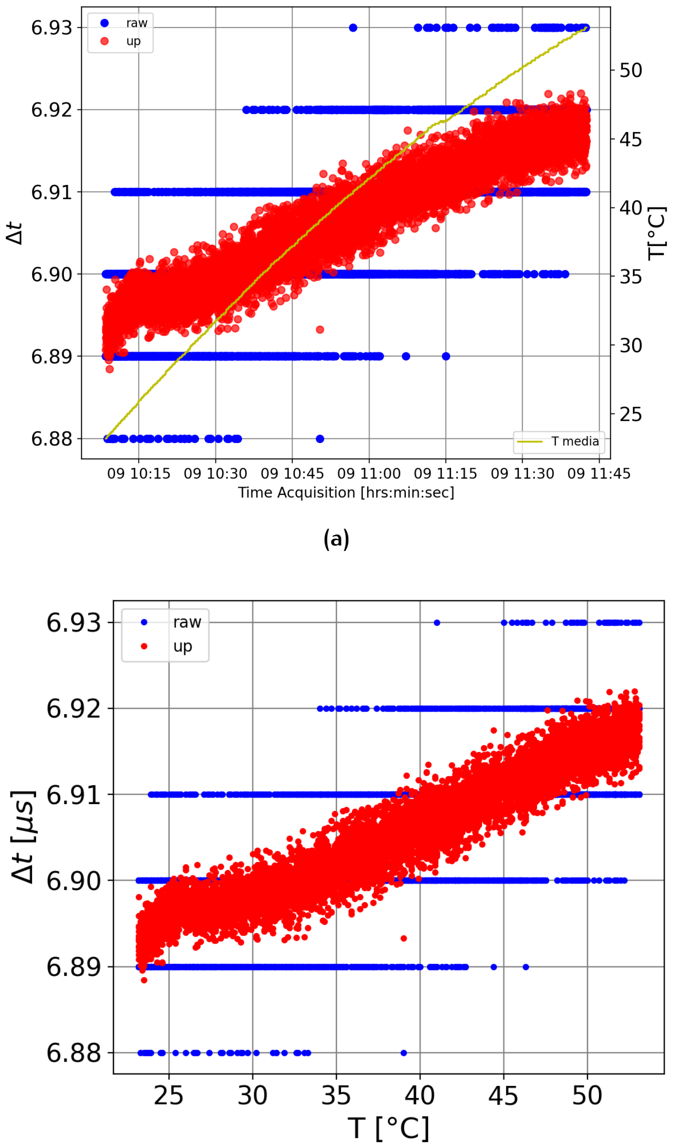

(a)

(b)

Figure 6.7: Temperature test with Eurosonic-MISTRAS in copper thickness of 16.48 mm. Each red and blue dot represent a Δt acquisition. The difference is that the blue is the TOF calculated by difference of the two raw maxima of the echo, while the red one comes from the output of the interpolation. *Above*: the acqusition trend is reported in function of time, the temperature trend in reported in *yellow*. *Below*: Δt in function of T.

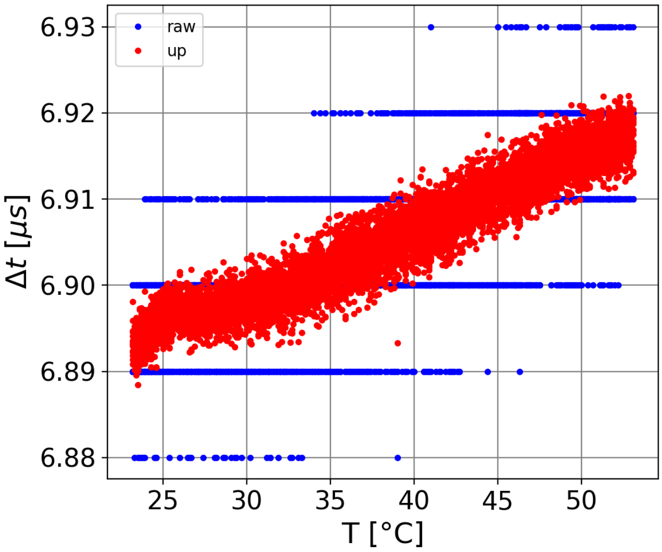

Figure 6.8: First test in heating with Eurosonic-MISTRAS in 16.48 mm. *Above*: Δt trend in temperature. *Below*: Δt dispersions for some temperatures.

6.3.2 Tests for repeatability

These tests in temperature variation have been repeated several time in order to see how these measurements are repeatable. In Fig.6.9 are reported the second test during the heating phase, along with the dispersion analyses (below figures).

In the temperature tests, both the heating and the cooling phase have been of the thermal bath have been used. In this way, since the cooling has an negative exponential decrease (see Fig.6.10) of the temperature, the cooling phase has been longer. The same replica of the test is visualized in Fig.6.11.The test has been realize in the same temperature interval as before, to compare the dispersion of the Δt for the two experiments. With detailed comparison is in Tab.6.2, where the $\sigma_{\Delta t}$ are shown at the same temperature evaluations.

On the other hands, the comparison among these tests could be done by plotting the overlapped behaviour of the velocities as functions of temperatures. In these case, the previous tests are depicted in Fig.6.12 all overlapped, with different colours. Both the *heating* and the *cooling* phases are presents. The heating experiments, signed by *risc* tag, have similar behaviour at the starting temperatures, with a slightly deformation from the expected linear behaviour. In that region, between the 25 °C and 30 °C, since the heating process is at the beginning, the sudden temperature variations induced by the boiler might increase the noise and affect the final outcome of the measurements. This is of course visible in Fig.6.11 and the $\sigma_{\Delta t}$ values for the shown temperatures,as already recap in Tab.6.2. The final result is the stability obtained t by introduction of the upsample plus regression technique. This fact is evident in Fig.6.12 where the overall dispersion of the below plot (interpolated values) is compared to those above (raw values). Superposition of different tests shown in the same figure, reveals the repeatability of these measurement and the possibility to evaluate in a quantitative and

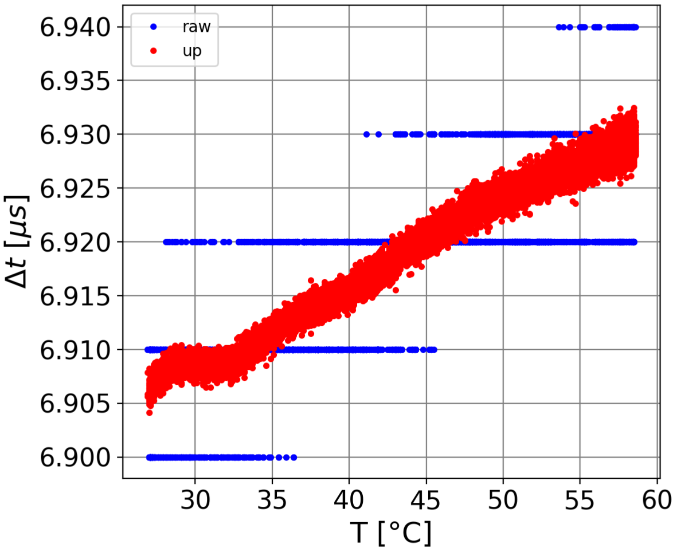

Figure 6.9: Second test in heating with Eurosonic-MISTRAS in 16.48 mm. *Above*: Δt trend in temperature. *Below*: Δt dispersions for some temperatures.

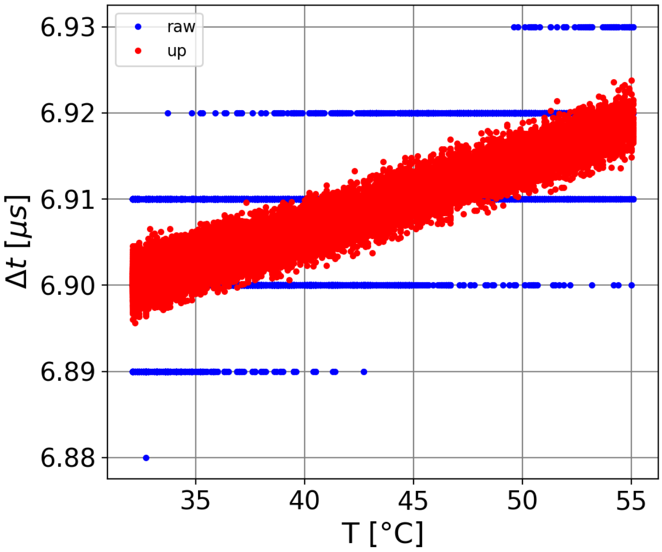

Figure 6.10: First test in cooling with Eurosonic-MISTRAS in 16.48 mm. *Above*: Δt trend in temperature. *Below*: Δt dispersions for some temperatures.

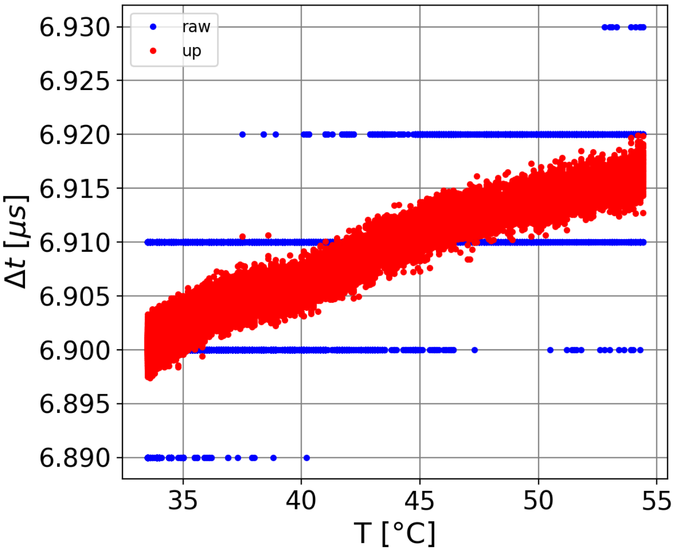

Figure 6.11: Second test in cooling with Eurosonic-MISTRAS in 16.48 mm. *Above*: Δt trend in temperature. *Below*: Δt dispersions for some temperatures.

Table 6.2: Values for $\sigma_{\Delta t}$ at various temperatures for different tests obtained with UTC110 card.

Test risc 1					
T	[°C]	24.48 ± 0.12	33.82 ± 0.14	44.29 ± 0.12	52.94 ± 0.07
$\sigma_{\Delta t}$	[ns]	1.7	1.9	1.8	1.8
Test risc 2					
T	[°C]	27.83 ± 0.10	33.82 ± 0.18	44.05 ± 0.13	53.21 ± 0.09
$\sigma_{\Delta t}$	[ns]	0.7	0.75	0.78	0.9
Test raff 1					
T	[°C]	33.00 ± 0.10	39.28 ± 0.06	43.93 ± 0.06	54.50 ± 0.16
$\sigma_{\Delta t}$	[ns]	0.7	0.75	0.78	0.9
Test raff 2					
T	[°C]	33.70 ± 0.01	39.85 ± 0.05	38.10 ± 0.06	53.82 ± 0.11
$\sigma_{\Delta t}$	[ns]	0.86	0.83	0.89	1.0

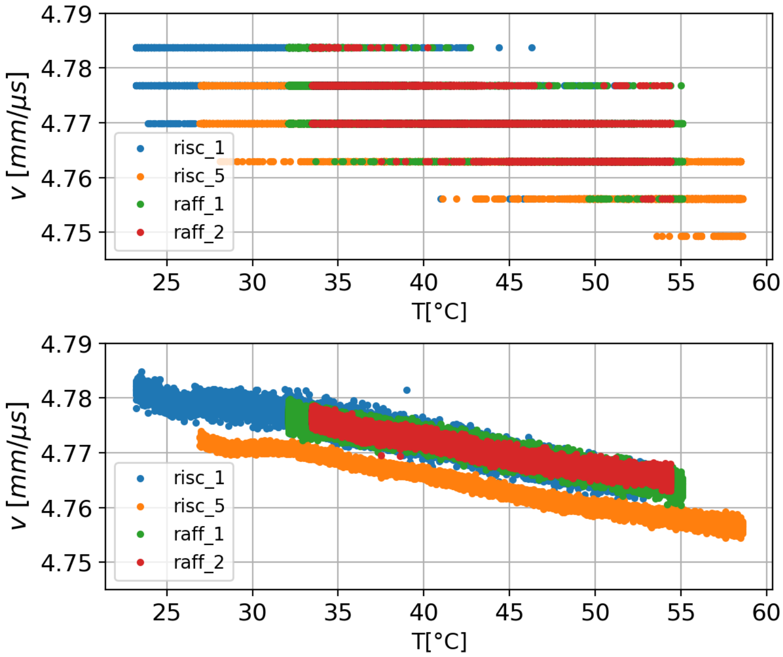

Figure 6.12: Superposition of the previous temperature tests of P-wave velocity in function of temperature. *Above*: raw values of c_P The *risc* points correspond to the *heating phase*, whereas the *raff* to the *cooling phase*.

deterministic manner the parameters describing the trends, for each copper specimens.

6.3.3 High temperature TOF measurements

The experiments have been organized by different type of the copper specimens, since they comes from different manufactures. The samples have been selected with various dimensions to be representative of the possible cases available in the steel plant. The linear regression analysis was applied to the velocity and temperature data. As regressor variable, 4 temperature measurements from thermocouple were used to calculate a single mean value; this approach has brought to a more reliable value in the region of the heating process, and confirms that in the region near the measurement the temperature is quite uniform. The temperature is therefore the predictor variable, *i.e.* the X independent variable. Th situation is the one where two physical quantities, say x and y, are known with different precision. x (temperature T) under control of the experimenter and measured with negligible error for statistical relevance, and the other Y (velocity v) known with less precision. So the model can be written as follow

$$Y = f(X) + Z \rightarrow v = m_v T + q_v + Z \tag{6.2}$$

where Z is the aleatory variable due to randomness of measurements ($\langle Z \rangle = 0$). The least squares formula to be minimized becomes

$$\chi^2(\boldsymbol{\beta}; x) = \sum_{i=1}^{n} \frac{(y_i - f(x_i; \boldsymbol{\beta}))^2}{\sigma_i^2} \tag{6.3}$$

with $\sigma_i = \mathrm{Var}[Z_i] = \mathrm{Var}[Y_i]$. The problem, now is the statistical error σ_i to assign at the observed aleatory variable v, since the v is a indirect physical quantity. What is really measured is Δt, and the thickness L, so to find the uncertainty over this one the errors must be propagated. If it is assume that the errors are only statistical and the quantities are independent, the formula for the error propagation can be obtained using the measured error s_L and $s_{\Delta t}$ [21]:

$$s_v^2 = \left(\frac{\mathrm{d}v}{\mathrm{d}L}\right)^2 s_L^2 + \left(\frac{\mathrm{d}v}{\mathrm{d}\,(\Delta t)}\right)^2 s_{\Delta t}^2 \tag{6.4}$$

which is valid in linear approximation. However, for the measurement uncertainty, the used density is the uniform probability density [21] and the law of error propagations is

$$\Delta_v = \left|\frac{\partial v}{\partial L}\right| \Delta_L + \left|\frac{\partial v}{\partial \Delta t}\right| \Delta_{\Delta t}. \tag{6.5}$$

The derivatives in the above expressions are:

$$\frac{\partial v}{\partial L} = \frac{\partial}{\partial L}\left(\frac{2L}{\Delta t}\right) = \frac{2}{\Delta t} \tag{6.6}$$

$$\frac{\partial v}{\partial \Delta t} = -\frac{2L}{\Delta t^2} \tag{6.7}$$

These two formula can be combined when in physical measurements they are both present. To find the probability density of the result, first identify with an estimate the contribution of both terms. Tab.6.3 reports the order of magnitude of these terms and the hypothesis behind them. With this assertions, the two types of error for the two different measurement are combined: the first thickness has predominant systematic term, the second for the time width, which has a higher statistical contribution.

So, if the estimates from Tab.6.3 are used in Eq.6.4 and 6.5, it's obtained

$$\begin{aligned} s_v^2 &= \left(\frac{\partial v}{\partial\,(\Delta t)}\right)^2 s_{\Delta t}^2 + \left(\frac{\partial v}{\partial L}\right)^2 s_L^2 && (6.8)\\ &\simeq (-1.25\,\mathrm{mm}/\mu\mathrm{s}^2)^2 \cdot (1 \times 10^{-3}\,\mu\mathrm{s})^2 && (6.9)\\ &\simeq (1.25 \times 10^{-3}\,\mathrm{mm}\,\mu\mathrm{s}^{-1})^2 && (6.10) \end{aligned}$$

$$\begin{aligned} \Delta_v &\simeq \left|\frac{\partial v}{\partial L}\right| \Delta_L + \left|\frac{\partial v}{\partial \Delta t}\right| \Delta_{\Delta t} && (6.11)\\ &\simeq 0.5\,\mu\mathrm{s}^{-1} \cdot 0.01\,\mathrm{mm} + 1.25\,\mathrm{mm}/\mu\mathrm{s}^2 \cdot O(1 \times 10^{-4}\,\mu\mathrm{s}) && (6.12)\\ &\simeq 0.005\,\mathrm{mm}\,\mu\mathrm{s}^{-1}. && (6.13) \end{aligned}$$

The final result is given by the formula for the standard deviation which is commonly used in these cases [21]

Symbol	U. M.	order	description
s_L	mm	$\ll O(1)$	Taking multiple measurement in the same point, the registered value is always the same, *i.e.* the measure is precise.
Δ_L	mm	0.01	The caliper sensitivity.
$s_{\Delta t}$	ns	$\simeq O(1)$	Statistical error of interpolated Δt, estimated from previous measurements on constant temperature.
$\Delta_{\Delta t}$	ns	$\ll O(1)$	Systematic error estimate for the measurement of interpolated Δt: the interpolated discretized sample steps are much smaller than ns.
$\frac{\partial v}{\partial L} = \frac{2}{\Delta t}$	μs^{-1}	$0.25 - 0.5$	With $4\,\mu s \leq \Delta t \leq 8\,\mu s$, covering the overall range of possible time interval.
$\frac{\partial v}{\partial \Delta t} = -\frac{2L}{\Delta^2}$	$mm/\mu s^2$	-1.25 to -0.625	With the copper thickness L between the $10\,mm$ and $20\,mm$ and Δt as before.

Table 6.3: Statistical and systematic error contributions for the measurement process in Eq. 6.4 and Eq. 6.5.

$$\sigma = = \sqrt{s_v^2 + \frac{\Delta_v^2}{12}} \tag{6.14}$$

$$= \sqrt{(1.25 \times 10^{-3}\,mm\,\mu s^{-1})^2 + \frac{(0.005\,mm\,\mu s^{-1})^2}{12}} \tag{6.15}$$

$$= \sqrt{1.25^2 + \frac{5^2}{12}} \cdot 1 \times 10^{-3}\,mm\,\mu s^{-1} \tag{6.16}$$

$$= 1.91 \times 10^{-3}\,mm\,\mu s^{-1}. \tag{6.17}$$

These results seems to be in agreement with the experimental observation of v, looking at the dispersion of the measurements. In Fig.6.13 and Fig.6.14 there are the results for the two test with the first approach method. They are reported to compare two cases: one from good measured data (Fig.6.13) and the other from bad ones (Fig.6.14). A way to check the hypothesis of normality of residual, and to assure the values in plot $(\hat{y}_i, z_i)$ are randomly distributed accordingly to the law of 3σ. Another check that could be done is to verify the correlation between residual, by plotting the points (z_i, z_{i+1}): if these point appear distributed like a cloud in the region near the origin, they are not correlated. Instead, situation like the one in Fig.6.14(d) reveals that the regression model does not describe well the data behaviour. The correlation between residues, seen in the (z_i, z_{i-1}) plot is evident, since the cloud is distributed in a region near the straight line $z_i = z_{i-1}$, and also concentrated in restricted areas in the plot. This comparison demonstrates that performing the regression analysis in data already distorted, with evidently problems due to the experimental procedure, does not produce useful results.

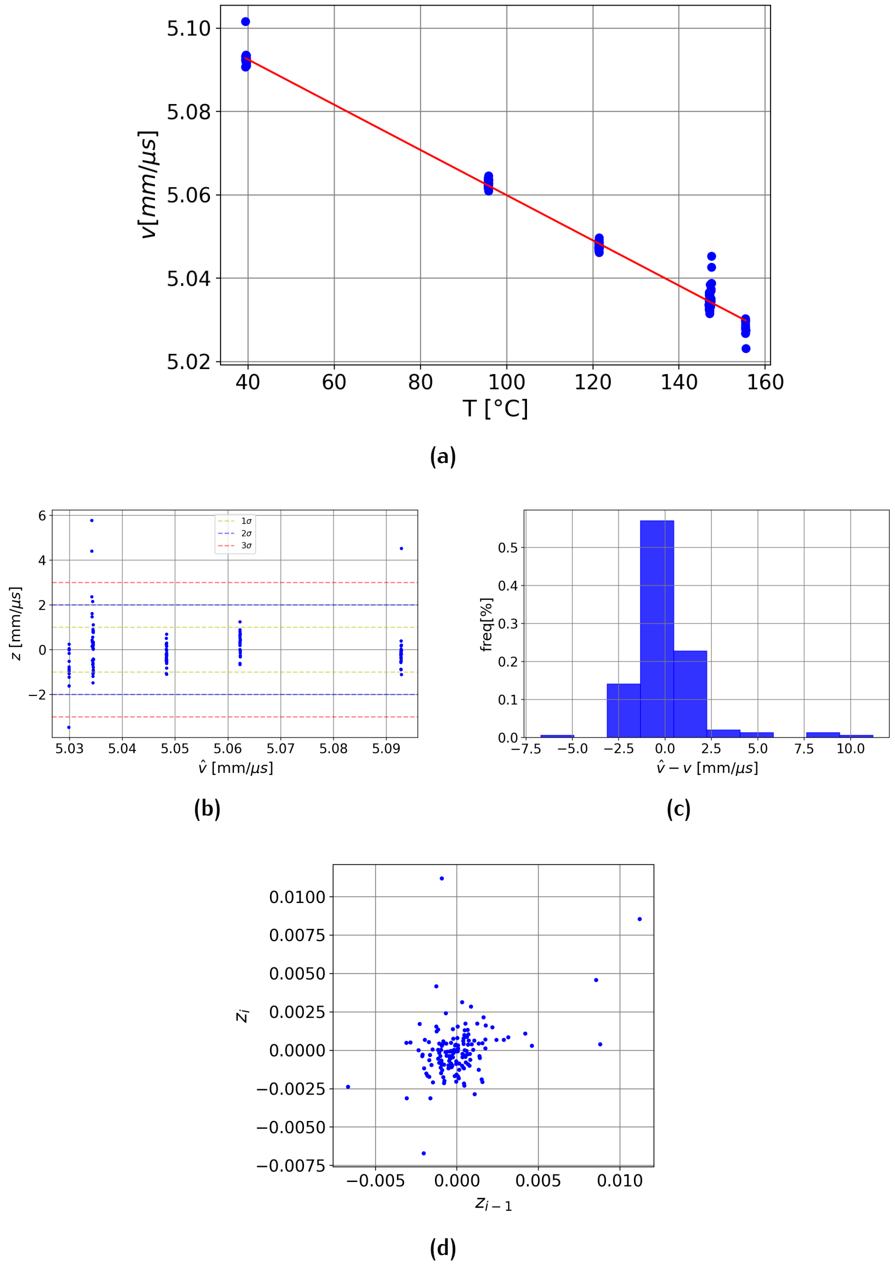

(a)

(b)

(c)

(d)

Figure 6.13: Linear regression analysis for type 3 specimen, first experiment.

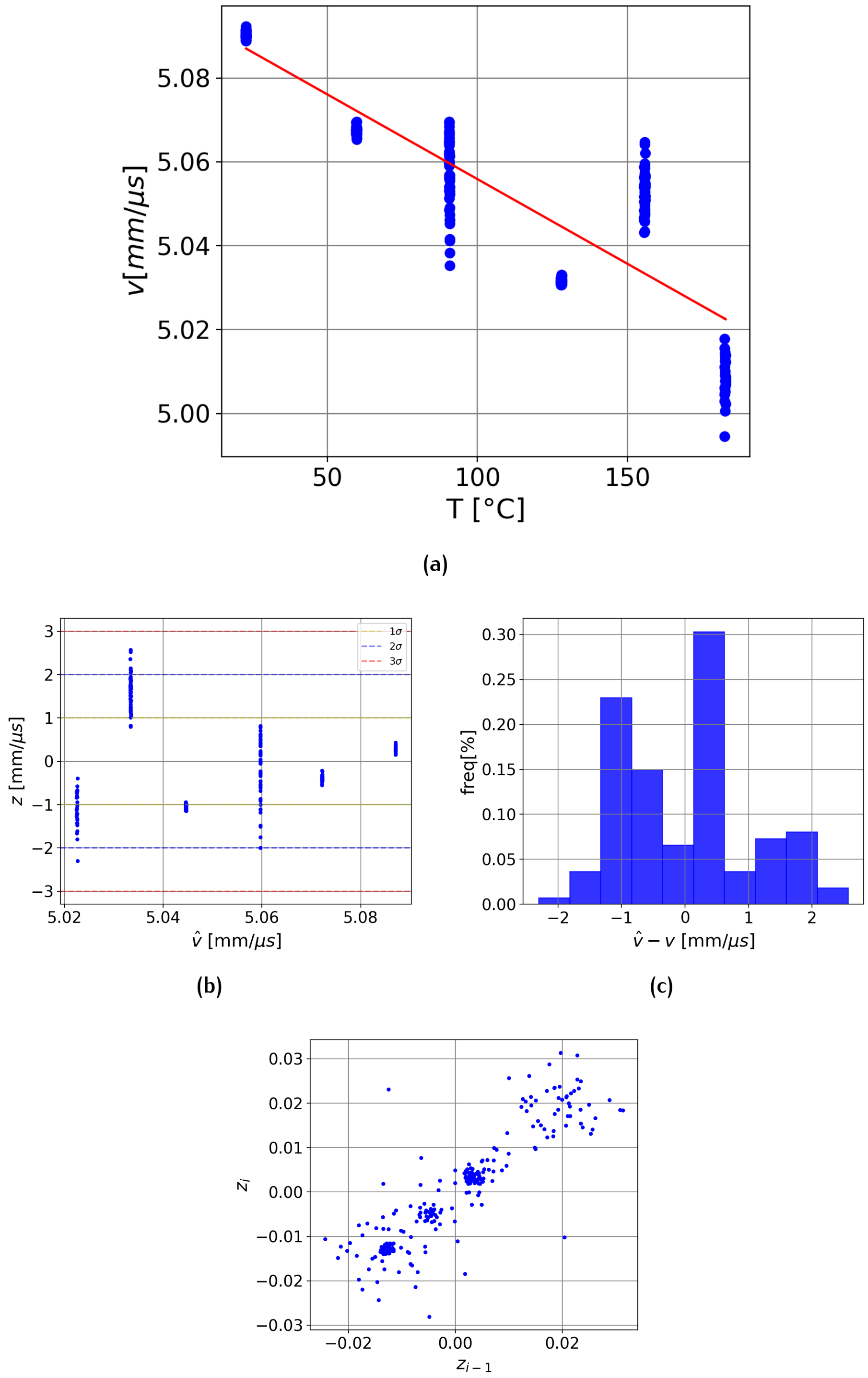

(a)

(b)

(c)

(d)

Figure 6.14: Linear regression analysis for type 3 specimen, second experiment.

6.3.4 Performing design of the Rexolite wedge material

Here the results for the last experimental tests are shown, where the Rexolite® substrate is machined to guarantees cooling of the piece: both for copper slab with 15.90 mm thickness. In the first test, in Fig.6.16, the final outcome seem to be not good as for the case of the fixed Rexolite®. In this situation the dispersion in the overall range of extended temperature is worse than for the latter case. Since the Rexolite® temperature, show in Fig.6.15 (b) in the *blue* curve is far lower the critical limit and in particular for copper temperature of about 150 °C the maximum value is 65 °C, it couldn't be an effect relates to temperature attenuation. Confirmation to this is the amplitude trend reported in the same group of figures, in (a), where also for values under the 4 V the oscillation of the peaks are controlled. Despite this fact, the dispersion of v at some fixed temperature is too wide, and this is clearly shown in the red histograms of Fig.6.16.

After this test, the aligment of the Rexolite piece was not so good, since the copper specimen has not a perfectly planar interface. Since the substrate is fixed with two screws, an unbalanced regulation with these two could make the Rexolite® crooked. In this way, the measurement could have a systematic error due to a not aligned Rexolite. This problem is quite important since the request to have a two planar surfaces in contact is difficult to satisfies. The Rexolite® is a rigid material, but if it is heated many times at a temperature near its *glass temperature*, under a pressure due to fixing, it can changes its shape. Moreover, copper slabs used for all these experimental tests come directly from industrial plants where they could have be subjected to huge thermal stresses, very differently to those testable in our experiments.

In the test reported in Fig.6.17, the results are quite better in terms of the dispersion of the measurements. In fact, looking at the amplitude and velocity trends the points are more narrow distributed than for the previous cases even for the same test made with the previous Rexolite piece. Until the temperature remains below the critical threshold of 150-160 °C, the dispersion is optimal, since it is far below the estimated $\sigma = 0.001\,\text{mm}\,\mu\text{s}^{-1}$ from the error analysis and other experiments. However, it makes worse when the limit is overtook, and the amplitude of Cu_1 and Cu_2 drops to values near 2-3 V. Moreover, as depicted in Fig.6.17 (b), the last interval acquisition there were a problem with the heating source, causing a drop in temperature with problems during acquisition. In this region the temperatures become unstable and the measured values oscillate too much: this effect is almost due to the great drop in amplitude observations. These last points, at the end of the temperature curve, are therefore not included for the regression procedure, since they are source of useless noise and not reliable. Furthermore, the errors of these points is higher than for the previous acquisitions, and these points cannot be treated together because they may invalidate the outcome.

Using this approach to exclude those noisy points, the linear regression is performed for these two presented case, both for copper slab of thickness 15.90 mm. For the first analyzed test, the dispersions in Fig.6.16 are wider on the overall measurement range than the successive case in Fig.6.18. For the first, shown in Fig.6.19, the residual are normally dispersed around the estimated value $\hat{v}_i$.

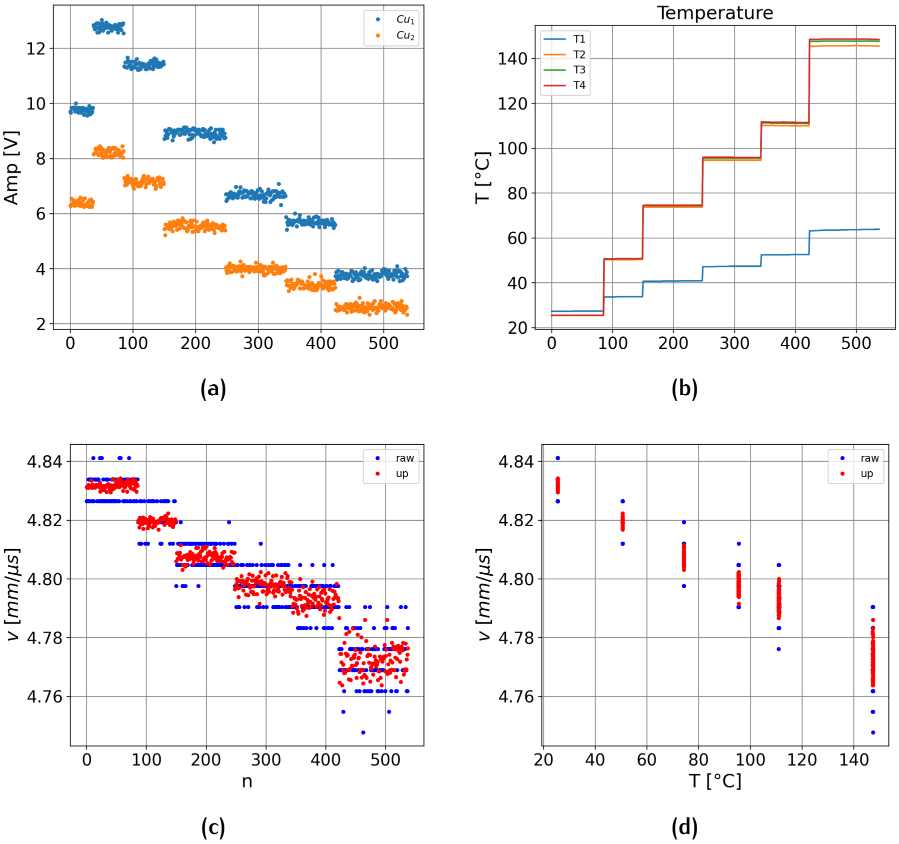

(a)

(b)

(c)

(d)

Figure 6.15: Results for copper slab, type 1, thickness 15.90 mm, test 1.

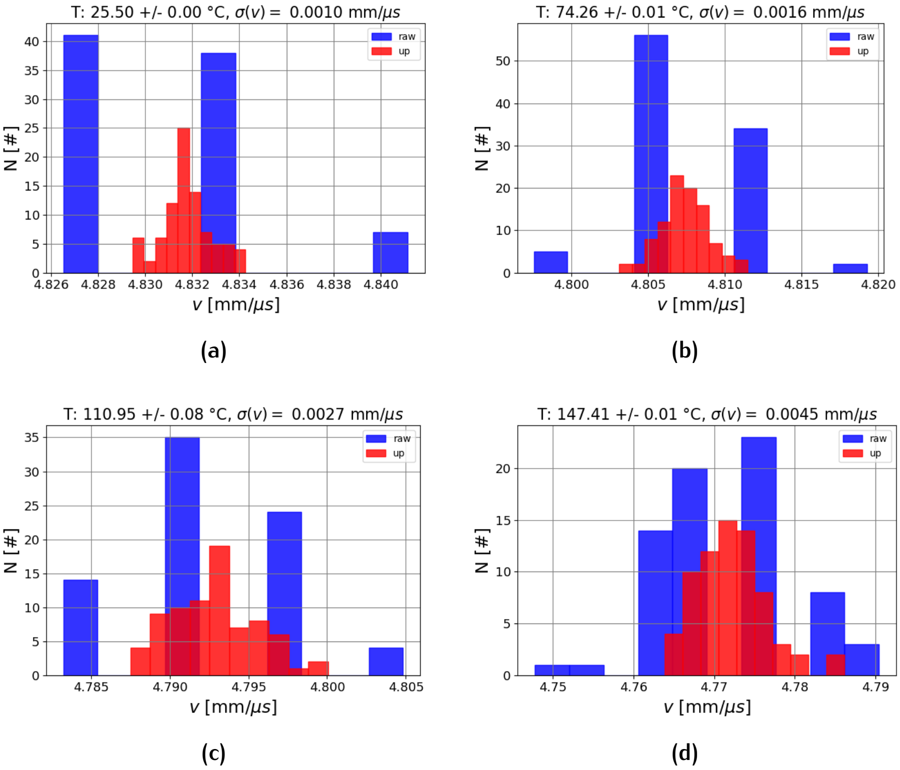

(a)

(b)

(c)

(d)

Figure 6.16: Dispersion analysis for copper slab, type 1, thickness 15.90 mm, test 1.

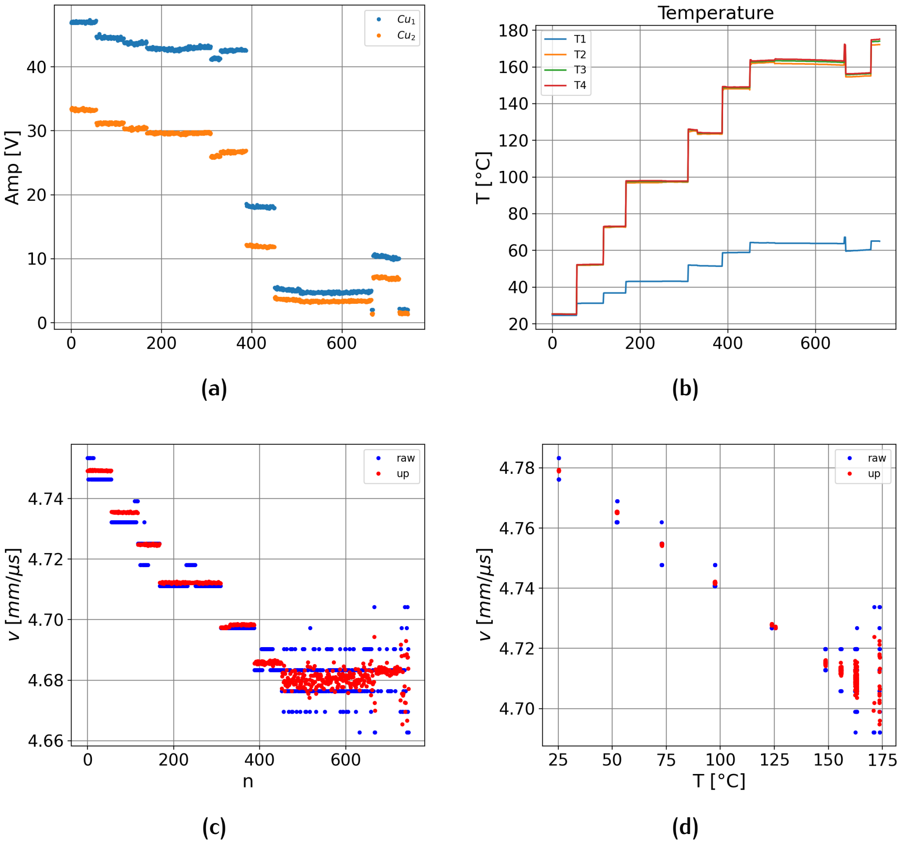

(a) (b)

(c) (d)

Figure 6.17: Results for copper slab, type 1, thickness 15.90 mm, test 2.

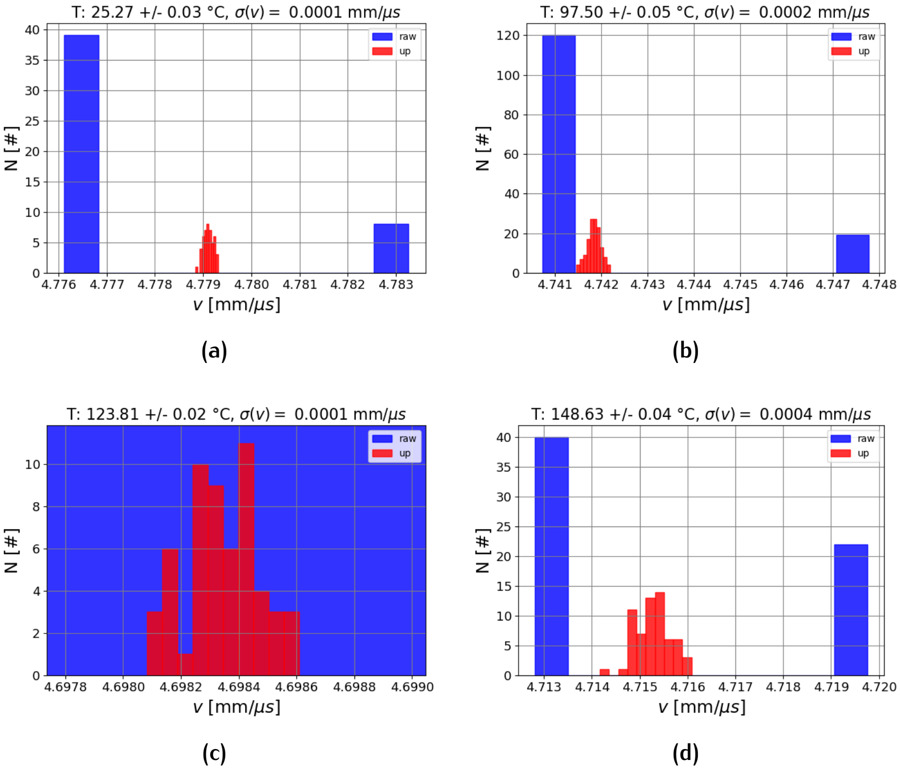

(a) (b)

(c) (d)

Figure 6.18: Dispersion analysis for copper slab, type 1, thickness 15.90 mm, test 2.

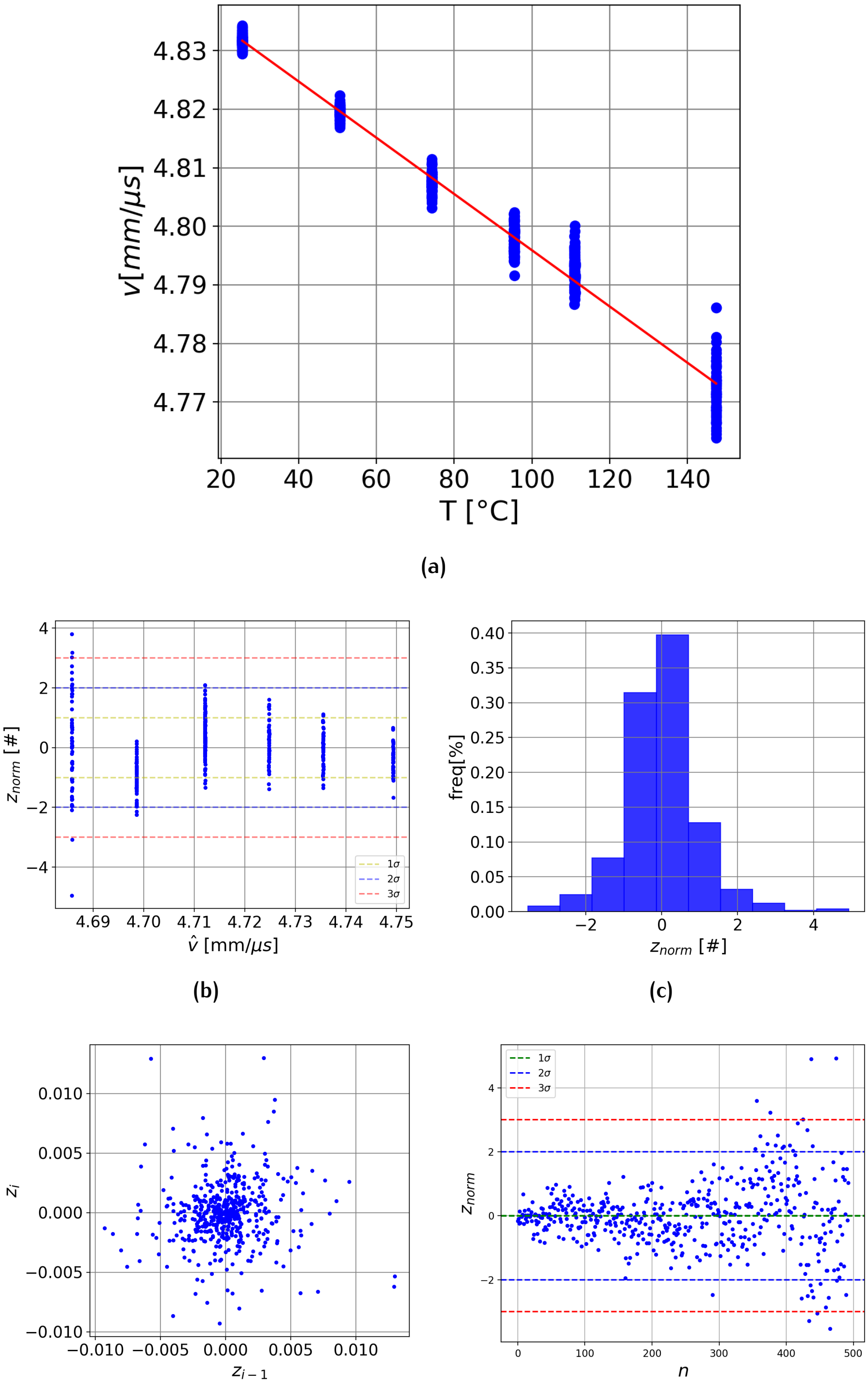

(a)

(b)

(c)

(d)

(e)

Figure 6.19: Results for linear regression on slab with thickness 15.90 mm.

The second test made in the same configuration, Fig.6.17-6.18, allowed to obtain more precise acquisition, until 150 °C. The screenshot of the acquisition software is reported, in this way the degeneration of the signal is visualized in Fig.6.21 at three different temperatures. It is clear that the precision of the measurements changes dramatically at a certain point, but the maximum temperature can be increased. In addition to the dispersion measurement of the signals, it is possible to notice the residual trends versus the acquisition time or order: the result, shown in Fig.6.20(e), are distributed accordingly to the 3σ law. However, even if the points which can influence the measure are discarded, around the sample number 300 is possible to see an abrupt trend change. The plot to demonstrate the residual correlation (z_i, z_{i-1}) appears to be quite random.

With this new setup, some improvements have been done in terms of increasing precision at high temperature measurements, at least to reach the temperature around 140-150 °C. Certainly, in an immersion setup, these temperatures would never be reached, since the maximum were about 60 °C.

6.3.5 Measurements with industrial ultrasonic setup

The aim was to obtain a quantitative description of the results with the electronics used for the customized sensor. In other words, the validity of the elaboration made by real-time software has been checked, and then has been studied the influence on temperature tests. The tests have been performed again using the last Rexolite piece visualized in Fig.6.22. The main difference respect to the UTC110 card is the sampling rate of 80 MHz. The results shown here regards the 10 mm copper thickness. Two different measurements with the final Rexolite substrate have been made: Fig.6.24 and Fig.6.25 provide the results of the regression procedure on the acquired data obtained with the custom electronics.

The software for this electronic allows to set a gain variable on different portions of the signal: this could be done by an AGC (*Automatic Gain Control*), setting a constant value for the signal amplitude. An improvement in the design of the electronic hardware has required the implementation of the AGC in the circuit elements, in this way, differences due to temperature attenuations are flattened. This situation is clearly depicted in Fig.6.24 (a) and Fig.6.25 (a) where, except the case of points at the ending point (higher n), the oscillation are limited to a fixed values. These two tests compare the performance of the different heating or cooling approaches, visible when looking the (b) figures. In (c) figures of both tests, the behaviour of the v measurements is shown: even the two test have been made one in decreasing temperature and the other in the reverse way, in the final part of the test there are both more noisy than the other, meaning the high temperature couplant was deteriorating. This of course is the critical point observed for the overall previous tests. In the first, the residual distribution, even if without clear correlation (Durbin-Watson Statistic equal to 2.0357, Fig.6.24 (f)) is clearly highly dispersed around the mean value, and this cannot be considered a good results for our standard, where it's preferred to have a reduced dispersion around the centred value at a fixed temperature. Even if it's not

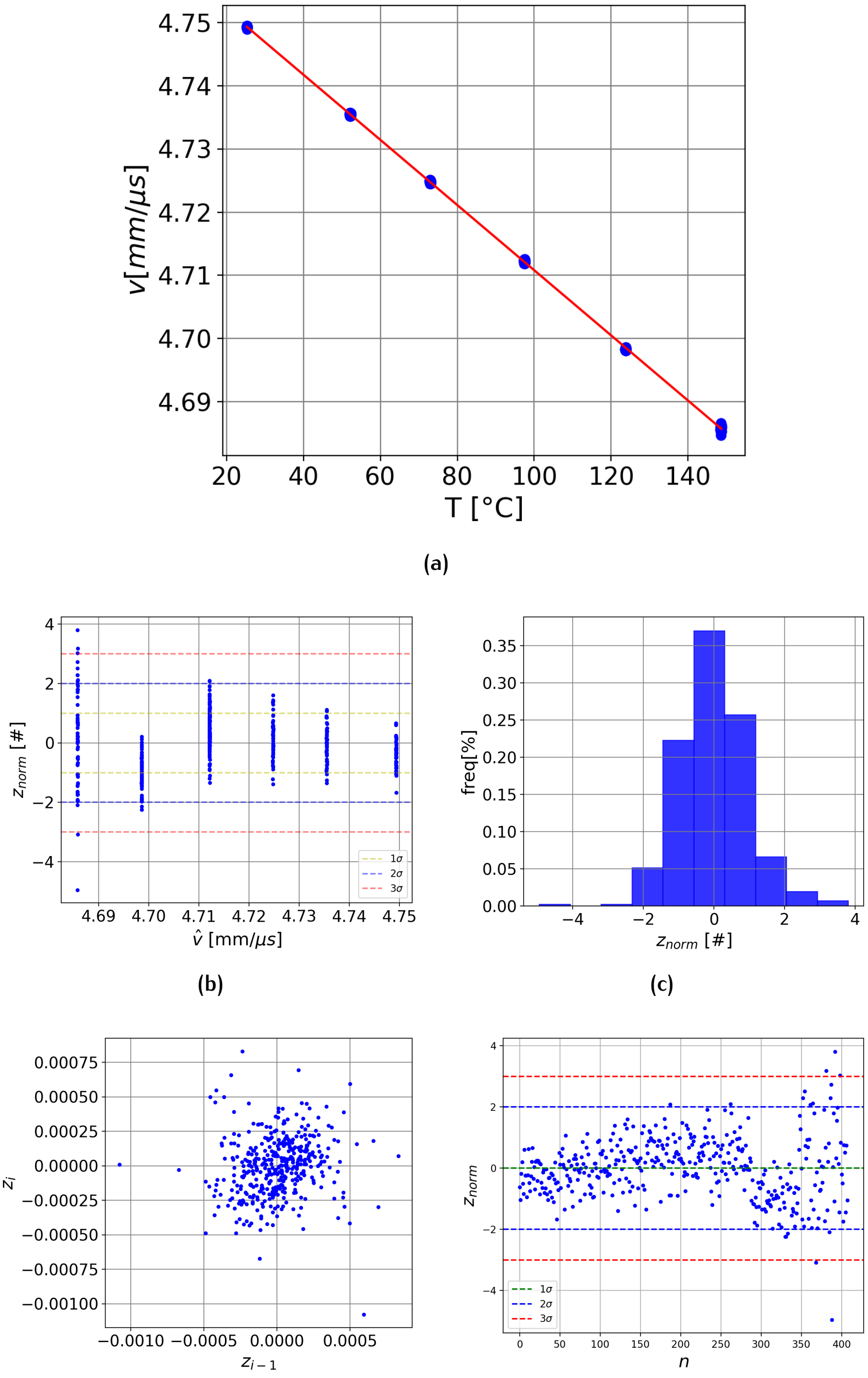

(a)

(b)

(c)

(d)

(e)

Figure 6.20: Results for linear regression on slab with thickness 15.90 mm in second test.

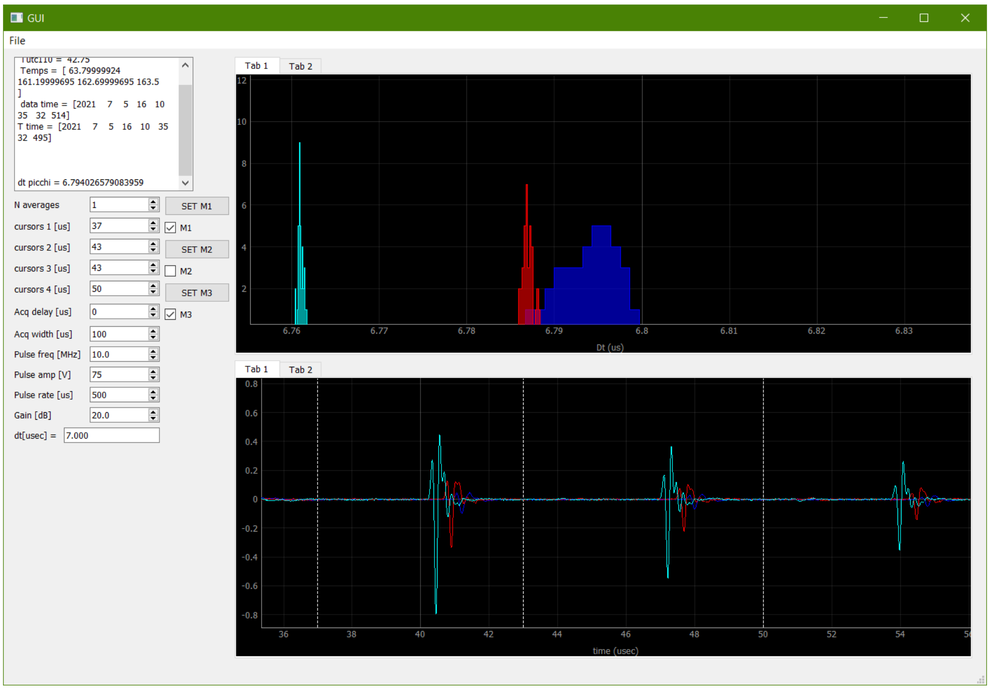

```
Tutc110 = 42.75
 Temps = [ 63.79999924
161.19999695 162.69999695 163.5
]
 data time = [2021    7    5   16   10
35   32  514]
T time = [2021    7    5   16   10   35
32  495]


dt picchi = 6.794026579083959
```

N averages 1
cursors 1 [us] 37 ☑ M1
cursors 2 [us] 43
cursors 3 [us] 43 ☐ M2
cursors 4 [us] 50
Acq delay [us] 0 ☑ M3
Acq width [us] 100
Pulse freq [MHz] 10.0
Pulse amp [V] 75
Pulse rate [us] 500
Gain [dB] 20.0
dt[usec] = 7.000

(a)

Figure 6.21: Screenshot of the GUI software. *Above*: window representing real time dispersion of the difference $\Delta t = t_{Cu_1} - t_{Cu_2}$ at different temperatures. *Below*: corresponding signal decay trends.

(a) (b)

Figure 6.22: Rexolite® piece disposition in the two test on copper of thickness 15.90 mm.

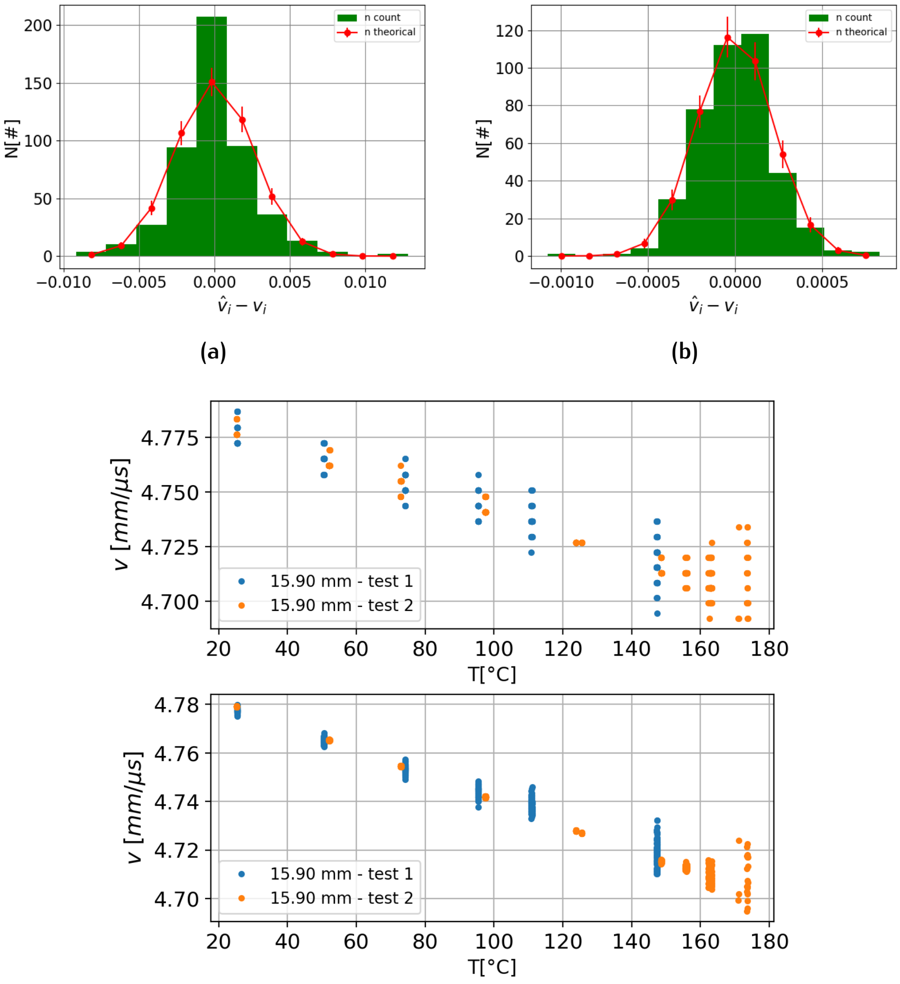

(a) **(b)**

(c)

Figure 6.23: *Above*: hypothesis testing of normality of residual dispersion. For both tests we have χ^2 values contained in the range $\chi_l^2 < \chi^2 < \chi_h^2$, so the hypothesis of residuals normal distribution can be accepted. *Below*: Superposition of the two v trends for the measurements in copper slab with thickness 15.90 mm.

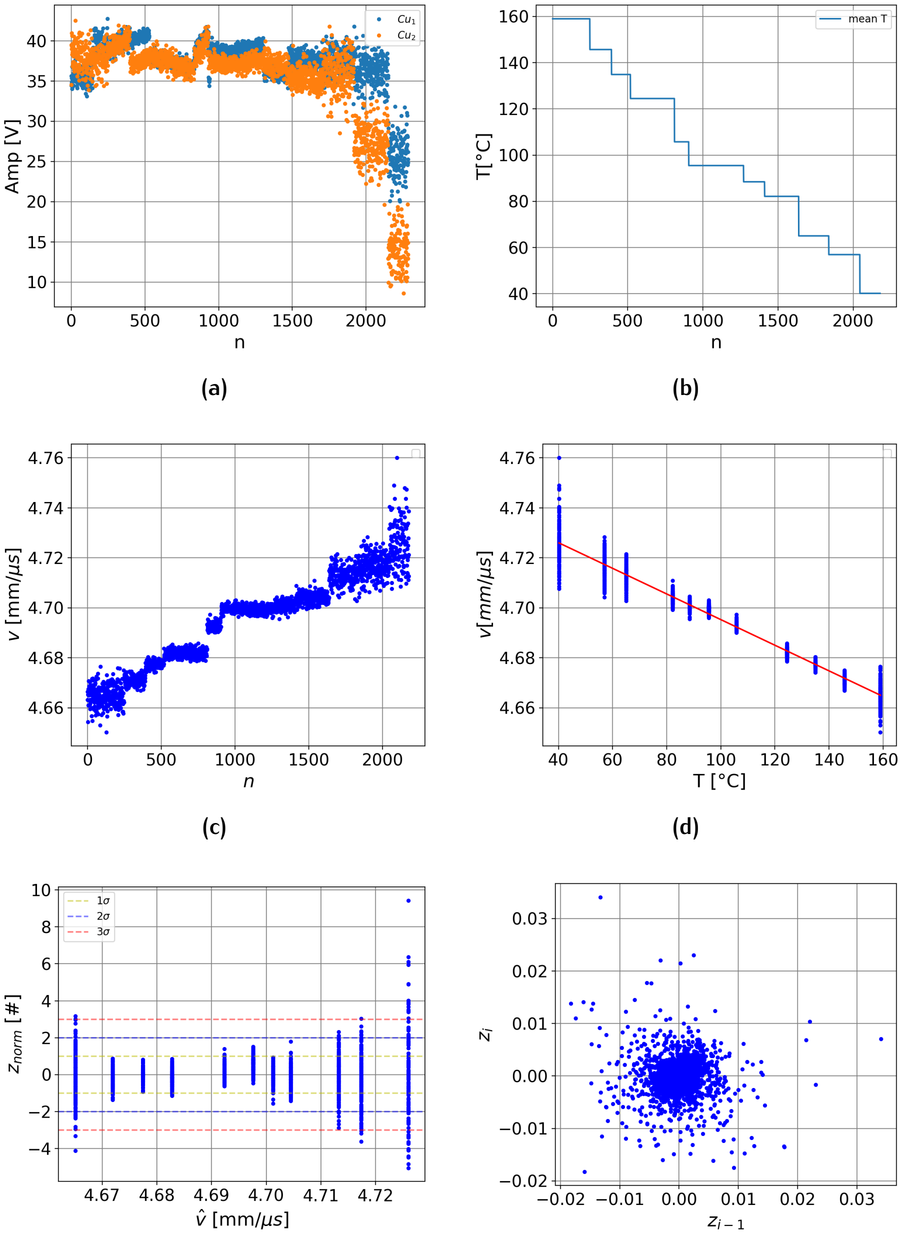

(a) (b)

(c) (d)

(e) (f)

Figure 6.24: 10 mm copper thickness measurement with custom electronic for ultrasonic sensor.

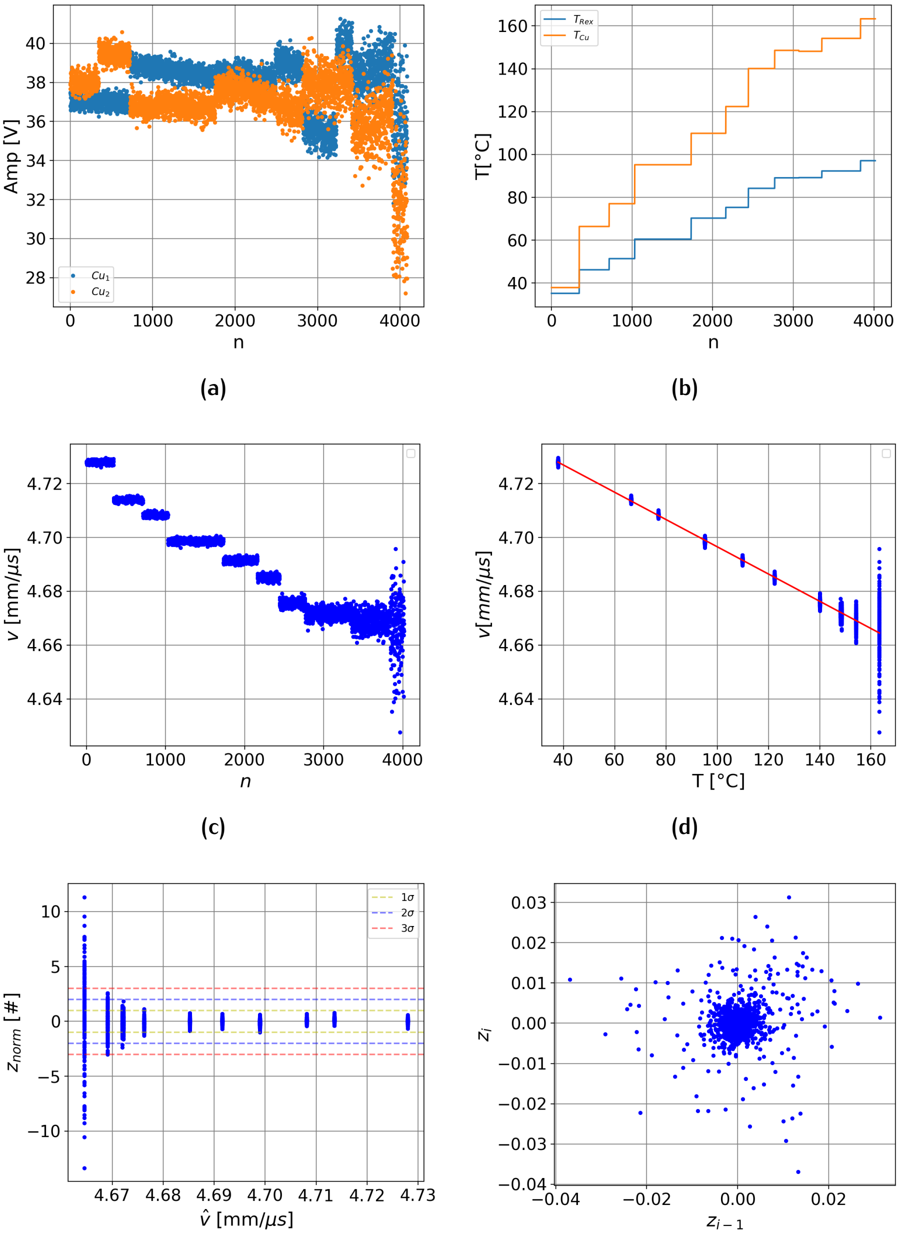

(a) (b) (c) (d) (e) (f)

Figure 6.25: Second test results with 10 mm copper thickness with custom electronics.

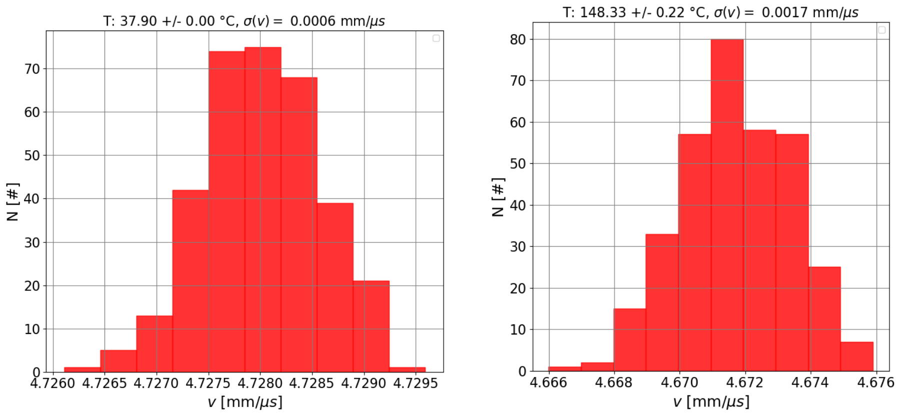

(a) (b)

Figure 6.26: Dispersion for v at different temperatures. *Left*: 37.90 °C and *right*: 148 °C.

reported the distribution at each temperature, the conclusion is that even if an experimental apparatus is build to paid specific attention for reducing high noisy temperatures, the couplant state is one parameter to monitor during the process, and it's hard to maintain this parameter unchanged.

In the second test, made in a raising temperature setup, results are better in terms of dispersion around the temperatures. Before starting the heating, the couplant gel under the Rexolite substrate has been replaced, then fixed it with to the copper and started the experiment. Up to temperature near 150 °C, a very reduced dispersion has been observed, in agreement with those obtained with the Eurosonic-MISTRAS UTC card. Fig.6.26 shows the dispersions of two measurement for the second test on 10 mm copper. The standard distribution for the errors is recognizable, but the $\sigma(v)$ slightly differ from temperature to temperature; however, with this approach an overall dispersion of about 0.001 mm μs^{-1} has been reached at approximately the 150 °C.

However, even the measurement here obtained seem to be better than the previous case, the Durbin-Watson statistic reveals that the residual correlation is more evident (1.5759 which is much lower than 2). The conclusion can be that it is due to the difference between precision in the last measurements of the curve, where the signals are more damped. A last comparison could be done with the superposition fo the reported tests. In Fig. 6.27 are presented the results already shown in Fig.6.28 (b), for the case of 10 mm copper thickness. To better understand the cited figure, the summary of the results is:

- *Blue*: first approach test, with removable transducer to keep the contact the least possible;
- *Orange*: replicate of the previous test;
- *Green*: second approach test, Rexolite fixed during the overall time;
- *Red*: replicate of the previous test, but in another point on the same specimen;

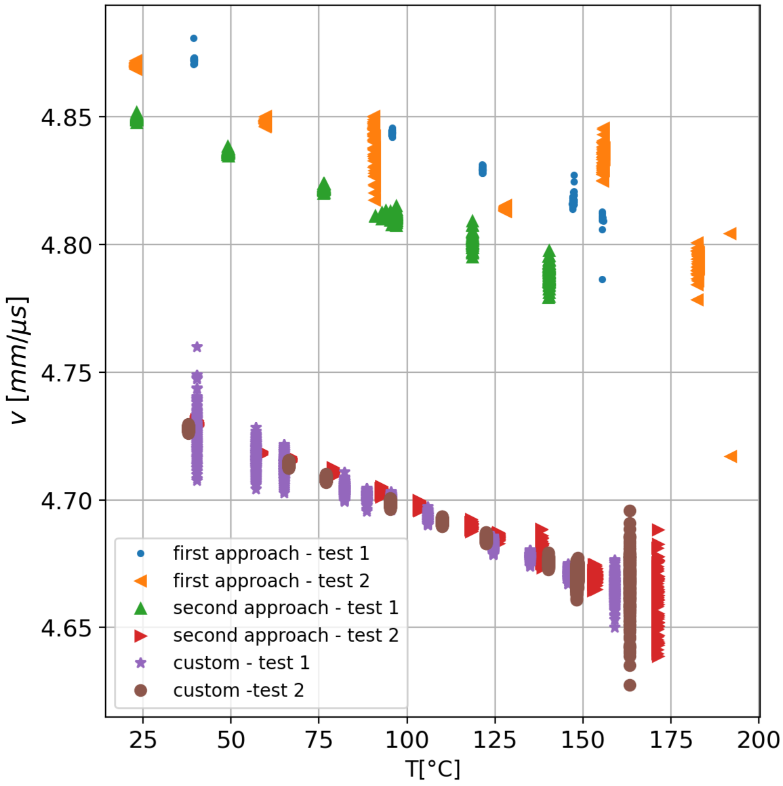

(a)

Figure 6.27: Comparison for measurements in copper 10 mm. Tests with Eurosonic-MISTRAS® UTC card (100 MHz) and custom electronics (80 MHz).

- *Purple*: final Rexolite (Fig.5.10), same point of measurement of *Red* points;

- *Brown*: replicate of the previous test.

The *blue* and *orange* cases are replicates obtained with the first approach measurement technique: the imprecision due to the every time changing condition has already been analyzed. For the purple and brown cases instead, a perfect match of the trends is verified. For these last two, there's an huge improvements on the precision of measurement techiques, also at high temperatures, realized with the custom electronic, even if the sampling signal frequency is lower than the one of the Eurosonic-MISTRAS tests. On the other hands, experimental points in red show that also the second approach technique has revealed quite good. However, the most notable thing is the difference between these last ones and the green points, acquired with the same approach (the 2nd), but in different position on the copper: for the *red* ones, the transducer positioning was the same just as for the purple and brown points. This could be due to the different thermal history of the copper samples, which has not been considered here until these results. In fact, also using three different techniques, measurements realized about in the same positioning have lead to similar results.

Results first method		Fixed Rexolite® results		Results with cooled Rexolite®	
T [°C]	σ_v [mm µs^{-1}]	T [°C]	σ_v [mm µs^{-1}]	T [°C]	σ_v [mm µs^{-1}]
				test 1 (with systematic error)	
24.2 ± 0.0	0.0045	22.40 ± 0.0003	0.0003	25.50 ± 0.00	0.001
58.43 ± 0.19	0.0008	53.59 ± 0.08	0.0003	74.26 ± 0.01	0.0016
60.99 ± 0.05	0.0030	91.67 ± 0.10	0.0004	110.95 ± 0.08	0.0027
122.95 ± 0.30	0.0056	124.96 ± 0.03	0.0005	147.41 ± 0.01	0.0045
134.79 ± 0.42	0.0039	147 ± 0.04	0.0015		
				test 2	
				25.27 ± 0.03	0.0001
				97.50 ± 0.05	0.0002
				123.81 ± 0.02	0.0001
				148.63 ± 0.04	0.0004

Table 6.4: σ_v values for different temperatures, for copper slab of thickness 15.90 mm, (type 1).

6.4 DISCUSSION ON THE RESULTS

The summary of these consideration is in Tab.6.4, where the dispersion for the experimental measurements are presented, starting from the first measurement approach, passing through the test with the fixed but not cooled Rexolite® at the surface and the final experiments, where the reported tests have been (test 1 and test 2). The first thing to notice is the importance to reduce systematic errors, that is, mechanical or technical imprecision during the experimental act, before starting the experiments: the expectation to obtain lower error in the last setup configuration was high, and it has been partially satisfied since the precision of the measurement increases. In particular, the evidence of the corrected evaluation of the thickness is the crucial factor which determine the variation in the intercept parameter q_v. This is a systematic error that could be included in the measurement, and its contribution has been analysed for the error evaluation. This action requires study for the development of a new and more reliable approach to detect the copper thickness, or, more practical, the use of standardized copper samples with predetermined thickness, in order to being sure such bias factors do not alter the measurements outcome. In this way, a certified copper specimen could be used to classify the similar copper slabs coming from several plants, to construct a database for all these characteristics.

Second, the dispersion in Δt measurements varies from method to method: it does not seem that there will be a particular trend in the performed tests, but the applied modification seem to perform better for the last work on the Rexolite. For the *test 2*, from the last approach, the obtained precision is the highest, and also at the highest temperature values it is $\sigma_v < 0.001\,\mathrm{mm\,\mu s^{-1}}$.

To conclude this part, in Fig.6.28 is shown the superposition of all the v trends, for each experimental sample. The measurements have been grouped according to the specimen:they are collected in the final Tab.6.5, to visualize

Results first method						
Thickness	$\hat{m}_v \pm t_{1-0.05/2}s(\hat{m}_v)$	$\hat{q}_v \pm t_{1-0.05/2}s(\hat{q}_v)$	R^2	R_a^2	d	$t_{m_v} = \frac{\hat{m}_v}{s(\hat{m}_v)}$
10.40 mm	$-5.24 \times 10^{-4} \pm 0.1 \times 10^{-4}$	4.893 ± 0.001	0.984	0.984	0.973	97.6
10.40 mm	$-3.94 \times 10^{-4} \pm 0.28 \times 10^{-4}$	4.876 ± 0.003	0.738	0.737	0.402	28.2
Fixed Rexolite® results						
Thickness	$\hat{m}_v \pm t_{1-0.05/2}s(\hat{m}_v)$	$\hat{q}_v \pm t_{1-0.05/2}s(\hat{q}_v)$	R^2	R_a^2	d	$t_{m_v} = \frac{\hat{m}_v}{s(\hat{m}_v)}$
10.40 mm	$-5.18 \times 10^{-4} \pm 0.06 \times 10^{-4}$	4.8619 ± 0.0006	0.988	0.988	1.851	169.0
10.87 mm	$-5.25 \times 10^{-4} \pm 0.06 \times 10^{-4}$	4.751 ± 0.0006	0.971	0.971	2.543	177.5
16.02 mm	$-5.33 \times 10^{-4} \pm 0.02 \times 10^{-4}$	4.7400 ± 0.0003	0.997	0.997	1.243	448.5
Results with cooled Rexolite®						
Thickness	$\hat{m}_v \pm t_{1-0.05/2}s(\hat{m}_v)$	$\hat{q}_v \pm t_{1-0.05/2}s(\hat{q}_v)$	R^2	R_a^2	d	$t_{m_v} = \frac{\hat{m}_v}{s(\hat{m}_v)}$
15.90 mm	-4.76 ± 0.06	4.7894 ± 0.0006	0.979	0.979	1.925	159.5
15.90 mm	-5.01 ± 0.03	4.7910 ± 0.0004	0.991	0.991	1.613	282.8
-Custom electronic- Thickness						
10.87 mm	$-5.13 \times 10^{-4} \pm 0.04$	4.7466 ± 0.0005	0.962	0.962	2.036	233.3
10.87 mm	$-5.16 \times 10^{-4} \pm 0.02$	4.7479 ± 0.0003	0.976	0.976	1.576	402.5

Table 6.5: Summary of results from statistical analysis. Here are classified the results obtained both with the state of the art and with the custom electronic hardware.

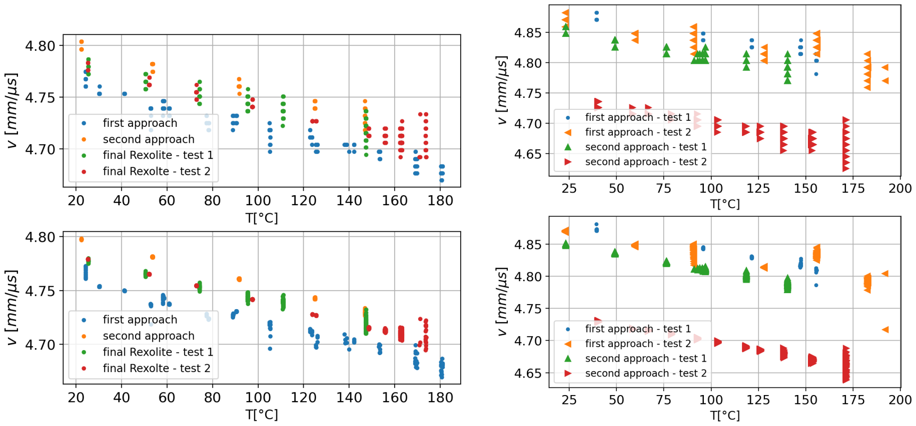

(a) 15.90 mm.

(b) 10 mm.

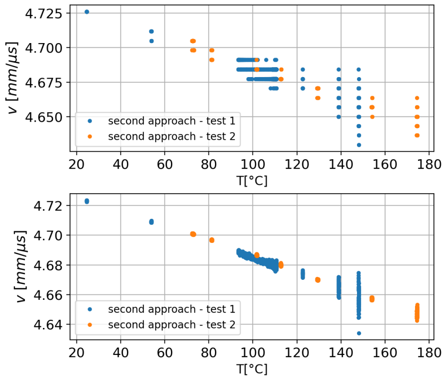

(c) 16 mm

Figure 6.28: Superposition of linear trends for the velocity v for the three copper samples.

the outcome of different experimental procedure applied to the same sample.

Velocity are different among the different specimens, even they are made of the same material, this could be a consequence of the different chemical composition of the metal alloys. An interesting example is in Fig.6.28 (b), where 4 tests are compared: 2 are realized with the *first approach* technique, and they clearly appear to be more noisy than the other. The third test (marker in green) is realized with the fixed Rexolite in the same position of the previous (blue and orange) tests. An improvement of the quality of measure is confirmed. The last test (red marker), is instead realized on another position, where the thickness is slightly different (10.87 mm). The specimen, as already specified, hasn't a constant thick so change the position of measurement induces always change in the thickness. This last consideration reveals once again how important is to determine a procedure with some copper specimens satisfying some standard.

7 CONCLUSIONS

With the combined interpolation and regression techniques, the results show an improvement in resolution for TOF measurements and therefore, indirectly, for acoustic velocity. Furthermore, the reconstructed signal is found to be more stable also when variations due to noise affects greatly its shape: this is certainly a relevant result since in operative conditions signal will be affected by a lot of external noise. Indeed, environmental conditions in the steel plant are not always under control, so this goal is a very important part of the implemented solution. The estimate of the temporal position of the maximum peak obtained with this technique was therefore accurate for the required purpose, which is a statistical variation on the order of the nanosecond, and stable over time for acquisitions at the same temperature. The goal of this thesis, defined at the beginning, was to study, experience with, and define in a prototype what later actually has become an industrial product. In this sense, the research activity carried out has always been outlined following this goal.

BIBLIOGRAPHY

[1] K. Aki and P. G. Richards. *Quantitative Seismology*. Second. University Science Book, 2002. ISBN: 0-935702-96-2.

[2] World Steel Association. *World Steel Association - Statistical reports*. URL: https://worldsteel.org/steel-by-topic/statistics/steel-statistical-yearbook.

[3] Mark V. Brook. *Ultrasonic inspection technology development and search unit design: examples of practical applications*. Ed. by John Wiley and Inc. Sons. 1st edition. 2011. DOI: 10.1002/9781118104781.

[4] V. Cerveny and I. Psencik. "Gaussian Beams and Paraxial Ray Approximation in Three-Dimensional Elastc Inhomogeneous Media". In: *Journal of Geophysics* 53 (1983), pp. 1–15.

[5] C. Chow and I. V. Samarasekera. "High speed continuous casting of steel billets: Part 1: General overview". In: *Ironmaking & Steelmaking* 29.1 (2002), pp. 53–60. DOI: 10.1179/030192302225001938. eprint: https://doi.org/10.1179/030192302225001938. URL: https://doi.org/10.1179/030192302225001938.

[6] C. Chow et al. "High speed continuous casting of steel billets: Part 2: Mould heat transfer and mould design". In: *Ironmaking & Steelmaking* 29.1 (2002), pp. 61–69. DOI: 10.1179/030192302225001947. eprint: https://doi.org/10.1179/030192302225001947. URL: https://doi.org/10.1179/030192302225001947.

[7] G. Fleury and C. Gondard. "Improvements fo ultrasonic inspections through the use of piezocomposite transducers". In: (1994). Ed. by 6th 6th European Conference on non destructive testing.

[8] Bin HU, Yu-hong ZHU, and Chao SHI. "Effect of Temperature on Solid Ultrasonic Propagation Using Finite Element Method and Experiments". In: (2018), pp. 107–111. DOI: 10.1109/FENDT.2018.8681981.

[9] G.A. Korn and T.M. Korn. *Mathematical Handbook for scientists and engineers*. 2nd edition. Dover Publications, 2000. ISBN: 978-0-486-41147-7.

[10] R. G. Lyons. *Understandin Digital Signal Processing*. 3rd edition. Pearson, 2011. ISBN: 978-0-136-99429-9.

[11] I. Mazza. "Sviluppo e sperimentazione metodi innovativi di imaging e caratterizzazione ad alta risoluzione basati su onde di Rayleigh". PhD Thesis. Università Degli Studi di Trieste, 2014.

[12] EUROSONIC MISTRAS Group SA. *Ultrasonic module UTC 110*. 2012. URL: https://eurosonic.com/en/products/ut-solutions/utc-110.html.

[13] EUROSONIC MISTRAS Group SA. *UTC 110 User Manual*. 2015.

[14] D. C. Montgomery. *Design and Analysis of Experiments*. Ed. by John Wiley and Inc. Sons. 6th edition. 2005. DOI: 978-0-471-48735-7.

[15] L. Mordfin. *Handbook of Reference Data for Nondestructive Testing*. ASTM International, 2002. ISBN: 0-8031-2092-3.

[16] H. Nyquist. “Certain topics in telegraph transmission theory”. In: *Transactions of the AIEE* 47 (1928), pp. 617–644.

[17] M. P. Pozar. *Microwave Engineering*. Ed. by John Wiley and Inc. Sons. 4th edition. 2012. DOI: 978-0-470-63155-3.

[18] LC PPC Polymer Plastic Company. *Rexolite*. URL: https://www.polymerplastics.com/Rexolite-High-Performance-Plastic.shtml?gclid=CjwKCAjw49qKBhAoEiwAHQVTkUEKckTS77Z9_bewEY4s3oFsAhqvijzB1TqqUkzk1PXv3tU1BoCLdoQAvD_BwE.

[19] “Quantitative Analysis of GPR Signals: Transmitted Wavelet, Amplitude Decay and Sampling-Related Amplitude Distorsion”. In: *Pure Appl. Geophys.* (2017). DOI: 10.1007/s00024-017-1752-2.

[20] P. Raminez Lopez. “Modelling shell and oscillation mark formation during continuous casting via Explicit incorporation of slag infiltration”. PhD Thesis. Imperial College, London, 2010.

[21] A. Rotondi, P. Pedroni, and A. Pietavolo. *Probabilità, Statistica e Simulazione*. Ed. by Springer. Terza edizione. 2012. ISBN: 978-88-470-2363-5. DOI: 10.1007/978-88-470-2364-2.

[22] I.V. Samarasekera and J. K. Brimacombe. “The Thermal Field in Continuous-Casting Moulds”. In: *Canadian Metallurgical Quarterly* 18.3 (1979), pp. 251–266. DOI: 10.1179/cmq.1979.18.3.251. eprint: https://doi.org/10.1179/cmq.1979.18.3.251. URL: https://doi.org/10.1179/cmq.1979.18.3.251.

[23] L. W. Schmerr Jr. *Fundamentals of Ultrasonic Nondestructive Evaluation - A Modeling Approach*. Springer, 2016. DOI: 10.1007/978-3-319-30463-2.

[24] L. W. Schmerr Jr. and S.J. Song. *Ultrasonic Nondestructive Evaluation Systems - Models and Measurements*. Springer, 2007. ISBN: 978-0-387-49061-8. DOI: 10.1007/978-0-387-49063-2.

[25] C.E. Shannon. “Communication in the presence of noise”. In: *Proceedings of the IRE* 37(1) (1949), pp. 10–21.

[26] H. N. G. Wadley. “Sensors for intellingent processing of materials”. In: *J. Fluid Mech.* 19 (1971).

[27] J. J. Wen and M. A. Breazeale. “A diffraction beam field expressed as the superposition of Gaussian Beams”. In: *Journal of Acoustical Society of America* 83 (1988), pp. 1752–1756.

[28] J. J. Wen and M. A. Breazeale. “Computer Optimization of the Gaussian Beam Description of an Ultrasonic Field”. In: *Computational Acoustics: Scattering, Gaussian and Aeoracoustics* 2 (1990), pp. 181–196.

[29] Wikipedia. *Cross-correlation*. 2021. URL: https://en.wikipedia.org/wiki/Cross-correlation.

[30] Wikipedia. *Electromagnetic acoustic transducer*. URL: https://en.wikipedia.org/wiki/Electromagnetic_acoustic_transducer.

[31] Wikipedia. *Gaussian beam*. URL: https://en.wikipedia.org/wiki/Gaussian_beam.

[32] Wikipedia. *Ultrasonic testing*. 2021. URL: https://en.wikipedia.org/wiki/Ultrasonic_testing.